Printing technologies for current collectors for dye-sensitized solar cells.

Cherrington, Martyn A

Swansea University
Prifysgol Abertawe

Printing technologies for current collectors for dye-sensitized solar cells

Martyn A. Cherrington

Thesis submitted to the Swansea University in fulfilment
of the requirements for the Degree of Doctor of Engineering

2012

ProQuest LLC.
789 East Eisenhower Parkway
P.O. Box 1346
Ann Arbor, MI 48106 – 1346

Summary

This project was in collaboration with TATA Steel Colors to investigate printing technologies for current collection grids in dye-sensitized solar cells (DSCs) for high volume, large area production. Current collecting grids are important to reduce resistive losses and maintain performance.

The aims of the thesis were to; investigate different high volume printing technologies as an alternative to screen printing for depositing current collector grids, develop a fast drying and sintering method for improved manufacturing speed, and to develop monitoring technology for quality control to optimize production.

Flexographic printing was identified as an alternative to screen printing. Flexible DSCs produced with a flexographic printed current collecting grid were found to have an efficiency drop of ~33%, when compared cells built with screen printed current collecting grids. However, the amount of silver printed using flexography saw a reduction of ~95% offering a significant reduction in materials cost.

A barrier to high volume roll-to-roll printing of conducting inks is the time required for drying and for nanoparticle inks sintering. Nanoparticle inks require a secondary sintering phase to form a highly conductive metallic film. Near infrared (NIR) radiation has been shown to be a rapid method for drying and sintering a silver nanoparticle ink in just 1 second, compared to 10 minutes in an oven, offering a significant reduction in process time. Polymer thick-film inks with microparticles require thermal treatment to remove the solvent to facilitate particle contact which allows the ink to become conductive and NIR drying was found not to be effective.

Quality control of the sintering process of silver nanoparticle inks is carried out offline. A method which could be implemented inline has been developed using colorimetry to correlate the colour of a silver nanoparticle ink film to its electrical performance using CIELAB colour coordinates. It is a fast, non-contact method. The technique works on the principle of light scattering through nanoparticles.

Declaration and statements

DECLARATION

This work has not previously been accepted in substance for any degree and is not being concurrently submitted in candidature for any degree.

Signed ..... (candidate)

Date 31/7/2013

STATEMENT 1

This thesis is the result of my own investigations, except where otherwise stated. Where correction services have been used, the extent and nature of the correction is clearly marked in a footnote(s).

Other sources are acknowledged by footnotes giving explicit references. A bibliography is appended.

Signed ..... (candidate)

Date 31/7/2013

STATEMENT 2

I hereby give consent for my thesis, if accepted, to be available for photocopying and for inter-library loan, and for the title and summary to be made available to outside organisations.

Signed ..... (candidate)

Date 31/7/2013

Acknowledgements

I would like to offer my sincere thanks to all those who have supported me throughout this thesis, in particular; Prof. Tim Claypole, Prof. David Gethin, Prof. David Worsley and Dr. Maarten Wijdekop.

Thank you to my sponsors TATA Steel Colors and the EPSRC. Without their funding this project would not have happened and I would not have had the opportunity to work on what has turned into a very enjoyable project.

To everyone at the WCPC who has offered advice, support and friendship over the years I am very grateful. A special thank you to: Dr. Davide Deganello, Dr. Dave Beynon, Dr. Chris Philips and Mrs. Christine Hammett.

'I'd just like to say... thanks' to the guys at SPECIFIC who have been a great source of support and friendship throughout: Dr. Trystan Watson, Dr. Ian Mabbett, Dr. Eifion Jewell, Dr. Matt Carnie, Dan Bryant and Pete Greenwood.

I would also like to thank those from TATA Steel Colors who have supported me throughout this project. Special thanks to; Paul Jones, Dr. Jon Elvins and Rod Rice. Thank you also to Mikael Khan from Dyesol for keeping me supplied with ink.

The morning coffee club has become a something of an institution (probably resembling the WI) over the past few years. These coffee breaks have been a great source of venting frustration and celebrating success, although the latter normally involved beer instead of coffee. Cheers guys- John, Dai, Davide, Neil, Will and Chappers.

Thank you to my housemate, friend and fellow member of the thesis procrastination club, Neil Graddage – thanks for putting up with me for the last 3 years and helping me 'hone' the essential life skills of darts and snooker.

Thanks to my family for their constant support over my (seemingly endless) years at university.

Finally, thank you to my girlfriend Lucie. You have always been there for me and your support, patience and understanding have been ever present.

Table of contents

List of figures

List of tables

Nomenclature

Common abbreviations used in this thesis:

*a** - Green-red colour component of CIELAB colour space

*b** - Blue-yellow colour component of CIELAB colour space

CE – Counter electrode

CIELAB - CIE 1976 (*L**, *a**, *b**) color space, from the International Commission on Illumination (French: *Commission internationale de l'éclairage*)

DSC – Dye-sensitized solar cell

FF – Fill factor

FTO – Fluorine-doped tin oxide

ITO – Indium tin oxide

IR - Infrared

Isc – Short circuit current

Jsc – Short circuit current density

*L** - Lightness component of CIELAB colour space

NIR – Near infrared

PEN – Polyethylene naphthalate

PET – Polyethylene terephthalate

Pmax – Maximum power

PTF – Polymer thick film

PV – Photovoltaic

R2R – Roll-to-roll

SEM – Scanning electron microscopy

SPR – Surface plasmon resonance

TCO – Transparent conducting oxide

WE – Working electrode

Voc – Open circuit voltage

1 Introduction

In 1991 Gräzel and O'Regan published a paper, regarding photoelectrochemical solar cells, which offered a low cost approach to photovoltaics (PV) [1]. They utilized a colloidal dispersion of TiO_2 which, when applied to a conducting glass substrate and thermally treated, formed large surface area photoelectrodes. When used in conjunction with efficient sensitizers they resulted in a high efficiency photoelectrochemicial cell. The technology was named Dye-sensitized Solar Cells (DSCs). The development of screen printable polymer-organic TiO_2 pastes [2] and high efficiency cells produced on metal substrates [3] lead to the realization that it may be possible to produce DSCs in a roll-to-roll (R2R) process. R2R manufacturing offers continuous, high volume production potential which would reduce the cost of DSCs considerably, meaning that low efficiency modules could be produced in a large scale to contribute a significant proportion of electricity generation for a given country.

In 2006 TATA Steel (then Corus Colors) began a collaborative project with Australian company Dyesol Ltd to develop a cost effective, low efficiency, high volume, PV coating through DSCs which could be manufactured directly onto steel strip to create a building integrated photovoltaic (BIPV) system for roofing [4].

Scale-up of DSCs from the laboratory to a R2R produced BIPV array provides many challenges. One of these challenges is metallization, where current collecting grids are applied in between individual DSC cells in a module to minimize resistive losses of the generated current to maximize the efficiency of the device. Metallization can be achieved by printing conductive inks. A flow diagram of the process is shown in Figure 1-1. The main issue regarding R2R processing of conductive inks is that their post-printing drying and/or sintering processes are lengthy and provide a barrier for high speed production; printing is fast, drying is slow. This barrier to production is common to the general field of printed electronics. Once the ink has been printed and subsequently processed

there are no commercially available systems which offer quality control for monitoring the electrical performance of conductive inks upon their exit from the post-printing process. Research into printing technologies for depositing the conductive inks for DSC metallization is currently limited to screen printing, which is not a high speed, high volume production process, when compared to other available printing methods [5].

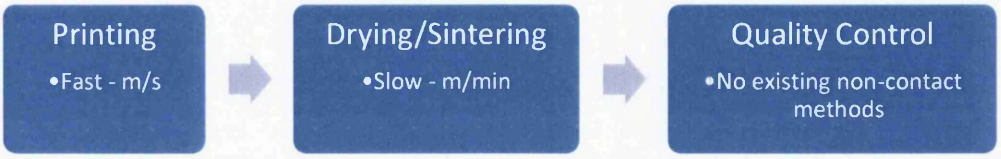

Figure 1-1 Flow diagram of printing for metallization application

This thesis aims to:

- Investigate printing technologies suitable for high volume R2R production of current collectors for flexible DSCs,
- Develop and optimize a method to increase the speed of the drying and/or sintering process for conductive inks,
- Conceptualize a quality control method which could be used in-line to monitor the sintering process of a metallic nanoparticle conducting ink.

1.1 Dye-sensitized solar cells

When compared to other PV technologies the advantages that DSCs offer are:

- Low cost,
- Ability to work well in diffuse and low level light conditions,
- Aesthetic properties, as they can be produced in a variety of colours and can be transparent,
- Potential for R2R processing.

There are scientists from many disciplines as well as engineers and industrialists whom are interested in the development of DSCs. The number of research publications has grown exponentially since 1991. Industrial interest has also grown with large multinational companies such as BASF and Bosch in Europe and Toyota, Sharp, Panasonic, Sony, Fujikura and Samsung in Asia [6]. In Wales TATA Steel and G24i have pilot production facilities with both companies capable of producing modules in a R2R manner.

1.1.1 Basic operating principles

The most commonly employed semiconductor in DSCs is a mesoporous layer of sintered TiO_2 nanoparticles [7]. Other oxides, such as ZnO and Nb_2O_5 have been investigated. Adsorbed onto the metal oxide film is a dye, which when photoexcited can inject an electron from its lowest unoccupied molecular orbital (LUMO) into the conduction band of the oxide. Injected electrons percolate through the network of sintered nanoparticles until they reach a conductive contact where they are exported to an external circuit to do work. The dye, minus its donated electron, is in an oxidized state and is subsequently reduced to its original state via electron donation from a redox electrolyte. The electrolyte is commonly a I^-/I_3^- redox couple dissolved in an organic solvent. It is crucial that the oxidized dye is reduced quickly to prevent it from recapturing an injected electron from the conduction band of the oxide. Having sacrificed their electrical potential to do work, the electrons flowing in the external circuit return to the counter electrode where they reduce the I_3^- of the redox couple in the electrolyte, which was oxidized during the reduction of the dye, completing the circuit [8]. Figure 1-2 shows an energy level diagram which describes the energetics of the basic processes. The important factor is that the LUMO of the dye must be higher than the oxide conduction band to achieve an efficient electron injection. The open circuit voltage (V_{OC}) of the cell is derived from the energy difference between the electron fermi level in the semiconductor and the redox potential of the electrolyte.

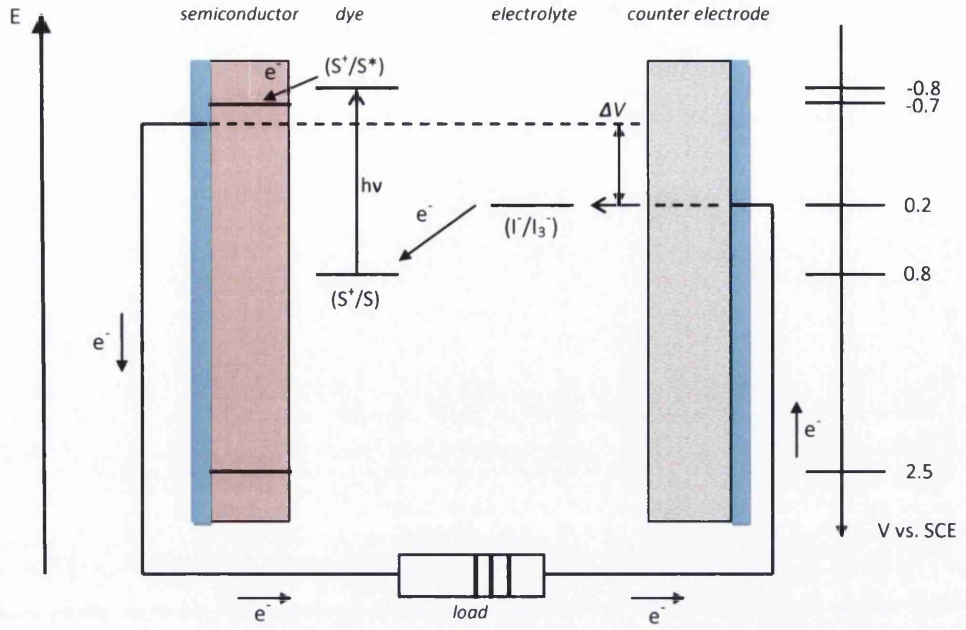

Figure 1-2 Energy level diagram outlining the basic operating principles of a DSC. Reproduced from [9].

The architecture of a typical DSC is illustrated in Figure 1-3. From the top side to the back contact a DSC usually consists of:

1. A transparent layer or topsheet (glass or polymer film), coated with a transparent conductive oxide (TCO), usually indium or fluorine doped tin oxide.
2. A wide band gap oxide semiconductor sintered onto 1.
3. A monolayer of sensitizing dye adsorbed onto 2.
4. A redox electrolyte.
5. A thin platinum catalytic layer deposited onto 6.
6. Substrate (typically glass), coated with TCO.

The working electrode consists of parts 1-3 and the counter electrode consists of parts 5-6 with the electrolyte in between. DSCs are often solely made using glass substrates and are often transparent. Flexible DSCs produced using metal substrates and polymer films have the working electrode sintered onto the metal

and the counter electrode forms the topsheet. Consequently the light has to travel through the electrolyte.

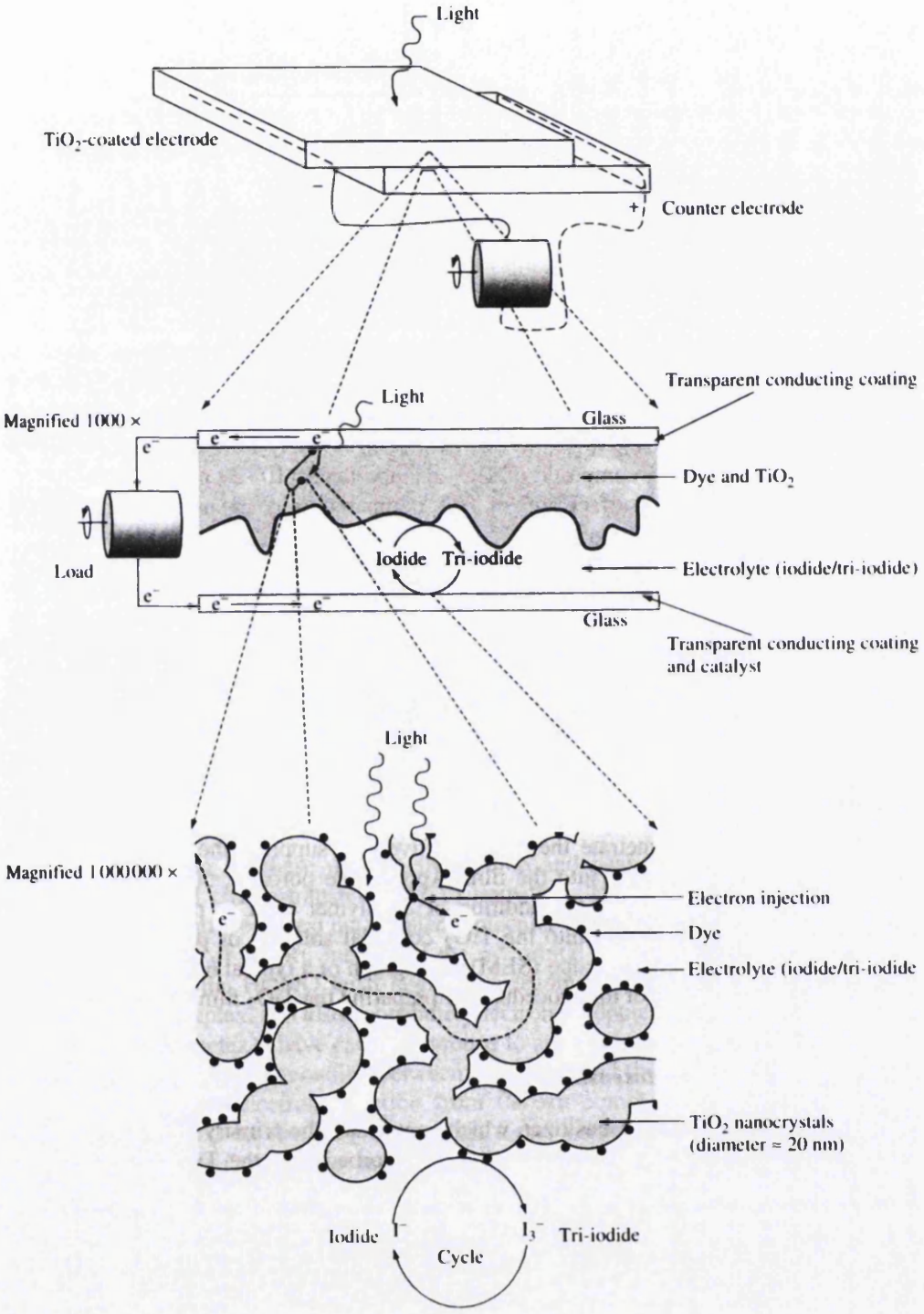

Figure 1-3 Schematic of a traditional DSC cell. Reproduced from [10].

1.1.2 Industrialization and scale-up of DSCs

In this section the terms 'cells', 'modules' and 'panels' are used as follows:

- *Cells* are units consisting of a single anode-cathode system which is hermetically sealed and has two terminal contacts.
- *Modules* are units of multiple cells, connected in series or parallel, with cell-to-cell seals and a perimeter seal and two terminal contacts.
- *Panels* are units comprising of multiple modules which are encapsulated and have two terminal contacts.

The scale-up of DSCs from the laboratory scale, where typical cell active areas are $\leq 1 cm^2$, to modules with larger active areas requires a metallization process to create current collection 'grids'. These grids reduce resistive losses and maximize the efficiency. Traditional methods for metallization involve additive processes such as electroplating, and are based on photolithographic techniques. Printing technologies are now being employed to print conductive inks (discussed later in this chapter) to increase the rate of production and reduce costs. Metallization for DSCs has focused solely on screen printing for depositing conductive inks because it is the printing technology of choice for applying the TiO_2 layer. Conductive inks can be printed rapidly but their subsequent drying requires a lengthy process.

Laboratory scale DSC test cells can take up to 24 hours to manufacture because of the various heat treatments and the dyeing step. Clearly this is not compatible when considering scale-up for R2R production of DSC modules. There are several 'rate limiting steps' in the DSC manufacturing process:

- Sintering of the TiO_2 nanoparticles.
- Dyeing of the sintered TiO_2 layer.
- Drying and/or sintering of conductive inks for metallization.

The sintering of the TiO_2 nanoparticles requires a thermal treatment which takes ~30 minutes, plus cooling time. This is too long to implement for volume R2R production as the oven length would be unfeasibly long. To reduce this process

time to make R2R production more feasible for flexible DSCs on metal, Watson *et al*, from Swansea University, used near infrared (NIR) radiation to sinter TiO_2 on titanium substrates, reducing the process time from 30 minutes to 12.5 seconds [11]. This resulted in cells which were comparable in performance to those prepared conventionally.

Dyeing of the sintered TiO_2 is usually carried out overnight, which is not compatible with a rapid production process. Holliman *et al* have demonstrated a method which reduces dyeing time to 5 minutes using a pumping procedure [12, 13]. A method for *in-situ* monitoring of the dye uptake process has demonstrated by Swansea and Bangor Universities [14].

The drying and/or sintering of metallic conductive inks along with current scale-up research for DSCs are discussed in the literature review in chapter 2.

1.1.3 Alternative photovoltaic technologies

There are many different types and generations of photovoltaic technologies which are not being considered in this body of work:

- *First generation* PV technologies are semi-conducting p-n junctions usually based on crystalline silicon [8].
- *Second generation* PV technologies are focused on reducing the cost of first generation PV cells by utilizing thin-film manufacturing technologies and examples include; Cadmium telluride (CdTe), copper indium gallium sellenide (CIGS), gallium arsenide, indium gallium nitride, amorphous silicon. Details can be found in [8].
- *Third generation* PVs are solar cells which are potentially able to overcome the Shockley-Queisser limit of 31-41% efficiency for single bandgap solar cells. The third generation PV technologies offer theoretical lower manufacturing costs and, as previously mentioned, include DSC but also other emerging technologies such as organic photovoltaics [15].

1.2 Printed electronics

The 1980s saw the birth of functional organic devices for the mass market. The advancement of the field through the 1990s included contributions from chemists, physicists and electrical engineers. In the early 2000s the print industry, a well established community, joined the organic electronics world. This strange collaboration between microelectronics and graphics printing has exhibited much promise to spawn a new method for producing electronics and introduce a whole new industry [16].

The advent of functional ink technology has allowed for printing technologies, such as ink jet, flexography, gravure and screen to be investigated for R2R manufacture. These technologies are better known for producing books, newspapers and packaging. The main advantage of using these printing technologies for producing functional electronic devices is cost. Traditional methods for producing electronics such as photo-lithography, chemical vapour deposition and electroplating are complex, multistep processes which are inherently costly. Table 1-1 shows a generalised comparison of the processes in conventional and printed electronics.

Table 1-1 Comparison of conventional and printed electronic processes.

	Conventional	**Printed electronics**
Process	Batch	Continuous
Production speed	Slow	Potentially fast
Capital cost	High	Low/moderate
Materials	Well defined and established	Under development
Cost	Moderate in high volume	Low/moderate
Substrate	Silicon wafers	Varied, flexible
Environmental	Acceptable	Friendly
Economic run length	Large	Small to very large

Printed electronics is an industry which is rapidly developing across the world. The areas of research are vast and include; displays and lighting, energy generation, energy storage, simple wireless products, electrical components and sensors (see Figure 1-4).

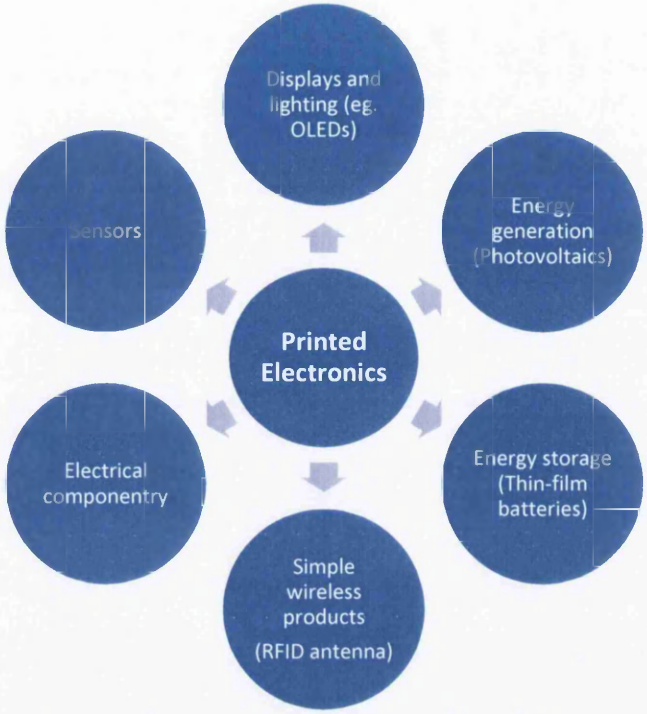

Figure 1-4 Schematic of printed electronics.

Within these areas specific research is well advanced in radio frequency identification tags, organic photovoltaics, dye-sensitised solar cells (DSCs), organic light emitting diodes, organic thin-film transistors, thin-film batteries, printed sensors.

1.3 Printing technologies

The printing technologies used for manufacturing printed electronic devices are discussed in this section. Table 1-2 offers a comparison of the process factors for the main printing technologies. The printing methods are well understood and there are many sources available for information [5, 17, 18].

Printing technologies which are referred to throughout this thesis include:

- Screen
- Gravure
- Flexography
- Ink jet

Table 1-2 Comparison of the process factors for each printing technology

	Screen Printing	**Rotogravure**	**Flexography**	**Ink Jet**
Resolution	Medium (~100 μm)	Very high (12 μm)	High (20 μm)	Very high - Medium (2.5 - 60 μm)
Average film thickness	Thick (1-20 μm)	Variable (<0.1 – 5 μm)	Variable (<0.1-5 μm)	Thin (<1 μm)
Capital cost	Low	High	Medium/low	Medium-High
Speed	Slow (<100 m/min)	Very high (1 km/min)	High (600 m/min)	Slow if single nozzle (mm/min)
Economic run length	Small-medium	Large	Medium-large	Medium
Ink viscosity	High (1-100 Pa.s)	Medium-low (0.05-0.5 Pa.s)	Medium-low (0.05-1.5 Pa.s)	Low (0.05 Pa.s)
R2R/Sheet-fed/Direct write	Sheet-fed/R2R if rotary or cylindrical	R2R	R2R/Sheet-fed	Direct write

1.3.1 Summary of printing technologies

Table 1-2 shows a comparison of the printing technologies considered in this thesis [5].

For depositing fine features, in the order of a few microns, then screen printing is not suitable and ink jet printing depends upon the quality of the printer nozzle but rotogravure and flexography would be suitable. If a thick ink film, greater than a few microns, is required then screen printing is the logical choice.

The operating costs associated with rotogravure; due to engraving costs, and ink jet; due to nozzle and cartridge costs, make them unfavourable for printed electronics. Costs associated with rotogravure can be offset if the print run is large enough. Ink jet costs depend upon how many nozzles are on the press but the main issue with printed electronics applications are that if particle inks are used then the particle size needs to be carefully monitored to prevent nozzle blocking which then impacts on maintenance costs. For screen printing the cost of screens are low and as a result the economic print run can be low. For flexography printing plates are slightly higher in price than screens so economic printing runs are longer than screen printing but shorter than rotogravure and inkjet.

The process speeds of rotogravure and flexography make them the technologies best suited to high volume manufacturing. Screen printing is relatively quick in a rotary press configuration but significantly slower in flatbed press configurations. Ink jet printing depends entirely on how many print nozzles are in the press and the number of nozzles then has a knock-on effect with cost; the more there are the greater the capital cost, but the faster the printing speed. A single nozzle ink jet unit is very slow because the nozzle has to move to print the image (which is a digital master) and means that the write speed is typically in the order of 0.2 mm/min. This makes ink jet an unsuitable technology for high volume production.

1.3.2 Screen printing

Screen printing is a flexible process with a wide range of operations. This is mainly due to the simplicity of the process and its ability to print both thick and thin films.

Applications in the screen printing industry are:

- Graphics, with packaging, advertising and product decoration.
- Fabrics, including curtains, fabric covers, T-shirts etc.
- Electronics, printing sensors, circuits and electroluminescent displays.

1.3.2.1 Screen printing process

The principle of screen printing is shown in Figure 1-5. The image is held in the screen and the ink is held on the surface of the screen.

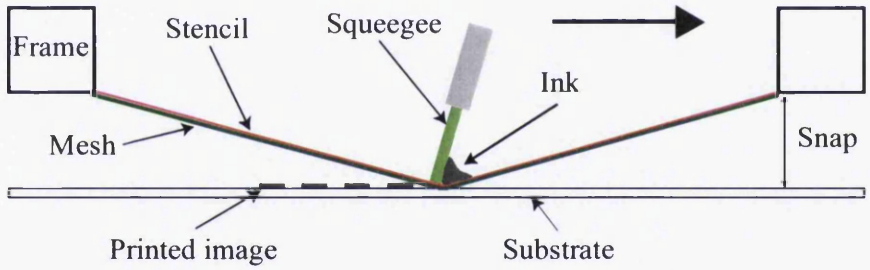

Figure 1-5 Schematic of the screen printing process

As the squeegee passes over the screen pushes the ink through the screen to the substrate. The process is discussed in detail in reference [5]. Screen printing essentially contains four distinct elements:

- Screen
- Squeegee and flowcoat
- Ink
- Press

1.3.2.1.1 Screen

The screen is the element that carries the image to be printed and can be split into three distinct parts:

- *Mesh*; made of woven fibres of either polyester or stainless steel.
- *Frame*; contains the mesh and stencil and commonly made from aluminium.
- *Stencil*; determines the ink film thickness and the quality of the print. There are two main types of stencil; direct emulsions and capillary films.

1.3.2.2 Squeegee and flowcoat

The squeegee is there to displace the screen to the substrate and to generate hydrodynamic pressure necessary to transfer the ink flow through the screen. The flowcoat redistributes the ink which has not passed through the screen after the print stroke.

1.3.2.3 Ink

Screen printing has a unique ability to be able to print a wide range of inks to any substrate. For the printed electronics industry this puts screen printing in a powerful position.

Metallic particle based, polymer thick film (PTF), inks whereby metallic flakes are dispersed in a polymer resin and a bulk solvent can be produced with a high concentration of particles to increase the conductance as the probability of metal particles contacting are greatly increased. Increasing the solid content inevitably increases the viscosity and as the particle size can range from 1-100μm the range of mesh specifications enables even the largest particles to be printed.

1.3.2.4 Press configuration

There are three generic types of screen press:

- *Flatbed*; characterised by a having a flat screen and a flat substrate bed.
- *Rotary*; used for continuous R2R production. The screen is cylindrical and consists of two concentric rings with an electronically deposited nickel alloy mesh wrapped around.
- *Cylinder*; used in continuous production. The screen is flat but the substrate bed is cylindrical and the frame reciprocates about a stationary squeegee.

Rotary presses have been used with much success in the wallpaper and textile industry and the unique R2R ability has lead to research for printed electronics, in particular for DSCs.

1.3.3 Rotogravure printing

The gravure process is one of the oldest volume printing processes. The origins of it date back to China in 100AD where wood carved plates were used. Modern gravure is derived from the "intaglio" printing process. In general, for any intaglio process, the image to be printed is recessed below the non-printing surface on a plate. Intaglio comes from the Italian word "in-taglio" which means "cut in". Rotogravure printing was first developed in the 1780's by Thomas Bell in Lancashire for printing onto cloth. The patents were based on an iron cylinder covered in engraved copper to carry the image with a doctor blade to remove the ink and an impression cylinder to force the substrate into contact with the cylinder. The principle has changed little over the years but the process has become more refined, in particular the engraving process. Despite its origins in the textile industry rotogravure printing is better known for its application in the printing of high quality graphics and high volume packaging.

1.3.3.1 Rotogravure printing process

The basic working principle of the rotogravure printing process is simple, see Figure 1-6.

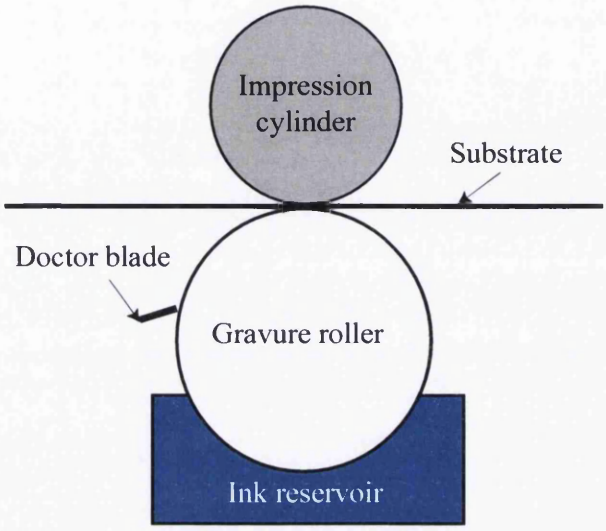

Figure 1-6 Schematic of the rotogravure printing process

The image to be printed is engraved on a cylinder as thousands of recesses, or cells. The engraved cylinder rotates in an ink bath where each cell is flooded with ink. A doctor blade is positioned to wipe-off and remove excess ink from the cylinder surface leaving the ink only inside the engraved cells. An impression cylinder is used to force the substrate into contact with the gravure cylinder. The area of contact is called the nip. At the nip the ink is drawn out of the cells and transferred to the substrate. The size of the cells determines the volume of ink which is available for transfer; larger cells transfer a greater volume of ink.

1.3.4 Flexography

Flexography evolved from letterpress printing, which uses a hard printing plate to transfer ink to a substrate. Its original name 'aniline' was used because the inks originally used aniline dyes, used until 1952, at this point flexography became the adopted name. In over 100 years of evolution from letterpress many

major developments, such as the introduction of anilox rollers, photopolymer plates and ink development, have occurred to give flexography the process as recognised today.

1.3.4.1 Flexographic printing process

A flexographic printing press comprises three basic parts, shown in Figure 1-7:

- Inking system,
- Plate cylinder,
- Impression cylinder.

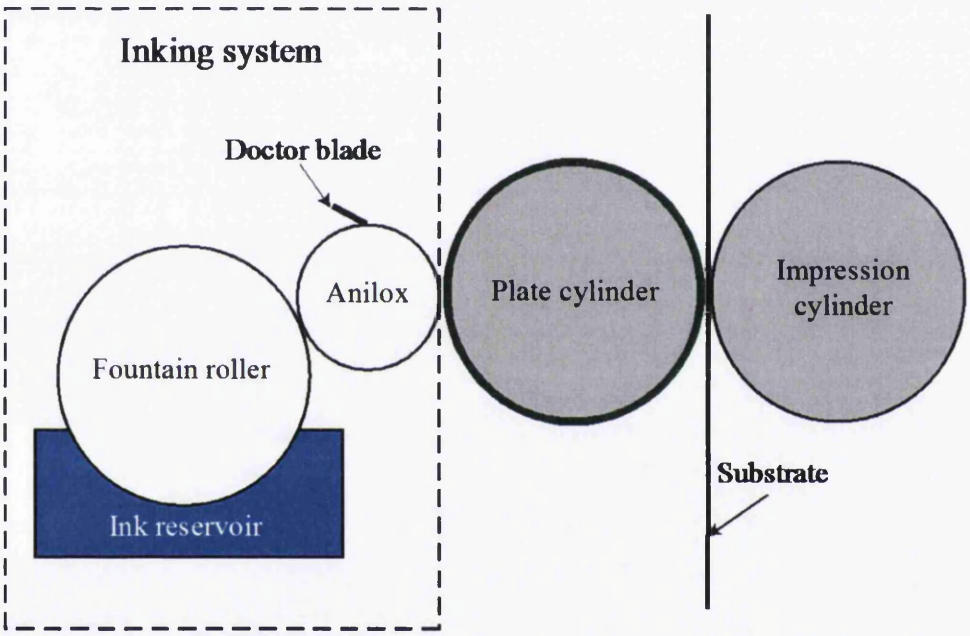

Figure 1-7 Schematic of the flexographic printing process

The *inking system* is used to transfer ink from a reservoir into the press. The quantity of ink transferred is governed by the amount of ink required to produce prints of an acceptable standard. The metering of the ink in the inking system is controlled by the anilox roll and a fountain roller and/or a doctor blade. Modern presses use a chambered system which contain two doctor blades and eliminates the need for a fountain roller. The anilox roll is designed to meter and control the volume of ink transferred to the printing plate. This is achieved by engraving

cells on the surface of the anilox. The cell geometry and the cell distribution determine the volume of ink to be transferred to the plate. To change the ink volume transferred a different anilox with a different cell volume is used.

The *plate cylinder* is used to mount the printing plate, on which the required image for printing is carried. The plate cylinder collects ink from the inking system and transfers it to the substrate. Plates are made from either rubber or a photopolymer, although the majority of modern plates use photopolymers. To mount the plate on the printing cylinder double-sided sticky tape, with a compressible inner layer, referred to as mounting tape, is used. It is available in a range of thicknesses and elasticity.

The *impression cylinder* is used to apply pressure facilitating contact between the plate cylinder/printing plate and substrate allowing printing to occur.

1.3.5 Alternative deposition methods for conductive features

There are alternative methods to printing for depositing conductive features. Common deposition technologies include:

- Chemical vapour deposition
- Physical vapour deposition

1.3.5.1 Chemical vapour deposition

Chemical vapour deposition (CVD) is a chemical process used to create high purity and high performance thin-films. Typically the substrate is exposed to one or more volatile precursor materials which react and/or decompose on the surface of the substrate producing the desired material coating. It is common for volatile by-products to also be produced and these are removed by gas flow through the reaction chamber. CVD can be carried out at atmospheric pressure, depending on the precursors being non-volatile, it is more common for the reaction chamber to be under vacuum in a controlled atmosphere [19].

CVD is a commonly used process in the semi-conductor industry when producing integrated circuits, or chips, with the process used to deposit a variety of materials including; silicon, silicon oxide, silicon nitride.

1.3.5.2 Physical vapour deposition

Physical vapour deposition (PVD) is a group of vacuum deposition processes used to deposit thin-film coatings by the condensation of a vaporised form of the desired film material, the target, onto a substrate. The method differs from CVD in that there are no chemical reactions occurring at the surface of the substrate and the material being deposited is *physically* coated on the substrate. Typical deposition rates are 1-10 nm per second [20].

There are several types of PVD which have different methods of vaporising the target material for example; using a high power electric arc to create a highly ionised vapour, bombarding the target with electrons transporting the material by diffusion, resistively heat the target material to evaporate it, use a high power laser to ablate the target material into a vapour, using sputter deposition where a glow plasma discharge localised around the target bombards the target causing the material to vaporise.

PVD is commonly used to deposit ITO onto plastic and glass substrates for use in electronic devices.

1.3.5.3 Summary of alternative deposition methods

CVD and PVD are both capable of depositing metal films for conductive tracks but in this thesis neither method is being considered for use as a coating process. The reasons for this are three-fold: Firstly, because both methods require carefully controlled atmospheric conditions. Secondly, both methods have slow deposition rates of <20 nm per second which would make multiple sample preparation very time consuming. Thirdly, both methods are expensive.

1.4 Inks

For a comprehensive guide on printing inks see references [5, 21]. Printing inks are generally made up of four main components:

- Colorant (Pigment/dye),
- Vehicle (binder),
- Additives,
- Carrier substance (solvents),

The *colorant* is either a pigment or a dye. Pigments are organic or inorganically coloured, white or black, substances which are insoluble in the binder. They are solid particles and/or molecular agglomerates that are held in suspension in the base liquid. Pigments work by dispersing light, although it is only molecules on or close to the particle surface which can absorb incident light and as a result pigments have a wide absorption band. Dyes are organic compounds that are dissolved in the system during application and are present in molecular form. The dye molecules are surrounded by solvents in the base liquid and almost every molecule can absorb photons. They also have a narrow absorption band and are much purer than pigments allowing for a much wider range of colours. Dyes also appear transparent as they are smaller than the waveband of visible light. Pigments always require a vehicle to bind them to the substrate while dyes connect directly to the substrate surface. Dyes are also susceptible to bleaching under prolonged light exposure which pigments are not. Pigments are cheaper materials to buy than dyes but are more expensive to process into ink as they require dispersants to prevent agglomeration whereas dyes dissolve into the base liquid.

The *vehicle*, or binder, are polymeric resins dissolved in a mineral oil. Common binders include; nitrocellulose, ethyl cellulose, polyvinyl alcohol (PVA), polyimide, polyamide. Pigments are dispersed in the binder and enclosed by a binder shell. The shell prevents the particles agglomerating. The binder dries onto the surface of the substrate and binds the pigment.

Additives are used to modify the behavior of an ink. Additives are commonly used to influence drying, flow behavior and rub resistance.

The *carrier substances*, hold the colorants. The carrier substance acts as both a thinning agent, for example mineral oil in the binder, and solvent.

This section will introduce the concepts behind conductive inks and how they work.

1.4.1 Conductive inks

Conductive inks require low resistance pathways through which electrons can move when a potential is applied across the material [16]. In a bulk metal the metallic bonding between atoms makes conductivity efficient in all directions. To make an ink conductive a conductive polymer backbone or conductive particles in direct contact, in a non-conductive matrix, are required. For low resistance and high conductivity, metallic particles are most commonly used.

There are three main types of conducting inks which will be introduced:

- Microparticle (polymer thick film),
- Metal nanoparticle,
- Organic (Metal organic deposition),

The choice of metal to use for a solution-processed conducting ink relate to the bulk resistivity, price and handling. An ideal metal-based ink would be cheap, easy to prepare, store and print, and give excellent conductivity after post-printing processing. Table 1-3 shows the performance and costs of metals used for conductive inks. In terms of electrical resistivity silver has the lowest, followed by copper and then gold. In terms of cost the most expensive is gold, followed by silver with copper significantly cheaper [22]. A significant factor in choosing a metal is whether it can be easily processed into an ink. For instance, copper is extremely cheap but oxidizes easily, especially with nano-size particles which oxidize spontaneously in air [23]. Gold is prohibitively expensive but is

easy to process into an ink. Silver is the current metal of choice and is the most reported in the literature. Other metals which have been processed into inks are aluminium and nickel [24] which are relatively inexpensive but offer poorer electrical performance.

Table 1-3 Electrical performance and costs of metals for conductive inks [22]

Metal	Volume Resistivity (Ω.m)	Cost (USD per Troy Ounce)
Silver	1.59×10^{-8}	35
Copper	1.72×10^{-8}	0.30
Gold	2.44×10^{-8}	1500
Aluminium	2.82×10^{-8}	0.08
Nickel	6.99×10^{-8}	0.75

1.4.1.1 Polymer thick film

Polymer thick film (PTF), or microparticle, inks are primarily composed of metallic flakes, usually silver, but copper and gold have both been used. Non-metallic carbon flakes have been used but due to their high resistance are only good where low conductivity is not an issue. The flakes, which are micron sized, are suspended in a retaining polymer vehicle which may/may not be conductive.

Once printed the retaining polymer matrix must be reduced to facilitate conductance by allowing the metal, or carbon, particles to come into contact. This reduction in the polymer matrix is known as curing. Curing is achieved via a number of methods (e.g. thermal, UV) but the most common is thermal curing in an oven. The bulk solvent is evaporated and the binder will polymerize attaching the particles to the substrate.

The conductivity of PTF inks depend upon the density of the particles in the cured ink film; the higher the particle density the better the conductivity. However, the greater the particle density is the greater the viscosity of the ink

and because the viscosity can be varied PTF inks can be printed with a wide range of printing technologies including screen, gravure and flexography although inkjet printing is not feasible due to particles blocking the nozzle.

1.4.1.2 Metal nanoparticle

A different approach to producing a conductive ink is to use metallic nanoparticles (diameter range 5-100nm depending on ink) suspended in a solvent at 30-50wt%. Most commonly used metals are silver and gold although copper based inks are now becoming commercially available. The nanoparticles are coated in a stabilizing shell to prevent agglomeration.

After printing the solvent is evaporated and the shell around the nanoparticles is removed enabling contact between the particles. This facilitates some conductance although contact resistance between the particles inhibits the conductivity of the ink film.

When reducing particle size to the nanometer scale the surface area to volume ratio of a particle increases dramatically, when compared to the bulk material, and this reduces the melting temperature. This enables the ink film to undergo a sintering step which melts the particles 'fusing' them together. The advantage of this is that the particle density is greatly increased and contact resistance between particles is eliminated allowing a highly conductive ink film which can be very thin (sub micron).

Silver nanoparticles are the most commonly used as silver it has the lowest resistivity of all metals (15.87nΩ.m) and has a good balance between cost and performance. Gold nanoparticles are more desirable as they have better chemical stability and higher work function. Copper nanoparticles are particularly attractive compared to gold and silver as materials cost is significantly cheaper.

Nanoparticle inks can be printed by any printing technology although the formulation will differ depending on the ink viscosity required for the printing method.

1.4.1.2.1 Sintering

Sintering is the process when thermal energy is applied to a powder compact, the compact is densified and the average grain, or particle, size increases [25]. The sintering process was associated with ceramics (for instance the firing of pottery) but now sintering is also associated with power metallurgy and consequently with metallic conductive inks.

When the particle size of a metal is reduced its melting temperature is depressed [26-28]. Silver has been shown to have a melting point reduced from 960°C to approx. 150°C when the particle size has been reduced to approx. 20 nm diameter [28].

The mechanisms of sintering are discussed in more detail in Chapter 2.

1.4.1.3 Summary

Although other nanoparticle inks, such as gold, copper and aluminum are available only silver nanoparticle inks will be considered in this thesis because silver is the best performing electrically and because at the time of this work there were no decent commercially available nanoparticle inks that were not silver or gold, which is prohibitively expensive.

1.4.1.4 Metal organic deposition

Metal organic deposition (MOD) inks are organometallic inks. The dry organometallic compounds, for example silver (hexafluoroacetylacetonate), 1,5-cyclooctadiene, are dissolved in a solvent. These are printed and the precursor

material is thermally decomposed on the substrate to form a metallic film. The gaseous byproducts from the decomposition are removed leaving behind a contaminant free metal film. These inks usually contain the lowest metallic content and are normally outperformed electrically. The most common printing technology used to deposit MOD inks is inkjet as nozzle clogging by particles is avoided.

1.5 Drying methods of inks

Drying includes all processes which take place after the ink transfer, i.e. post-printing. During the drying process the ink solidifies as the solvent is removed to leave behind the colorant and vehicle. The ink composition affects whether the drying is effected by a chemical reaction or a physical process, see Figure 1-8.

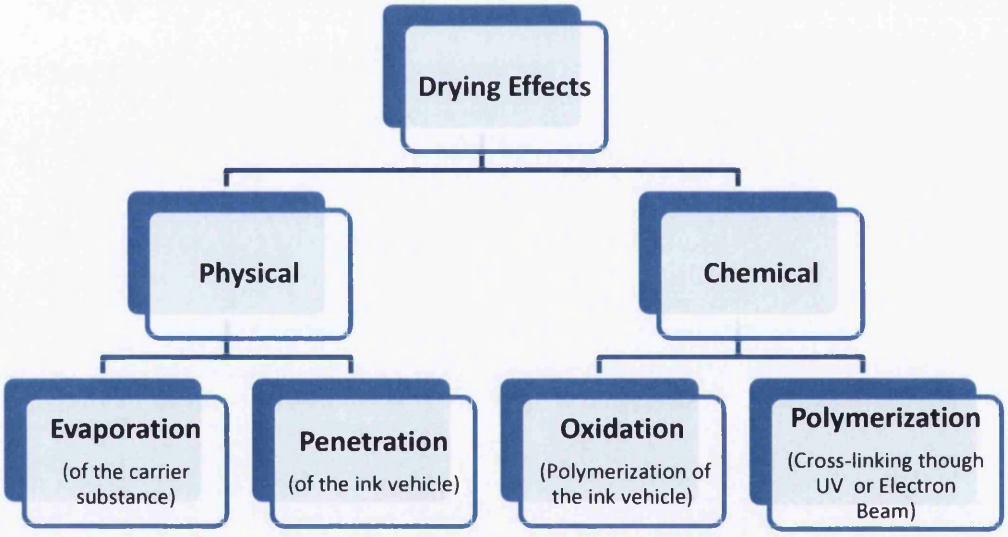

Figure 1-8 An overview of the effects in the drying process. Reproduced from reference [5]

1.5.1 Physical drying

Physical drying is used when the ink contains solid pigments and resins in a liquid medium and the liquid binding agents are removed. The mechanism of drying is achieved either through *evaporation*, where the carrier substance is

removed thermally or *penetration*, where the ink vehicle absorbs radiative energy. The main methods for physical drying are hot-air drying and infrared (IR) drying.

1.5.1.1 Hot-air drying

The carrier solvent in the ink system is evaporated thermally, with energy absorbed into the ink film via convection, and the solid contents of the ink are then fixed as the resin cures to the substrate. Hot-air drying is affected by the thermal properties of the carrier solvent; high boiling point solvents require more time for evaporation. Another factor to consider is the ink viscosity; a viscous ink tends to have a greater solid content so there is less solvent to remove. Temperature needs to be considered as it has to compliment the substrate as well as the ink system; too high and substrate damage can occur and/or the solvent could 'flash' off damaging the ink film.

1.5.1.2 IR drying

The IR region of the electromagnetic spectrum is between 800 – 1 x 10^6 nm. IR radiation causes vibrations of the bonds of functional groups in organic molecules and these vibrations induce thermal heat. IR drying primarily works because the ink vehicle, which consists of organic materials, absorbs the irradiated energy and heat up the ink system causing evaporation of the solvent(s). Conventional IR dryers use IR sources within the mid-IR waveband (2-4μm).

1.5.2 Chemical drying

Chemical drying is normally associated with inks which contain fluid binders which are solidified in a chemical reaction. This is achieved either through *oxidation* of the ink vehicle or *polymerization* through cross-linking. The

methods for chemical drying are either UV radiation or electron beam (EB) radiation.

1.5.2.1 UV drying/curing

The UV region of the electromagnetic spectrum is between 10-380nm. Common UV driers use a waveband of 100-380nm. UV drying of printing inks is based on radical polymerized ink vehicles which contain photo-initiators. No evaporation and therefore no mass loss occur from the ink system.

1.5.2.2 Electron beam drying/curing

EB is an ionizing radiation of very high energy which ionizes the molecules in the ink vehicle causing the release of free-radicals which initiate polymerization. The wavelength of EB radiation is at 1nm in the X-ray part of the electromagnetic spectrum.

1.6 Closure, objectives and thesis layout

Printing technologies for the scale-up of DSCs have focused primarily on screen printing. This is because it is the only method capable of achieving a film thickness satisfactory for the TiO_2 working electrode (8-12μm). A consequence of this is that screen printing has also been exclusively used for their metallization; to deposit the current collectors, with a focus on using PTF inks. PTF inks contain large metal solid content and a printed thick film, combined with the high cost of silver, adds to the manufacturing costs for DSCs.

A major inhibitor to the industrialization of DSCs is the post-printing drying and/or sintering step: The greater the time required for the post-printing processes, the longer and more capital intensive the ovens need to be for a R2R production line. This is not just an issue specific to DSCs but with all printed

electronic devices. There are also no existing quality control methods for monitoring these post-printing processes in-line.

This thesis aims to investigate methods to aid the industrialization of DSCs and the printed electronics industry by offering potential solutions to the aforementioned issues:

- Alternative printing methods for the metallization of DSCs will be investigated with the aim of reducing the amount of silver used by depositing thinner films without compromising cell performance by utilizing nanoparticle silver ink.
- Investigating methods to decrease the drying and/or sintering times of PTF and nanoparticle silver inks to improve the process feasibility for high speed, high volume R2R manufacturing.
- Develop a potential method for in-line quality control monitoring of the drying/sintering performance for nanoparticle conductive inks as a tool for R2R production.

The structure of the thesis is as follows:

- Chapter 1 – Introduction and background of DSCs, printed electronics, printing technologies and conductive inks,
- Chapter 2 – Literature review,
- Chapter 3 – Experimental apparatus and materials,
- Chapter 4 – A comparison of printing technologies for the deposition of conductive tracks,
- Chapter 5 – An investigation into using flexography for the metallization of DSCs,
- Chapter 6 – Near infrared processing of conductive inks,
- Chapter 7 – Near infrared drying and sintering characteristics of flexographic printed features using a nanoparticle silver ink,
- Chapter 8 – Evaluation of electrical performance through colour: A potential non-contact, in-line measurement system,
- Chapter 9 – Conclusions and further work.

1.7 References

1. O'Regan, B. and M. Gratzel, *A LOW-COST, HIGH-EFFICIENCY SOLAR-CELL BASED ON DYE-SENSITIZED COLLOIDAL TIO2 FILMS.* Nature, 1991. **353**(6346): p. 737-740.
2. Ma, T.L., T. Kida, M. Akiyama, K. Inoue, S.J. Tsunematsu, K. Yao, H. Noma, and E. Abe, *Preparation and properties of nanostructured TiO2 electrode by a polymer organic-medium screen-printing technique.* Electrochemistry Communications, 2003. **5**(4): p. 369-372.
3. Ito, S., N.-L.C. Ha, G. Rothenberger, P. Liska, P. Comte, S.M. Zakeeruddin, P. Pechy, M.K. Nazeeruddin, and M. Graetzel, *High-efficiency (7.2%) flexible dye-sensitized solar cells with Ti-metal substrate for nanocrystalline-TiO2 photoanode.* Chemical Communications, 2006(38): p. 4004-4006.
4. http://www.dyesol.com/index.php?element=Corus 31/08/2012
5. Kipphan, H., *Handbook of print media : technologies and production methods.* 2001, Springer: Berlin ;.
6. Hagfeldt, A., G. Boschloo, L. Sun, L. Kloo, and H. Pettersson, *Dye-Sensitized Solar Cells.* Chemical Reviews. **110**(11): p. 6595-6663.
7. Gratzel, M., *Dye-sensitized solar cells.* Journal of Photochemistry and Photobiology C-Photochemistry Reviews, 2003. **4**(2): p. 145-153.
8. Luque, A. and S. Hegedus, *Handbook of Photovoltaic Science and Engineering.* 2003: John Wiley & Sons.
9. Hagfeldt, A. and M. Gratzel, *LIGHT-INDUCED REDOX REACTIONS IN NANOCRYSTALLINE SYSTEMS.* Chemical Reviews, 1995. **95**(1): p. 49-68.
10. Smestad, G.P., *Education and solar conversion: Demonstrating electron transfer.* Solar Energy Materials and Solar Cells, 1998. **55**(1-2): p. 157-178.
11. Watson, T., I. Mabbett, H. Wang, L. Peter, and D. Worsley, *Ultrafast near infrared sintering of TiO2 layers on metal substrates for dye-sensitized solar cells.* Progress in Photovoltaics. **19**(4): p. 482-486.
12. Holliman, P.J., M.L. Davies, A. Connell, B.V. Velasco, and T.M. Watson, *Ultra-fast dye sensitisation and co-sensitisation for dye sensitized solar cells.* Chemical Communications. **46**(38): p. 7256-7258.
13. Holliman, P.J., M. Mohsen, A. Connell, M.L. Davies, K. Al-Salihi, M.B. Pitak, G.J. Tizzard, S.J. Coles, R.W. Harrington, W. Clegg, C. Serpa, O.H. Fontes, C. Charbonneau, and M.J. Carnie, *Ultra-fast co-sensitization and tri-sensitization of dye-sensitized solar cells with N719, SQ1 and triarylamine dyes.* Journal of Materials Chemistry, 2012. **22**(26): p. 13318-13327.
14. Watson, T., P. Holliman, and D. Worsley, *Rapid, continuous in situ monitoring of dye sensitisation in dye-sensitized solar cells.* Journal of Materials Chemistry, 2011. **21**(12): p. 4321-4325.
15. Brabec, C., U. Scherf, and V. Dyakonov, *Organic Photovoltaics: Materials, Device Physics, and Manufacturing Technologies*: Wiley.
16. Gamota, D., *Printed Organic and Molecular Electronics.* 2004: Kluwer Academic.
17. Crouch, J.P., *Flexography Primer.* 1998: GATFPress.

18. Kasunich, C.L., *Gravure Primer*. 1998: Graphic Arts Technical Fndtn.
19. Jones, A.C. and M.L. Hitchman, *Chemical Vapour Deposition: Precursors, Processes and Applications*. 2009: Royal Society of Chemistry.
20. Mattox, D.M., *Handbook of Physical Vapor Deposition (PVD) Processing*. 1998: Elsevier Science.
21. Leach, R.H., *The Printing Ink Manual*. 1993: Springer.
22. http://www.metalprices.com/ 13th June 2012
23. Grouchko, M., A. Kamyshny, and S. Magdassi, *Formation of air-stable copper-silver core-shell nanoparticles for inkjet printing.* Journal of Materials Chemistry, 2009. **19**(19): p. 3057-3062.
24. Tekin, E., P.J. Smith, and U.S. Schubert, *Inkjet printing as a deposition and patterning tool for polymers and inorganic particles.* Soft Matter, 2008. **4**(4): p. 703-713.
25. Kang, S.J.L., *Sintering: Densification, Grain Growth and Microstructure*. 2004: Elsevier Science.
26. Buffat, P. and J.P. Borel, *Size effect on the melting temperature of gold particles.* Physical Review A, 1976. **13**(6): p. 2287-2298.
27. Wronski, C.R.M., *The size dependence of the melting point of small particles of tin.* British Journal of Applied Physics, 1967. **18**(12): p. 1731.
28. Moon, K.-S., H. Dong, R. Maric, S. Pothukuchi, A. Hunt, Y. Li, and C.P. Wong, *Thermal behavior of silver nanoparticles for low-temperature interconnect applications.* Journal of Electronic Materials, 2005. **34**(2): p. 168-175.

2 Literature review

2.1 Introduction

This review is split into two sections: The first section will review flexible dye-sensitized solar cells, with a focus on the substrates used and metallization methods for depositing current collecting grids. The second section will focus on conductive nanoparticle inks and will review; the mechanism of nanoparticle sintering, optical properties of nanoparticles and post-printing methods for sintering.

2.2 Flexible dye-sensitized solar cells

The principles behind DSCs were introduced in chapter 1. To enable the DSC to be produced R2R the substrate materials for the electrodes have to change from the traditional rigid glass to flexible materials such as polymer films and metal sheet, with the latter critically important for the TATA Steel/Dyesol project. This section reviews metal and plastic substrates for flexible DSCs and their subsequent devices.

2.2.1 The standard preparation method of rigid glass DSCs

Figure 2-1 shows a typical laboratory sized DSC test cell. The typical laboratory methods for depositing the working electrode (WE) TiO_2 layer are doctor-blading, spraying and screen printing. For small cells ($\leq 1 cm^2$) the most common method is doctor-blading; where a mask, cut from regular office tape, is attached to the transparent conductive oxide (TCO) coated glass substrate. A thin layer of TiO_2 paste is spread using a glass rod or microscope slide. TiO_2 pastes can be either prepared or obtained commercially. In addition to the TiO_2 nanoparticles the paste contains a

high viscosity organic solvent, for example terpineol, organic binders and porosity/morphology controlling agents such as cellulose derivatives.

The deposited TiO_2 paste is post-treated to achieve mechanical integrity and good electrical conduction between the particles and the substrate TCO. This is obtained through thermal sintering at 450-500°C for ~30 minutes.

After cooling the sintered TiO_2 layer is placed in a dye solution (typical concentration of the dye ~0.3mM in ethanol) for sensitization. The dyeing process usually takes place overnight to ensure a proper monolayer adsorption of the dye to the TiO_2. For R2R manufacturing the dyeing time is a barrier to production and methods to reduce the process time were discussed in chapter 1.

Platinized counter electrodes (CE) are usually prepared using a thermal method [1] or sputtering. For the thermal method the CE is coated with a platinum salt (e.g. $PtCl_4$ or H_2PtCl_6) in isopropanol and heated to 385° C for 10-15 minutes. The platinum salt is reduced to platinum and forms Pt nanoparticles on the TCO glass surface.

To seal the electrodes together the most common method is to use a thermoplastic ionomer resin film such as Surlyn® or Bynel® which are melted between the electrodes on a hotplate (~100°C) whilst applying slight pressure at the same time. The film also acts as a spacer leaving a thin space for the electrolyte and preventing a short circuit from occurring. The electrolyte is then inserted through a hole drilled through one of the electrodes or through a channel in the spacer film.

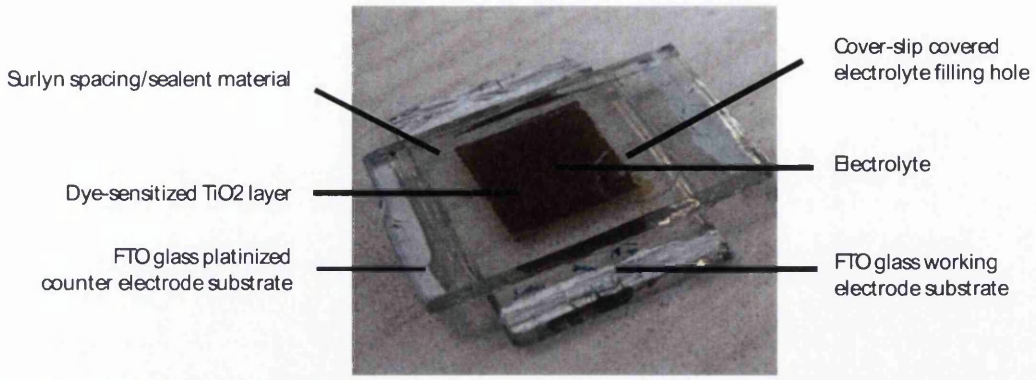

Figure 2-1 A typical 1cm^2 laboratory scale rigid dye-sensitized solar cell

2.2.2 Plastic substrates for DSCs

Plastic substrates for use as electrodes in DSCs require a conductive TCO coating. The TCO coating predominantly used is an indium doped tin oxide (ITO) layer.

Investigations by Zardetto *et al* into plastic substrates for use in flexible electronic devices have determined that the best substrates are ITO coated polyethylene terephthalate (PET) or polyethylene naphthalate (PEN) which has been heat stabilized [2]. PEN films are more thermally stable than PET but they are more expensive. Zardetto *et al* showed that PET/ITO exhibits good electrical stability up to 150°C but at higher temperatures the sheet resistance increases dramatically until it melts at 250°C. PEN/ITO sheet resistance stayed stable up to 235°C and only showed a significant increase at 250°C where partial melting had occurred.

The ITO coating (15Ω/□) reduces the transmission in the visible region by ~5% for both PEN and PET although the latter is more transparent that the former (with and without an ITO coating).

Both PET/ITO and PEN/ITO films offer good thermal stability, electrical stability and optical properties for use in DSCs but no high temperature preparation methods (>150°C for PET and >180°C for PEN) can be used during DSC preparation. For

plastic CEs thermal platinization has to be replaced and for plastic WEs a low temperature sintering process is required. Other potential issues with using plastic substrates over glass include; poorer barrier properties, as plastic is not as efficient as glass at preventing oxygen and water permeation, and mechanical sturdiness.

A plastic WE requires a low temperature method to sinter the TiO_2 layer. There are currently only two suitable methods which are compatible with plastic foils and R2R processing; binder-free pastes [3-5] and compression methods [6-9]. Removing the binder from TiO_2 paste allows the high temperature sintering step to be avoided and sintering can be achieved at temperatures <150°C and cell efficiencies of 5.8% have been achieved on PEN/ITO [5]. Compression methods involve static or continuous pressing of TiO_2 nanoparticle suspensions onto plastic substrates. The pressing forms firm contacts between adjacent nanoparticles. Cells of with an efficiency of ~5% have been produced in this manner.

Using plastic as a substrate for the CE requires a low temperature platinization method to deposit the catalyst. Sputtering [10, 11], chemical reduction [12-14] and electrochemical deposition [10, 15-17] are the two most common low temperature techniques. Chemical and electrochemical methods reduce platinum from a platinum salt solution and are R2R compatible. Chemical reduction requires an additional reducing agent, such as sodium borohydride, whereas the electrochemical method requires an electric field. Both chemical and electrochemical methods have been used to produce cells, which have metal WEs, with high efficiencies of 8.6% [14] and 7.2% [15] respectively. Sputtering, whilst being a low temperature method and suited for use with plastics, requires the sample to be under vacuum and is not suitable for R2R.

2.2.3 Metal substrates for DSCs

Metal substrates for DSCs can offer several advantages over their glass counterparts: Firstly, metal substrates are cheaper than TCO coated glass. Secondly, the sheet resistance of metal is significantly lower than that achieved through TCO coated substrates. Thirdly, metals offer high temperature processing, which is important for sintering of the TiO_2 layer.

Using metal substrates as CEs have been investigated using a glass WE [18]. However, for a flexible DSC the WE is a polymer film, so TiO_2 preparation has to be a low temperature process. The most popular method is to pressure sinter the TiO_2 nanoparticles [19, 20] but this is too slow for R2R use and because of this metals are only going to be considered for the WE substrate in this thesis. The main disadvantage of using a metal as the WE is that the incident light must pass through the CE and the electrolyte before interacting with the dye shading the photoactive area, although the losses in efficiency are smaller than equivalent losses caused by the low temperature sintering methods if the metal is used as the CE.

There have been many studies carried out using metals as either the CE or WE with stainless steel (SS), galvanized carbon steel, Inconel, titanium, copper all investigated [21-24]. However, after stability testing in electrolyte solutions it has been found that only SS and titanium metals are suitable [25] and aside from their corrosion resistance both SS and titanium exhibit large recombination resistance (movement of electrons from the substrate to the electrolyte). A summary of DSCs made with metal WEs is presented in Table 2-1.

Table 2-1 Summary of DSC with metal working electrodes

WE Substrate	CE Substrate	Cell area (cm^2)	Jsc (mA/cm^2)	FF (%)	Efficiency (%)	Ref.
SS	ITO/PET	0.32	2.40	51	0.9	[22]
SS	ITO/PET	0.25	7.70	45	2.59	[23]
SS	FTO Glass	1.00	2.40	68	1.2	[26]
Ti	ITO/PEN	n/a*	13.6	68	7.2	[15]
Ti	FTO Glass	0.50	6.94	61	3.2	[24]
Ti	ITO/PET	0.25	6.71	54	2.4	[23]
Ti	FTO Glass	1.00	6.00	70	3.1	[26]

*Believed to be a very small active area

The negative side to using metals as a WE substrate is that for scale-up to a module a series connection between cells is near impossible and cells are connected in parallel. This limits their output voltage to that of a single cell (V_{oc} = 0.6 to 0.8V) [25]. TCO coatings on glass substrates can be etched to insulate adjacent cells making series connection possible. The major advantage of metals is that current collection is easy due to the near bulk sheet resistivity, which is an issue with TCO coatings.

The width of a single conventional DSC on glass is restricted to ~1cm due to the large sheet resistance of the TCO (~15Ω/□) [27]. Using a metal substrate the sheet resistance is low (for Ti ~0.003Ω/□) and cell width could be up to 20cm, although the TCO on the CE poses a barrier to this.

2.2.4 Metallization deposition methods

To reduce manufacturing costs of silicon solar cells alternative ways to photolithographic methods for metallization have reported over the years. Metal grid deposition by screen printing silver conductive inks was first done 30 years ago [28, 29] and improvement in mesh design has lead to a significant reduction in track

widths [30]. Nickel/copper electroplating has been researched [31] and more recently flexography has been trialed as a method to deposit a seed layer for electroplating [32].

For DSCs little has been reported in the literature regarding metallization methods. Screen printing has been used to deposit conductive silver ink by Lee *et al* [33] to improve performance of strip cells on FTO glass with active areas of 1.4cm^2. They achieved a significant improvement in performance improving FF and efficiency by 70% and 89% respectively. Another method which has been reported by Okada *et al* is nickel electroplating [34]. Nickel was found to have good corrosion resistance to the electrolyte and by building a large cell on top the nickel grid they achieved 5.1% efficiency for a cell with an active area of 68.9cm^2.

2.2.5 Closure

The purpose of this section was to review what work had been reported in the literature for flexible DSCs. Methods for building DSCs using both plastic and metal substrates for both electrodes have been reviewed, their relative cell performances compared and methods reported for metalizing have been discussed.

Flexible DSCs have been produced with promising performances. PET and PEN films have been shown as suitable materials, although plastic substrates can only easily be used to make CEs due to temperature constraints. Titanium and stainless steel have been shown to be the metal substrates of choice and their ability to withstand high temperature processing and their very high conductivities give a great advantage over plastic and glass substrates. Cells built using titanium and PEN have been reported with excellent performances. The result of this review is that all cells made in this body of work will use metal substrates for the working electrodes to alleviate the lower sintering temperature required if a plastic substrate were used instead. Titanium will be used as the performance of the reported cells are greater.

Reported work on metallization methods for DSCs is limited to screen printing silver conductive inks and electroplating methods. No other printing technologies have been investigated to the authors' knowledge. This gap in the literature offers an opportunity to investigate alternative printing methods for the metallization of DSCs. As the Tata Steel DSC project is focusing on developing R2R production methods the printing technology to be investigated is flexography. All of the data published in the literature is for cells with very small active areas ($\leq 1.0 cm^2$). To test the performance of a cell using different printing methods for metallization a more realistic, larger active area will be used.

2.3 Conductive nanoparticle ink processing

2.3.1 Introduction

As the field of printed electronics grows and devices begin to be produced *en mass* in a R2R process, the rate limiting step for volume production is the drying and sintering process. For example, if a sintering step requires ten minutes on a line running at 100 m min^{-1} then a conventional oven would be 1 km in length, which is not feasible, both from a plant footprint and capital cost perspective [35].

Nanoparticle conductive inks require an additional post-printing step to enhance their conductivity. The solvent is removed during the drying phase, followed by a curing phase where the organic stabilizing shell around the particle is removed allowing direct contact between the particles and facilitating conductance. Although described as separate phases the drying and curing occur simultaneously. After drying and curing, a sintering phase then occurs to form a continuous metallic film which effectively eliminates inter-particle contact resistance. Nanoparticles have much reduced melting temperatures due to their large surface area to volume ratio. Typical sintering temperatures are between 120°C - 140°C for between 5 – 10 minutes.

This section will review the sintering mechanism, optical characteristics and post-printing techniques for the drying and sintering process of silver nanoparticle conductive inks. Process time and suitability for R2R manufacturing will be considered.

2.3.1.1 Mechanism of nanoparticle ink sintering

Nanoparticle conductive inks have been introduced in Chapter 1. Although solvent evaporation during the drying process forces the nanoparticles together, conductivity only arises when metallic contact between particles is achieved and a continuous

network is formed throughout the printed film. An organic layer between the metal particles as thin as a few nanometers is enough to prevent electrons from moving between particles [36]. Curing removes the organic shell around the nanoparticles and the curing temperature is defined as the temperature at which this organic removal starts and particles start showing conductance through direct physical contact. After curing the ink film is conducting but the contact resistance between the particles is significant. To remove the effect of contact resistance the nanoparticles may form larger particles through *Ostwald ripening* or sintering; where the surface energy is reduced because of the large surface area-to-volume ratio of the particles' [37].

Sintering occurs at a higher temperature than curing, when all the organic material has been removed, and necks start to form between particles. There are two important properties which require consideration in the field of sintering: firstly, the lowest temperature at which features begin to conduct, usually determined by the organic additives in the ink [38] and secondly, finding the lowest possible resistance of the ink film at the lowest possible temperature. A low resistance is achieved through sintering the particles to transform initially very small contact areas to thicker necks and eventually a dense layer. Very low resistances can be obtained through the formation of large necks, which decrease constriction resistance and eventually form a metallic crystal structure with few grain boundaries.

At low temperatures the driving forces for sintering are mainly due to Ostwald ripening [39]. Ostwald ripening is a method of particle growth where large particles grow at the expense of smaller ones. This occurs because small particles have a small radius of curvature: smaller spheres are bent more sharply and therefore have a higher curvature, which is equal to the reciprocal radius of a sphere ($1/R$). As a result, smaller particles have a higher chemical potential than larger particles [40] which means that larger particles are energetically more favorable.

Ostwald ripening facilitates surface and grain boundary diffusion rather than bulk diffusion within the coalesced particles. Densification can only occur when atoms are removed from the contact surface, or a grain boundary, so that the centers of the spheres can move towards each other, as depicted in Figure 2-2. In these processes, the centers of the spherical particles approach each other, as the neck between them widens, increasing the particle contact area. Neck formation is also driven by the reduction in surface energy by atomic diffusion where the material fluxes from areas of positive curvature to areas of negative curvature. The energy reduction from neck formation is offset by the energy of grain boundary creation [41]. The Ostwald ripening process stops when a particle diameter approximately one and a half times its original size is formed. This leaves a porous structure and as a result a resistivity value greater than the bulk material is achieved. The relative density increases with increased temperature which reduces the porosity. Larger particles are formed due to particle migration and coalescence.

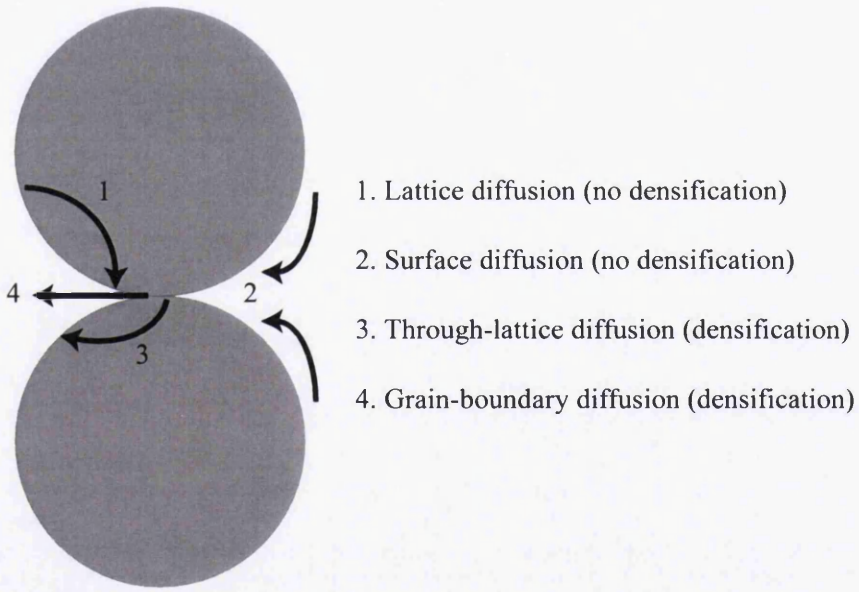

Figure 2-2 A schematic representing various atomic diffusion paths between two contacting particles. Paths 1 and 2 do not produce any shrinkage while paths 3 ad 4 enable the sphere centers to approach one another, resulting in densification. Image reproduced from reference [41].

2.3.2 Optical characteristics of nanoparticles

Silver metal has a characteristic white colour. This is caused by the presence of filled d bands near the electron energy surface of the s-p conduction band (NB. Electronic configuration of silver is [Kr] $4d^{10}5s^{1}$). The excitation energy for silver corresponds to absorption in the ultraviolet region (~300nm – 400nm) so when incident radiation hits the metal surface the reflected radiation contains the entire visible spectrum (350nm – 750nm) appearing white [42].

When a solid particle of any shape is illuminated with incident electromagnetic radiation, part of the energy associated to the incident wave is absorbed and the rest is scattered. The sum of the parts is known as the extinction. When the radiation interacts with the particle, its electrons start to oscillate, absorbing energy, which is transformed into, for instance, thermal energy (Cf. Photonic sintering). The scattered radiation is a consequence of the radiation emitted by the accelerated electrons. When the frequency of the incident radiation matches the natural frequency of the surface electrons oscillating against the restoring force of the nuclei this excitation of the surface electrons is known as surface plasmon resonance (SPR). The first person to address the optical response of particles was Gustav Mie who studied a homogenous dielectric sphere of arbitrary size. Mie solved Maxwell's equations for the sphere in 1908, calculating the electric and magnetic fields inside and outside a spherical object enabling the calculation of light scattering and absorption.

Silver nanoparticles of an approximate diameter of 30nm are known to exhibit absorption at about 430nm, which corresponds to the violet part of the visible spectrum [43-45] (see Figure 2-3). This absorption is caused by a localised SPR. With the violet part of the spectrum absorbed the scattered light makes the silver nanoparticle solution appear yellow/green in colour. As the particle size increases silver nanoparticles exhibit a red-shift in the absorbance where SPR occurs, see Figure 2-4.

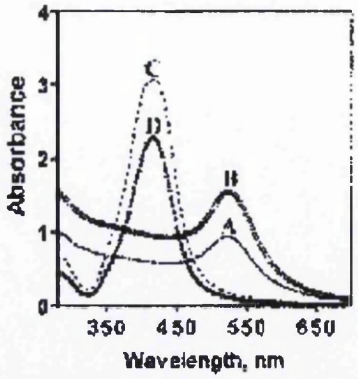

Figure 2-3 Absorbance spectra of solutions of gold (A and B) and silver (C and D) nanoparticles, measured using water (A and C) and hexane (B and D) as solvents. Diameter of the silver nanoparticles are ~30nm. Taken from reference [44].

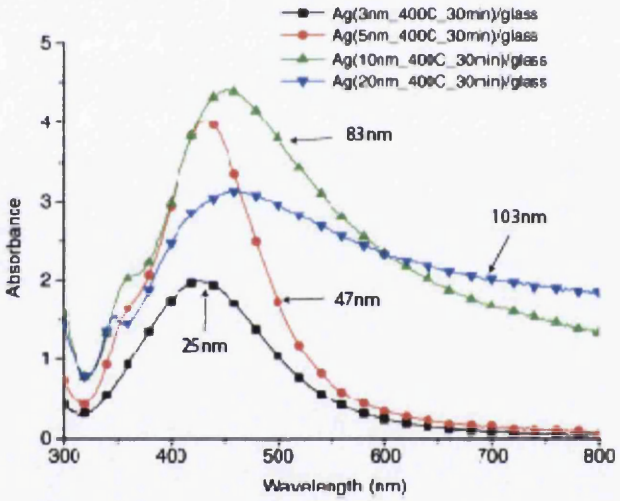

Figure 2-4 Optical absorption spectra of silver island films on glass annealed with various thicknesses. The average particle diameters for each dataset are highlighted. Taken and modified from reference [45].

2.3.3 Post-printing processes for metallic nanoparticle conductive inks

2.3.3.1 Conventional sintering methods

There are two conventional ways to sinter a nanoparticle ink; thermally and at room temperature. This section will discuss the two methods in turn.

2.3.3.1.1 Thermal sintering

Thermal heating is the conventional method for sintering nanoparticle inks. In general, oven temperatures of at least 150°C with dwell times of up to 4 hours are needed to achieve a sintered ink film.

Szczech *et al* [46] reported inkjet printing a silver nanoparticle (diameter 1-10nm) suspension in toluene onto polyimide and glass substrates and sintering at 300°C for 15 minutes achieving a resistivity of 22 x bulk silver. There are several disadvantages for printing flexible electronics: firstly, toluene is an aggressive solvent and not suitable for use with the majority of polymer substrates. Secondly, the high sintering temperature of 300°C makes the use of inexpensive polymer substrates infeasible.

Park and Baek [47] observed that when they aerosol jetted printed features ~30μm wide onto silicon using a silver nanoparticle ink (diameter ~40nm) and sintering at 200-400°C for 1-4 hours the microstructure of the silver became denser with increasing temperature. However, the centre of the line decreased in thickness as the silver became denser resulting in an increased resistance.

Lee *et al* [48] used a silver nanoparticle colloid (diameter 10-50nm) dispersed in a water/diethylene glycol mix. They inkjet printed the ink onto glass and pre-dried at 70°C for 5 minutes to remove the solvent before sintering at 150 - 260°C. They

observed that particle sintering only started occurring at 150°C and the particle boundaries were still visible. Above 200°C the boundaries between particles disappeared. Best electrical performance occurred at 260°C but after a dwell time in the oven of 60 minutes, however, after 3 minutes a resistivity of 10 x bulk silver was achieved which is a significant improvement on what Szczech *et al* achieved.

More recently Dennulin *et al* [49] have reported that after 60 minutes at 400°C on glass, sintered silver nanoparticle ink (diameter 20nm) showed a 2500% growth in particle size. They also reported that after 5 minutes at 200°C a resistivity of ~130 x bulk was achieved although the best resistivity of 50 x bulk was achieved at the same temperature after 60mins.

The Schubert group [50] attempted to reduce the sintering temperature by formulating a silver nanoparticle ink with a low amount of organic additives. They managed to make the ink conduct at 80°C, a significant improvement.

There are several nanoparticle inks commercially available [51-53] that can be sintered at <140°C although recommended processing times vary from 5 to 30mins.

Sintering nanoparticle inks in an oven, whilst feasible on a laboratory scale, is not a realistic option when rapid roll-to-roll production is desired. Long process times mean that the length of the oven will be unfeasibly long. The high temperatures make the use of cheap polymer substrates, such as PET, impossible as the temperatures are close to or above the materials glass transition temperature which would lead to the substrate being damaged.

2.3.3.1.2 Room temperature sintering

Another option is not to use any post-printing processes for sintering nanoparticle inks but to allow them to sinter at room temperature (RT).

In the literature there are many examples of RT sintered nanoparticle inks [54-57]. There are several accepted mechanisms for RT sintering occurring: The first method allows the solvent to evaporate slowly, which causes the stabilizer to collapse onto the particle surfaces causing the nanoparticles to coalesce, or sinter [55, 57]. The second method is to chemically neutralize the stabilizer which causes particles to sinter. The Magdassi group first reported using HCl vapour to enhance nanoparticle sintering in 2009 and managed to achieve a resistivity of 7 x bulk silver [56]. They enhanced the process and found that increasing the acid concentration increased grain size and that just a 10s exposure was enough for sintering to occur, achieving a remarkable 2.4 x bulk resistivity [54].

2.3.3.1.3 Summary of conventional sintering methods

There are several obvious disadvantage for using conventional thermal and room temperature methods for sintering nanoparticle inks: Firstly, the slow speed of the processes inhibits R2R processing. Secondly, the high temperatures required to reach a resistivity value close to the bulk material prevents the use of cheaper polymer substrates. Thirdly, using an acid vapour in a production line presents several health and safety issues. As an example; if a R2R manufacturing speed is 100 m/min, and the sintering time in an oven is 5 minutes, the oven would need to be 500m long.

2.3.3.2 Alternative sintering methods

Alternative approaches for sintering nanoparticle conductive inks are discussed in this section with a focus on the technologies suitability for high volume R2R production. The sintering methods discussed are; laser, microwave, plasma, infrared, electrical, intense pulsed light.

2.3.3.2.1 Laser sintering

A laser is '*a light source which produces a beam of highly coherent and nearly monochromatic light as a result of cooperative emission from many atoms*' [58]. Laser is an acronym for "light amplification by stimulated emission of radiation".

An optical cavity with a pair of mirrors at each end contains the gain medium. The gain medium is stimulated, usually by an electric current, and the light produced by the simulated emission from the gain medium is amplified by bouncing back and forth between the mirrors in the optical cavity. The beam of light produced is a narrow beam which can be highly focused onto a narrow spot and because of this has a high irradiance.

There are two main types of laser operation; continuous wave and pulsed. A continuous wave laser has a power output which is constant over time. A pulsed laser produces a pulsed output at a fixed repetition rate.

Laser's can be tuned to a particular frequency depending on the gain medium. This has led to their use in selectively sintering nanoparticles. As the output is monochromatic the ink should absorb the energy but the substrate should be near-invisible preventing damage. The beam has to be focused on the printed line and only sinters the area of ink under the beam. This is dependent on the optics but is typically a narrow diameter.

The Poulikakos group first reported using an argon ion laser (100mW) tuned to 514nm to sinter thin-film, inkjet printed lines of gold nanoparticles (diameter 2-5nm) on a glass substrate, achieving 3 x bulk resistivity [59]. The wavelength of the laser was selected to prevent heating of the glass substrate. The average height of the lines was roughly 200nm and the ink was printed at 0.12m/min but was sintered at a speed which corresponds to 0.012m/min. By increasing the power of the argon ion laser (200-400mW) the group managed to improve the sintering speed to that of the

printer, at 0.12m/min, but the resistivity of the sintered gold nanoparticles was greater at 6 x bulk [60]. The group also reported that as the laser beam translates across the line Marangoni flow occurs where a surface tension gradient displaces ink around the laser spot changing the profile of the printed line [61]. At higher laser powers the glass substrate also experienced expansion causing damage. A polyimide based flexible substrate was demonstrated by Ko *et al* as suitable for laser sintering of gold nanoparticles for use as electrodes [62]. Another common problem associated with the argon ion laser sintering is that non-sintered particles, a result of the small radius of the beam, are washed away with solvent. This creates an issue with materials wastage.

Other types of laser using solid state gain mediums have been reported in the literature for sintering nanoparticles. Niizeki *et al* used a continuous wave Nb:YAG (neodymium-doped yttrium aluminum garnet) laser tuned to 1064nm to sinter silver nanoparticles (diameter ~5nm), spin-coated onto a copper substrate. The laser speed was equivalent to 0.03m/min [63]. Lesyuk *et al* managed to increase the speed of sintering silver nanoparticles onto Alumina to 0.3m/min achieving a resistivity of ~2.5 x bulk and by pulsing the laser sintered the silver nanoparticles on polyimide at 0.6m/min achieving 5 x bulk, however, a pre-drying step at 60°C for 10 minutes was used [64].

A Diode Pumped Solid State (DPSS) laser, with an output of 1064nm, was used by Chiolerio *et al* to sinter silver nanoparticles [65]. The gain medium was a neodymium-doped yttrium orthovanadate ($Nd:YVO_4$) crystal. A resistivity of 3 x bulk was achieved for thick and thin films at speeds of 0.09m/min and 0.03m/min respectively.

Other wavelengths have been used to sinter silver nanoparticles. Auyeung *et al* used a continuous wave 532nm green laser to sinter silver nanoparticles on polyimide at 0.006m/min, which is slow but resistivity's of 5 x bulk were reported [66].

Laser sintering is a good method for selectively sintering nanoparticles but there are several major disadvantages for implementing it in R2R manufacturing of printed electronics: Firstly, the beam has to follow the printed image and areas which do not get exposed to the beam do not get sintered and are wasted. Secondly, speed is extremely slow. Even the fasted speed of 0.6m/min is not feasible for high volume production. Thirdly, low cost and low glass transition temperature polymers, such as PET or PEN, are not suited as the power of the beam would cause damage. The only polymer substrates used at present are polyimide based. Fourthly, the cost and complexity of using a laser makes the technology impractical.

2.3.3.2.2 Microwave sintering

Microwave radiation is associated to the region of the electromagnetic spectrum between the infrared and radio with wavelengths in the range of 1 x 10^{-3}m - 1m, correlating to frequencies of 300GHz to 300MHz.

Microwave heating is used for sintering dielectric materials [67] and in synthetic chemistry [68]. It offers uniform, fast and volumetric heating. Microwaves are absorbed due to coupling with charge carriers or rotating dipoles.

Highly conductive materials, i.e. Metals, can be sintered by microwaves but they have a small penetration depth (the distance into the material at which the incident power is reduced to 1/e of the surface value). At 2.54GHz the penetration depth for silver, gold and copper is between 1.3 and 1.6μm [69]. This means that the microwave sintering of metals can only be successful if the dimension of the object at right angles to the plane of incidence is of the same order of magnitude as the penetration depth.

It is believed that the conductive particle interaction with microwave radiation, or inductive coupling, is mainly based on Maxwell-Wagner polarization, which results from the buildup of charge at the materials interfaces, electric conduction and eddy

currents [70]. The reasons for the successful heating of metal particles through microwave heating are still not fully understood.

For thermoplastic polymer substrates, below their glass-transition temperature, the bonding between molecules restricts the rotational movements of any dipoles present. Therefore the absorption of microwave radiation is minimal.

The Schubert group were the first to report using microwaves for sintering printed nanoparticle tracks [71]. Perelaer *et al* used inkjet printing to deposit nanoparticle silver inks onto a pre-heated (150°C) polyimide substrate. The sample was then placed into a microwave reactor and treated in continuous wave mode (300W). Temperature in the chamber reached 200°C and the ink reached a minimum resistivity of 19 x bulk after 240s, which is comparable to a sample oven sintered at 220°C for 60mins. Although reducing the sintering time is beneficial for volume production 240s, or 4 minutes, is still too long and the total process time does not include the heating of the substrate to 'enhance' solvent evaporation.

With this in mind Perelaer *et al* looked at ways to further reduce the sintering times [72]. They used antennae structures; inkjet printed using silver nanoparticles, onto polyethylene napthalate foil, and cured at 110°C for 60 minutes. The purpose of the antennae structure was to act as microwave absorbers and electrodes for measuring the resistance of a line of silver nanoparticle ink printed using inkjet over the ends of the antennae. The printed line was cured for 1-5 minutes at 110°C before being exposed to the microwave radiation for at 1-60s at a power of 1W. They found that just 1s exposure to microwaves at 2.45GHz is enough to promote sintering but the smaller the initial resistance is the better the effect and conductivity values are large at 10 to 34% bulk.

Microwave sintering can be used for sintering silver nanoparticle inks but only if the ink is already dry and with some inherent conductance. Using microwave radiation alone is still slow with a process time of at least 4 minutes. If an antennae structure to

absorb microwave radiation is present then sintering can be achieved in 1 second, however, a minimum of 1 minute is required to cure the ink and give it a degree of conductance. Microwave sources require heavy shielding and are not readily available for installing on a production line. This all makes R2R processing with microwaves infeasible.

2.3.3.2.3 Argon plasma sintering

Plasma is defined as: a state of matter, similar to a gas in which a certain portion of the particles are ionized. Heating a gas may ionize its molecules or atoms turning it into plasma, which contains charged particles.

For the high temperature sintering of particles plasma has been shown to be useful. However, where polymer foils are concerned high temperature leads to damage.

Reinhold *et al* showed that low pressure argon plasma could be used to sinter an inkjet printed silver nanoparticle ink [73]. Glass, polycarbonate and PET substrates were pre-heated to 120°C to allow solvent evaporation, but not particle sintering, to occur immediately after printing. The sample was then placed in a plasma chamber and argon plasma formed at a pressure of 1mbar. After 60 minutes the control oven sample at 220°C and plasma sample yielded resistivity's of 2.5 to 3 x bulk silver.

The theory behind the sintering of a nanoparticle silver ink is that the energetic ions and UV radiation from the plasma will decrease the chain length of the organic binding material around the nanoparticles. Low pressure will drive the evaporation of these fragments and allow the now-uncoated particles to coalesce and sinter.

The ink sinters from the top surface through to the substrate and shows an evolution from a sintered top layer to a bulk material. However, a negative point which results, from this top down sintering, is that even after a 4 hour exposure the bottom of the ink film can be un-sintered as Niittynen *et al* reported [74].

It is a good low temperature method and is suitable for most polymer foil substrates but plasma sintering is limited by the penetration depth of the plasma species. Processing time is too long for high volume production. That the process requires a specialized atmosphere, with an inert gas and under vacuum, makes it even more undesirable. It is not a suitable process for R2R manufacturing.

2.3.3.2.4 Infrared processing

The infrared (IR) region of the electromagnetic spectrum is situated in between the visible and microwave regions at a waveband of 750nm – 1mm.

IR radiation is associated with the heating of organic molecules, which absorb strongly in the IR due to dipole-dipole interactions between atomic bonds which cause vibrations between atoms.

Metals are strong reflectors of IR and silver in particular is one of the greatest reflectors, hence its traditional use in mirrors.

Denneulin *et al* used a long wave IR emitter (Waveband 8-15μm) to sinter an inkjet printed nanoparticle silver ink (diameter ~20nm) on glass and paper [49]. The theory being that the organics in the ink vehicle and the paper would absorb the IR to quickly increase the sample temperature and facilitate particle sintering. The IR lamp emitted between ~2200 W/m^2 and ~2950 W/m^2, depending on the source-sample distance. Substrate temperature was found to directly impact on the sheet resistance. The paper substrate heated much faster than the glass, despite paper having a low thermal conductivity, and as a result the process time on paper was less than on glass, 2 minutes and 3 minutes respectively. Comparative samples sintered in an oven at 200°C achieved a best sheet resistance after 5 minutes.

Further work on IR sintering of silver nanoparticle (diameter 20-50nm) inks on paper has been carried out by Tobjörk *et al* [75]. They used two IR sources: a short-wave IR (3 x 2kW) with an intensity of 2-4 W/cm^2 and a mid-IR (500W) with an intensity of approximately 0.6W/cm^2 and a maximum intensity at 4μm. Using the short-wave IR unit they achieved a resistivity of 5 x bulk silver in 20 seconds, for a film 300-500nm thick. With the mid-IR unit the resistivity achieved was 3.7 x bulk in 10 seconds. It was observed that the testing could not be achieved on low-cost plastic substrates, such as PET, as they were quickly thermally deformed. Tobjörk also observes that using radiative methods to sinter metal nanoparticles has the advantage over other processes because of the negative feedback of the process. As sintering occurs the light absorptance decreases, preventing overheating of the nanoparticle structures.

IR sintering of metal nanoparticles exhibits good potential for R2R manufacturing of printed electronics. All the work in the literature is carried out on paper and glass or expensive polymers. No work using cheap polymer substrates, such as PET, exists. If the process times could be reduced further to below 10 seconds then the risk of damage to the substrate could potentially be prevented.

2.3.3.2.5 Electrical sintering

Electrical sintering, or joule heating, is the process of applying an electrical potential between two electrodes to force a direct current through nanoparticles causing resistive heating to occur which facilitates particle sintering.

Allen *et al* reported that silver nanoparticle ink (diameter 10-20nm) was inkjet printed onto a temperature sensitive photopaper and after 3ms reached a resistivity of 1.7 x bulk silver, with the sintering occurring in just 2μs [76]. They claim several advantages for electrical sintering over other methods including; reduced substrate temperature as heating only occurs in the nanoparticle layer, short sintering time, obtaining a pre-determined conductivity value. The process can be split into three

parts: a pre-sintering phase, where the stabilizer is removed, a transition phase, where sintering occurs and the large-current phase. During the large-current phase the temperature increases to further reduce the resistivity, reaching a saturation point after 60 seconds.

Hummelgard *et al* studied the electrical sintering *in-situ*, using TEM probing, and found that there are two processes occurring simultaneously; nanoparticle sintering and a carbonisation process which alters the structure of the organic stabilizing shell surrounding the silver particles [77]. This carbonisation process leaves behind a carbon residue in the ink film. Conduction increases as soon as carbonisation starts which would indicate the stabiliser removal facilitating particle contact. Upon continued joule heating the carbon is seen to evaporate at high temperature. Sintering was found to occur when power levels were at 0.1-10mW/μm^3.

Electrical sintering is rapid and conductive features close to bulk can be achieved. A disadvantage of electrical sintering is that a continuous physical contact is required between the electricity source and the printed metallic structures, which is not easy to achieve in a R2R setup.

2.3.3.2.6 Photonic sintering

Photonic sintering, or intense pulsed light (IPL), is a low thermal exposure method developed to sinter nanoparticle thin films. A xenon flash lamp is used to deliver a high intensity, short duration, pulse of light to the printed film. The technology was first made public by Schroder *et al* [78].

A xenon flash lamp produces light by passing an electric current through xenon plasma at high pressure producing a brilliant white light. The lamp electrodes are connected to a bank of capacitors, which are charged to a high voltage. Pulsed light is discharged when a plasma arc is formed between the electrodes, when the xenon gas is ionized by a voltage bias of ~16kV. Once triggered, using a pulse controller,

approximately 1kA of current is delivered from the capacitors within milliseconds. The spectrum produced is across a wide waveband from 160nm to 2.5μm [79]. A typical spectrum is shown in Figure 2-5. General practice for using polymer substrates is to use a UV filter to prevent damage.

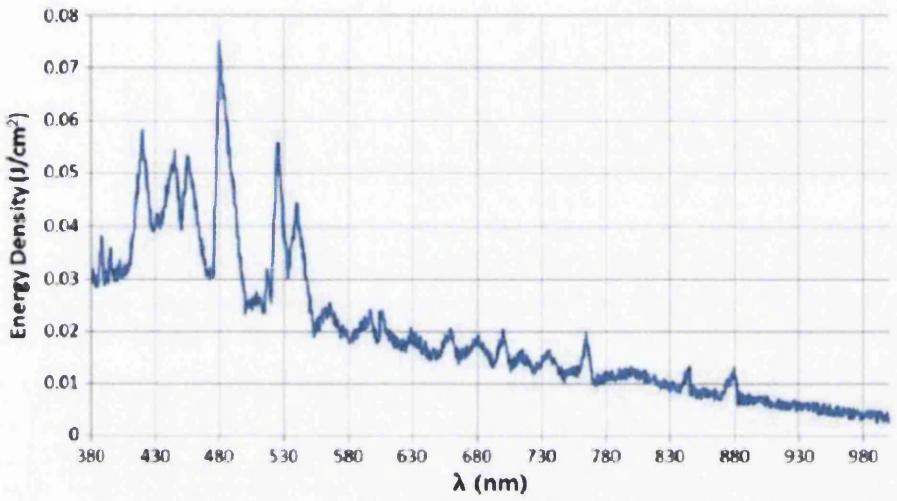

Figure 2-5 Spectral distribution of a xenon flash lamp at 50J/cm^2 between 380nm and 1000nm from reference [80]

The motivation behind IPL sintering is that metal nanoparticles are generally black and therefore light absorbing [81]. They have a large surface area to mass ratio and consequently require little radiation to heat the particles. A continuous source of radiation should heat up the particles but within a few milliseconds they will transfer heat to thermally equilibrate with the substrate. In theory, if a large enough pulse of energy is transferred, in a time shorter than the thermal equilibrium time of the particles and substrate, then the nanoparticles can sinter before much energy is transferred to the substrate. A typical absorbance and reflectance spectra for a silver nanoparticle ink is shown in Figure 2-6.

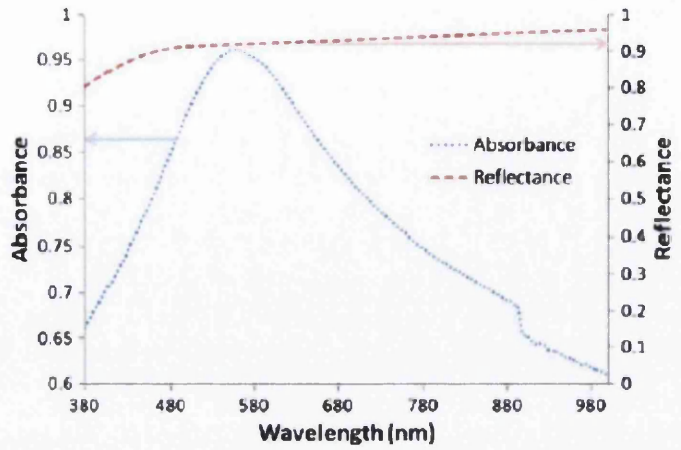

Figure 2-6 Absorbance and reflectance of an unsintered silver nanoparticle ink (diameter20-40nm) measured using UV-Vis spectroscopy from reference [80]

Schroder *et al* [78] reported that they sintered both silver and copper nanoparticle films claiming resistivity values of 4 x and 40 x bulk respectively. The best values presented in the paper for silver nanoparticles are ~30 x bulk silver for a 100μs pulse and 40 x bulk copper for a 30μs pulse with film thicknesses of 2.5μm. They claim that for a silver nanoparticle film the ideal radiant energy is of the order 1 J/cm^2 per millisecond to sinter a film 0.5-5μm thick.

Kim *et al* [82] used IPL to sinter dried copper nanoparticles (diameter 5nm), using a xenon flash lamp, and achieved 3 x bulk resistivity in 2ms at an intensity of 50 J/cm^2. They used a variety of polymer films, including polyethylene and polypropylene. It was found that the particles only sintered when the intensity was above 30 J/cm^2 and that the resistivity has an inverse relationship to intensity.

Kang *et al* [80] sintered silver nanoparticles (diameter 20-40nm) which were inkjet printed (tracks of ~0.4 x 11 mm and ~10μm thickness) onto a glass-fibre reinforced polymer composite laminate. The dried samples were subjected to one (4ms), two (4ms + 6ms) or three (4ms + 6ms + 6ms) pulses at an intensity of 50 J/cm^2. Resistivity values of 11.7, 5.6 and 2.9 x bulk silver respectively are reported.

Lee *et al* [79] investigated the effect of different line widths (150, 300 and 500μm) when using IPL to sinter inkjet printed silver nanoparticles (diameter 3-7nm). The ink was sintered with 3 x 5ms pulses. They found that the morphology changed significantly when the intensity and width is changed. The thinner lines started to sinter at lower intensities but at higher intensities swelling occurred causing ruptures. Wider films saw no remarkable changes in morphology, compared to narrower ones, except at higher intensities. The reason for the morphology changes is explained as being due to the pulses. The first pulse is absorbed by the top layer of nanoparticles, producing a thin metallic film. When the second and third pulses are applied the un-sintered nanoparticles beneath begin to sinter due to heat transfer from the film surface. At the same time the organics left in the ink vaporize leading to swelling.

West *et al* [83] report that a silver nanoparticle ink film can reach a density which is 84% that of bulk silver after IPL sintering of ~900μs. They also report that for IPL sintering the light absorption in uncured silver nanoparticle films is not primarily due to surface plasmon resonance and is instead a broadband effect across the spectrum.

Photonic sintering appears to be an excellent method for rapidly sintering metallic nanoparticle inks extremely rapidly, with speeds of up to 100 m/min claimed, offering a technology which is well suited to R2R manufacturing. A wide variety of substrates can be used, including low cost polymer foils such as PET. However, there are several disadvantages: Firstly, the ink has to be 'dry', with the bulk solvent evaporated, before sintering under the flash lamps. Secondly, the amount of electrical power required is huge as the capacitors need constant charging to thousands of volts. Total system power is in the region of megawatts (16MW quoted by NovaCentrix).

2.3.3.3 Hybrid sintering systems

There are several examples of hybrid methods where several of the methods mentioned in this review are used in tandem to 'enhance' the sintering process. Both methods here are reported by the Schubert group.

The first method is proposed by Perelaer *et al* [84] and combines plasma and microwave flash sintering. The motivation behind the work is to reduce the sintering process temperature to below the glass transition temperature of a PEN substrate. Plasma and microwave flash sintering have been described earlier in this chapter. Using low pressure argon plasma the inkjet printed silver nanoparticle ink (diameter 10nm) was given a low conductivity of at least 0.1% of bulk silver after a plasma exposure of 8 minutes at 150W. After the plasma pre-sintering the samples were microwave flash sintered for 1 second at a power of 1W. Longer process times in the microwave caused substrate damage. The best resistivity achieved was 5 x bulk silver. There are the same disadvantages to the microwave and plasma processes as described previously: Antennae structures were needed to be present on the sample to absorb the microwaves. Microwave sintering requires the placing of the sample into a chamber. Plasma sintering was carried out in an inert atmosphere under vacuum. Process time is large at 8 minutes and 1 second. This combination of factors makes the use of these processes for rapid R2R manufacturing even less relevant.

Perelaer *et al* [85] reported using IPL and microwave flash sintering together to reduce the process time by lowering the time required for the pre-sintering step where the ink film is dried, removing the bulk solvent. This step often takes at least 10 minutes and at a temperature that will not induce sintering, usually about 110°C. An inkjet printed silver nanoparticle ink (diameter 30-50nm) was pre-sintered using IPL. Multiple pulses were required to dry and start to sinter the wet ink, taking about 10 seconds. This resulted in a resistivity of 3.5 x bulk silver. Similar results were achieved in by pre-sintering the ink in an oven at 140°C, taking 40 seconds. To

decrease the resistivity further the samples were placed into a microwave (2.46GHz) and sintered at 1W for 1 second. This further reduced the resistivity to 2.3 x bulk silver. IPL was used to pre-sinter the ink from wet reducing process time by a factor of four when compared to using an oven. The total process time using a combination of IPL and microwave flash was within 15 seconds from wet ink to sintered ink film. This makes this process within a timeframe suitable for R2R manufacturing, although using a microwave sintering step seems pointless when the photonic process could be used on its own producing a nearly fully sintered film in 10 seconds. Increasing the number pulses to continue the 'pre-sinter' step would surely render the microwave step redundant.

2.3.3.4 Summary of alternative sintering techniques

For high speed R2R manufacturing there are only two alternative sintering methods that have potential to be implemented; infrared and photonic.

Laser sintering is too slow and prohibitively expensive. Microwave sintering is impractical as it cannot be implemented inline. Plasma sintering is impractical as it requires an argon atmosphere under vacuum. Electrical sintering requires electrodes to be in contact with the ink to conduct the current for joule heating to occur.

All the methods, with the exception of IR, require the ink film to be dried before the sintering process. This means that a drying stage has to be implemented and increasing the process time.

The mechanism of IR sintering relies on the organics in the ink vehicle absorbing the radiation and dissipating the energy through the system facilitating sintering. This means that the process works as a single stage dying and sintering step making it simple to implement for R2R. Process time has been quoted as being around 10 seconds.

By contrast the mechanism for photonic sintering relies on the plasmon resonance of the nanoparticles absorbing the radiation and thermally conducting the energy to other particles as sintering takes place. Process time for this sintering step can be of the order of several microseconds. However, the IPL process requires the bulk solvents to have been removed from the ink system, making the process multi-stage. Photonic sintering has been shown to be capable of drying and initiating sintering of a wet silver nanoparticle ink and achieving a process time of ~10 seconds, which would make the process single-step and more suitable for R2R.

For R2R manufacturing either IR or photonic methods can be used for processing a printed metallic nanoparticle ink from wet to sintered film in a single stage process.

2.3.4 Closure

This part of the literature review has reviewed the reported methods for nanoparticle sintering and discuss the methods reported in the literature for facilitating the sintering of metallic nanoparticle inks for potential use in a R2R manufacturing process.

Many of the current methods for sintering the nanoparticle inks are not practical for R2R manufacturing: Thermal and room temperature methods are too slow. Lasers are expensive and require the ink to be dry prior to sintering. Microwave and plasma sintering also require a pre-sintering drying step. Infrared drying and sintering is a single step but the process times are too long. Electrical sintering requires direct contact with the ink film which could damage the film. Photonic sintering, whilst rapid, requires the ink film to be dried prior to sintering. If a method could be developed to dry and sinter an ink film in a single step rapidly, in a non-contact way and with low setup costs then it could be of major benefit to the printed electronics industry, not just for metalizing DSCs..A summary of the nanoparticle sintering processes is shown in Table 2-2.

A best process time is shown for either IR or photonic sintering methods taking an ink film from wet to sintered in about 10 seconds. For a line speed of 100 m/min this still equates to a furnace length which is 60m long. A method which would reduce this processing time would be of great benefit to the high speed, volume manufacturing of printed electronics.

Table 2-2 Summary of the metallic nanoparticle conductive ink sintering methods

Method	Pre-sintering step	Pre-sintering time (min)	Pre-sintering temperature (°C)	Sintering time (mins unless stated)	Sintering temperature (°C)	Headline ratio of resistivity to bulk metal	R2R Capability
Thermal	No	n/a	n/a	5-60	100-400	10	Yes
Room Temperature	No	n/a	n/a	>60	~25	2.4	No
Laser	Yes	10	60-150	Fast	-	3	Yes
Microwave	Yes	1-5	80-150	1s – 1min	~200	3	No
Plasma	Yes	-	120	60-120	-	3	No
Infrared (Mid)	No	n/a	n/a	2 – 3	-	<10	Yes
Infrared (Short)	No	n/a	n/a	<20s	-	<10	Yes
Electrical	Yes	-	-	2μs	-	1.7	Yes
Photonic	Yes	5-10	~25-85	<30ms	-	3	Yes

2.4 Conclusions

In section 2.1 substrates for flexible DSCs and metallization methods for depositing current collectors were reviewed. Metals are more suitable than plastics for WE substrates due to the high temperature sintering of TiO_2. Metals shown to be most suitable are titanium or stainless steel with cells produced with titanium WEs demonstrated to perform better than stainless steel. Common plastics used include ITO coated PET and PEN.

Deposition methods for metallization of DSCs are not well reported in the literature. Screen printing of a conductive ink and nickel electroplating are the only reported techniques, with both methods used in conjunction with glass substrates. Screen printing is generally used to deposit thick-films so alternative thin-film printing methods could be investigated. There are also cost justifications for investigating thin-film methods as the cost of silver, the most commonly used metal in conductive inks, is becoming prohibitively expensive (see Chapter 1).

In section 2.2 nanoparticle conductive ink processing was reviewed. Nanoparticle inks offer printed thin-film metallization and the sintering mechanism is well understood. The printing technology most reported for depositing nanoparticle inks is ink jet, which is not a rapid R2R technology. Of the reported techniques for sintering only intense pulsed light (IPL) and IR are methods which facilitate R2R manufacturing. IPL can sinter nanoparticle films in microseconds but requires the ink film to be dry and the drying process takes several minutes. Using IR a nanoparticle ink film can be sintered from wet in ~20s. A method which could process a nanoparticle ink from wet to dry in less than 20s would offer a significant contribution to the manufacturing of printed electronics.

2.5 References

1. Papageorgiou, N., W.F. Maier, and M. Gratzel, *An iodine/triiodide reduction electrocatalyst for aqueous and organic media.* Journal of The Electrochemical Society, 1997. **144**(3): p. 876-884.
2. Zardetto, V., T.M. Brown, A. Reale, and A. Di Carlo, *Substrates for flexible electronics: A practical investigation on the electrical, film flexibility, optical, temperature, and solvent resistance properties.* Journal of Polymer Science Part B: Polymer Physics, 2011. **49**(9): p. 638-648.
3. Pichot, F., J.R. Pitts, and B.A. Gregg, *Low-temperature sintering of TiO2 colloids: Application to flexible dye-sensitized solar cells.* Langmuir, 2000. **16**(13): p. 5626-5630.
4. Kijitori, Y., M. Ikegami, and T. Miyasaka, *Highly efficient plastic dye-sensitized photoelectrodes prepared by low-temperature binder-free coating of mesoscopic titania pastes.* Chemistry Letters, 2007. **36**(1): p. 190-191.
5. Miyasaka, T., M. Ikegami, and Y. Kijitori, *Photovoltaic performance of plastic dye-sensitized electrodes prepared by low-temperature binder-free coating of mesoscopic titania.* Journal of The Electrochemical Society, 2007. **154**(5): p. A455-A461.
6. Santa-Nokki, H., J. Kallioinen, T. Kololuoma, V. Tuboltsev, and J. Korppi-Tommola, *Dynamic preparation of TiO2 films for fabrication of dye-sensitized solar cells.* Journal of Photochemistry and Photobiology a-Chemistry, 2006. **182**(2): p. 187-191.
7. Lindstrom, H., A. Holmberg, E. Magnusson, S.E. Lindquist, L. Malmqvist, and A. Hagfeldt, *A new method for manufacturing nanostructured electrodes on plastic substrates.* Nano Letters, 2001. **1**(2): p. 97-100.
8. Durr, M., A. Schmid, M. Obermaier, S. Rosselli, A. Yasuda, and G. Nelles, *Low-temperature fabrication of dye-sensitized solar cells by transfer of composite porous layers.* Nature Materials, 2005. **4**(8): p. 607-611.
9. Lindstrom, H., A. Holmberg, E. Magnusson, L. Malmqvist, and A. Hagfeldt, *A new method to make dye-sensitized nanocrystalline solar cells at room temperature.* Journal of Photochemistry and Photobiology a-Chemistry, 2001. **145**(1-2): p. 107-112.
10. Fang, X.M., T.L. Ma, G.Q. Guan, M. Akiyama, T. Kida, and E. Abe, *Effect of the thickness of the Pt film coated on a counter electrode on the performance of a dye-sensitized solar cell.* Journal of Electroanalytical Chemistry, 2004. **570**(2): p. 257-263.
11. Hauch, A. and A. Georg, *Diffusion in the electrolyte and charge-transfer reaction at the platinum electrode in dye-sensitized solar cells.* Electrochimica Acta, 2001. **46**(22): p. 3457-3466.
12. Jun, Y., J. Kim, and M.G. Kang, *A study of stainless steel-based dye-sensitized solar cells and modules.* Solar Energy Materials and Solar Cells, 2007. **91**(9): p. 779-784.

13. Kang, M.G., N.G. Park, K.S. Ryu, S.H. Chang, and K.J. Kim, *A 4.2% efficient flexible dye-sensitized TiO2 solar cells using stainless steel substrate.* Solar Energy Materials and Solar Cells, 2006. **90**(5): p. 574-581.
14. Park, J.H., Y. Jun, H.-G. Yun, S.-Y. Lee, and M.G. Kang, *Fabrication of an efficient dye-sensitized solar cell with stainless steel substrate.* Journal of The Electrochemical Society, 2008. **155**(7): p. F145-F149.
15. Ito, S., N.-L.C. Ha, G. Rothenberger, P. Liska, P. Comte, S.M. Zakeeruddin, P. Pechy, M.K. Nazeeruddin, and M. Graetzel, *High-efficiency (7.2%) flexible dye-sensitized solar cells with Ti-metal substrate for nanocrystalline-TiO2 photoanode.* Chemical Communications, 2006(38): p. 4004-4006.
16. Kim, S.S., Y.C. Nah, Y.Y. Noh, J. Jo, and D.Y. Kim, *Electrodeposited Pt for cost-efficient and flexible dye-sensitized solar cells.* Electrochimica Acta, 2006. **51**(18): p. 3814-3819.
17. Nemoto, J., M. Sakata, T. Hoshi, H. Ueno, and M. Kaneko, *All-plastic dye-sensitized solar cell using a polysaccharide film containing excess redox electrolyte solution.* Journal of Electroanalytical Chemistry, 2007. **599**(1): p. 23-30.
18. Ma, T., X. Fang, M. Akiyama, K. Inoue, H. Noma, and E. Abe, *Properties of several types of novel counter electrodes for dye-sensitized solar cells.* Journal of Electroanalytical Chemistry, 2004. **574**(1): p. 77-83.
19. LindstrÃ¶m, H., A. Holmberg, E. Magnusson, L. Malmqvist, and A. Hagfeldt, *A new method to make dye-sensitized nanocrystalline solar cells at room temperature.* Journal of Photochemistry and Photobiology A: Chemistry, 2001. **145**(1â€"2): p. 107-112.
20. Haque, S.A., E. Palomares, H.M. Upadhyaya, L. Otley, R.J. Potter, A.B. Holmes, and J.R. Durrant, *Flexible dye sensitised nanocrystalline semiconductor solar cells.* Chemical Communications, 2003(24): p. 3008-3009.
21. Miettunen, K., I. Asghar, X. Ruan, J. Halme, T. Saukkonen, and P. Lund, *Stabilization of metal counter electrodes for dye solar cells.* Journal of Electroanalytical Chemistry. **653**(1-2): p. 93-99.
22. Toivola, M., F. Ahlskog, and P. Lund, *Industrial sheet metals for nanocrystalline dye-sensitized solar cell structures.* Solar Energy Materials and Solar Cells, 2006. **90**(17): p. 2881-2893.
23. Chang, H., T.L. Chen, K.D. Huang, S.H. Chien, and K.C. Hung, *Fabrication of highly efficient flexible dye-sensitized solar cells.* Journal of Alloys and Compounds. **504**: p. S435-S438.
24. Onoda, K., S. Ngamsinlapasathian, T. Fujieda, and S. Yoshikawa, *The superiority of Ti plate as the substrate of dye-sensitized solar cells.* Solar Energy Materials and Solar Cells, 2007. **91**(13): p. 1176-1181.
25. Toivola, M., J. Halme, K. Miettunen, K. Aitola, and P.D. Lund, *Nanostructured dye solar cells on flexible substrates-Review.* International Journal of Energy Research, 2009. **33**(13): p. 1145-1160.
26. Philip, B., *Investigation of metal substrates for photovoltaic applications.* 2010, Swansea University.

27. Sastrawan, R., J. Beier, U. Belledin, S. Hemming, A. Hinsch, R. Kern, C. Vetter, F.M. Petrat, A. Prodi-Schwab, P. Lechner, and W. Hoffmann, *A glass frit-sealed dye solar cell module with integrated series connections.* Solar Energy Materials and Solar Cells, 2006. **90**(11): p. 1680-1691.
28. Firor, K. and S. Hogan, *ENVIRONMENTAL TESTING OF SINGLE-CRYSTAL SILICON SOLAR-CELLS WITH SCREEN-PRINTED SILVER CONTACTS.* Ieee Transactions on Reliability, 1982. **31**(3): p. 270-275.
29. Frisson, L., P. Lauwers, R. Mertens, R. Vanoverstraeten, and R. Govaerts, *SCREEN PRINTED METALLIZATION OF SILICON SOLAR-CELLS.* Electrocomponent Science and Technology, 1980. **7**(1-3): p. 107-111.
30. Ju, M., Y.-J. Lee, J. Lee, B. Kim, K. Ryu, K. Choi, K. Song, K. Lee, C. Han, Y. Jo, and J. Yi, *Double screen printed metallization of crystalline silicon solar cells as low as 30 mu m metal line width for mass production.* Solar Energy Materials and Solar Cells. **100**: p. 204-208.
31. Vitanov, P., N. Tyutyundzhiev, P. Stefchev, and B. Karamfilov, *Low cost multilayer metallization system for silicon solar cells.* Solar Energy Materials and Solar Cells, 1996. **44**(4): p. 471-484.
32. Frey, M., F. Clement, S. Dilfer, D. Erath, and D. Biro, *Front-side Metalization By Means Of Flexographic Printing*, in *Proceedings of the Siliconpv 2011 Conference*, S. Glunz, et al., Editors. p. 581-586.
33. Lee, W.J., E. Ramasamy, D.Y. Lee, and J.S. Song, *Glass frit overcoated silver grid lines for nano-crystalline dye sensitized solar cells.* Journal of Photochemistry and Photobiology a-Chemistry, 2006. **183**(1-2): p. 133-137.
34. Okada, K., H. Matsui, T. Kawashima, T. Ezure, and N. Tanabe, *100 mm x 100 mm large-sized dye sensitized solar cells.* Journal of Photochemistry and Photobiology a-Chemistry, 2004. **164**(1-3): p. 193-198.
35. Blom, P. and T. van Mol, *LEDs are on a roll*, in *Physics World.* November 2011, IOP.
36. Yang, N.J. and K. Aoki, *Voltammetry of the silver alkylcarboxylate nanoparticles in suspension.* Electrochimica Acta, 2005. **50**(25-26): p. 4868-4872.
37. Yao, J.H., K.R. Elder, H. Guo, and M. Grant, *Late stage droplet growth.* Physica A: Statistical Mechanics and its Applications, 1994. **204**(1â€“4): p. 770-788.
38. Liang, L.H., C.M. Shen, S.X. Du, W.M. Liu, X.C. Xie, and H.J. Gao, *Increase in thermal stability induced by organic coatings on nanoparticles.* Physical Review B, 2004. **70**(20).
39. Ratke, L. and P.W. Voorhees, *Growth and Coarsening: Ostwald Ripening in Material Processing.* Vol. 1. 2002: Springer.
40. Datye, A.K., Q. Xu, K.C. Kharas, and J.M. McCarty, *Particle size distributions in heterogeneous catalysts: What do they tell us about the sintering mechanism?* Catalysis Today, 2006. **111**(1-2): p. 59-67.
41. Greer, J.R. and R.A. Street, *Thermal cure effects on electrical performance of nanoparticle silver inks.* Acta Materialia, 2007. **55**(18): p. 6345-6349.
42. Greenwood, N.N. and A. Earnshaw, *Chemistry of the Elements.* 1997: Elsevier Science & Technology Books.

43. Gonzalez, A.L. and C. Noguez, *Optical properties of silver nanoparticles*, in *Physica Status Solidi C - Current Topics in Solid State Physics, Vol 4, No 11*, S.E. Ulloa and P.P. Prieto, Editors. 2007. p. 4118-4126.
44. Hutter, E., J.H. Fendler, and D. Roy, *Surface plasmon resonance studies of gold and silver nanoparticles linked to gold and silver substrates by 2-aminoethanethiol and 1,6-hexanedithiol.* Journal of Physical Chemistry B, 2001. **105**(45): p. 11159-11168.
45. Lee, K.C., S.J. Lin, C.H. Lin, C.S. Tsai, and Y.J. Lu, *Size effect of Ag nanoparticles on surface plasmon resonance.* Surface & Coatings Technology, 2008. **202**(22-23): p. 5339-5342.
46. Szczech, J.B., C.M. Megaridis, D.R. Gamota, and J. Zhang, *Fine-line conductor manufacturing using drop-on-demand PZT printing technology.* Ieee Transactions on Electronics Packaging Manufacturing, 2002. **25**(1): p. 26-33.
47. Park, J.-W. and S.-G. Baek, *Thermal behavior of direct-printed lines of silver nanoparticles.* Scripta Materialia, 2006. **55**(12): p. 1139-1142.
48. Lee, H.H., K.S. Chou, and K.C. Huang, *Inkjet printing of nanosized silver colloids.* Nanotechnology, 2005. **16**(10): p. 2436-2441.
49. Denneulin, A., A. Blayo, C. Neuman, and J. Bras, *Infra-red assisted sintering of inkjet printed silver tracks on paper substrates.* Journal of Nanoparticle Research, 2011. **13**(9): p. 3815-3823.
50. Perelaer, B.J., A.W.M. de Laat, C.E. Hendriks, and U.S. Schubert, *Inkjet-printed silver tracks: low temperature curing and thermal stability investigation.* Journal of Materials Chemistry, 2008. **18**(27): p. 3209-3215.
51. http://nanopchem.com/wp-content/uploads/file/DataSheets/PFI-722%20Data%20Sheet.pdf 7th August 2012
52. http://www.inktec.com/english/product_info/electronic_tec.asp 7th August 2012
53. http://www.fetc.com.tw/new_products.htm 7th August 2012
54. Grouchko, M., A. Kamyshny, C.F. Mihailescu, D.F. Anghel, and S. Magdassi, *Conductive Inks with a "Built-In" Mechanism That Enables Sintering at Room Temperature.* ACS Nano, 2011. **5**(4): p. 3354-3359.
55. Grouchko, M., A. Kamyshny, and S. Magdassi, *Formation of air-stable copper-silver core-shell nanoparticles for inkjet printing.* Journal of Materials Chemistry, 2009. **19**(19): p. 3057-3062.
56. Layani, M., M. Gruchko, O. Milo, I. Balberg, D. Azulay, and S. Magdassi, *Transparent Conductive Coatings by Printing coffee Ring Arrays Obtained at Room Temperature.* ACS Nano, 2009. **3**(11): p. 3537-3542.
57. Magdassi, S., M. Grouchko, D. Toker, A. Kamyshny, I. Balberg, and O. Millo, *Ring stain effect at room temperature in silver nanoparticles yields high electrical conductivity.* Langmuir, 2005. **21**(23): p. 10264-10267.
58. Young, H.D. and R.A. Freedman, *University physics*. 1996: Addison-Wesley Pub. Co.
59. Chung, J.W., S.W. Ko, N.R. Bieri, C.P. Grigoropoulos, and D. Poulikakos, *Conductor microstructures by laser curing of printed gold nanoparticle ink.* Applied Physics Letters, 2004. **84**(5): p. 801-803.

60. Bieri, N.R., J. Chung, D. Poulikakos, and C.P. Grigoropoulos, *Manufacturing of nanoscale thickness gold lines by laser curing of a discretely deposited nanoparticle suspension.* Superlattices and Microstructures, 2004. **35**(3-6): p. 437-444.
61. Chung, J., N.R. Bieri, S. Ko, C.P. Grigoropoulos, and D. Poulikakos, *In-tandem deposition and sintering of printed gold nanoparticle inks induced by continuous Gaussian laser irradiation.* Applied Physics a-Materials Science & Processing, 2004. **79**(4-6): p. 1259-1261.
62. Ko, S.H., H. Pan, C.P. Grigoropoulos, C.K. Luscombe, J.M.J. Frechet, and D. Poulikakos, *All-inkjet-printed flexible electronics fabrication on a polymer substrate by low-temperature high-resolution selective laser sintering of metal nanoparticles.* Nanotechnology, 2007. **18**(34): p. 8.
63. Niizeki, T., K. Maekawa, M. Mita, K. Yamasaki, Y. Matsuba, N. Terada, H. Saito, and Ieee, *Laser sintering of Ag Nanopaste film and its application to bond-pad formation*, in *58th Electronic Components & Technology Conference, Proceedings*. 2008, Ieee: New York. p. 1745-1750.
64. Lesyuk, R., W. Jillek, Y. Bobitski, and B. Kotlyarchuk, *Low-energy pulsed laser treatment of silver nanoparticles for interconnects fabrication by ink-jet method.* Microelectronic Engineering. **88**(3): p. 318-321.
65. Chiolerio, A., G. Maccioni, P. Martino, M. Cotto, P. Pandolfi, P. Rivolo, S. Ferrero, and L. Scaltrito, *Inkjet printing and low power laser annealing of silver nanoparticle traces for the realization of low resistivity lines for flexible electronics.* Microelectronic Engineering. **88**(8): p. 2481-2483.
66. Auyeung, R.C.Y., H. Kim, S.A. Mathews, and A. Pique, *Laser Direct-Write of Metallic Nanoparticle Inks.* Journal of Laser Micro Nanoengineering, 2007. **2**(1): p. 21-25.
67. Rao, K.J., B. Vaidhyanathan, M. Ganguli, and P.A. Ramakrishnan, *Synthesis of inorganic solids using microwaves.* Chemistry of Materials, 1999. **11**(4): p. 882-895.
68. Wiesbrock, F., R. Hoogenboom, and U.S. Schubert, *Microwave-assisted polymer synthesis: State-of-the-art and future perspectives.* Macromolecular Rapid Communications, 2004. **25**(20): p. 1739-1764.
69. Cheng, D.K., *Field and wave electromagnetics*. 1989: Addison-Wesley.
70. Mishra, P., G. Sethi, and A. Upadhyaya, *Modeling of microwave heating of particulate metals.* Metallurgical and Materials Transactions B-Process Metallurgy and Materials Processing Science, 2006. **37**(5): p. 839-845.
71. Perelaer, J., B.J. de Gans, and U.S. Schubert, *Ink-jet printing and microwave sintering of conductive silver tracks.* Advanced Materials, 2006. **18**(16): p. 2101-+.
72. Perelaer, J., M. Klokkenburg, C.E. Hendriks, and U.S. Schubert, *Microwave Flash Sintering of Inkjet-Printed Silver Tracks on Polymer Substrates.* Advanced Materials, 2009. **21**(47): p. 4830-+.
73. Reinhold, I., C.E. Hendriks, R. Eckardt, J.M. Kranenburg, J. Perelaer, R.R. Baumann, and U.S. Schubert, *Argon plasma sintering of inkjet printed silver tracks on polymer substrates.* Journal of Materials Chemistry, 2009. **19**(21): p. 3384-3388.

74. Niittynen, J., E. Halonen, M. Mantysalo, D. Lupo, J. Perelaer, and U.S. Schubert. *Conductivity and Adhesion Study of Plasma-sintered Nanoparticle Silver Ink.* in *LOPE-C.* 2011. Frankfurt Messe, Frankfurt.
75. Tobjörk, D., H. Aarnio, P. Pulkkinen, R. Bollstrom, A. Maattanen, P. Ihalainen, T. Makela, J. Peltonen, M. Toivakka, H. Tenhu, and R. Osterbacka, *IR-sintering of ink-jet printed metal-nanoparticles on paper.* Thin Solid Films, 2012. **520**(7): p. 2949-2955.
76. Allen, M.L., M. Aronniemi, T. Mattila, A. Alastalo, K. Ojanpera, M. Suhonen, and H. Seppa, *Electrical sintering of nanoparticle structures.* Nanotechnology, 2008. **19**(17): p. 4.
77. Hummelgard, M., R.Y. Zhang, H.E. Nilsson, and H. Olin, *Electrical Sintering of Silver Nanoparticle Ink Studied by In-Situ TEM Probing.* Plos One, 2011. **6**(2): p. 6.
78. Schroder, K.A., S.C. McCool, and W.F. Furlan. *Broadcast photonic curing of metallic nanopartiele films.* in *2006 NSTI Nanotechnology Conference and Trade Show - NSTI Nanotech 2006 Technical Proceedings.* 2006.
79. Lee, D.J., S.H. Park, S. Jang, H.S. Kim, J.H. Oh, and Y.W. Song, *Pulsed light sintering characteristics of inkjet-printed nanosilver films on a polymer substrate.* Journal of Micromechanics and Microengineering, 2011. **21**(12).
80. Kang, J.S., J. Ryu, H.S. Kim, and H.T. Hahn, *Sintering of Inkjet-Printed Silver Nanoparticles at Room Temperature Using Intense Pulsed Light.* Journal of Electronic Materials, 2011. **40**(11): p. 2268-2277.
81. Yang, Y.Q., S.F. Wang, Z.Y. Sun, and D.D. Dlott, *Propagation of shock-induced chemistry in nanoenergetic materials: The first micrometer.* Journal of Applied Physics, 2004. **95**(7): p. 3667-3676.
82. Kim, H.-S., S. Dhage, D.-E. Shim, and H. Hahn, *Intense pulsed light sintering of copper nanoink for printed electronics.* Applied Physics A: Materials Science & Processing, 2009. **97**(4): p. 791-798.
83. West, J., M. Carter, S. Smith, and J. Sears. *Photonic Curing of Silver Nanoparticle Based Inks.* in *NSTI Nanotechnology Conference and Expo.* 2010.
84. Perelaer, J., R. Jani, M. Grouchko, A. Kamyshny, S. Magdassi, and U.S. Schubert, *Plasma and microwave flash sintering of a tailored silver nanoparticle ink, yielding 60% bulk conductivity on cost-effective polymer foils.* Advanced Materials, 2012. **24**(29): p. 3993-8.
85. Perelaer, J., R. Abbel, S. Wunscher, R. Jani, T. van Lammeren, and U.S. Schubert, *Roll-to-Roll Compatible Sintering of Inkjet Printed Features by Photonic and Microwave Exposure: From Non-Conductive Ink to 40% Bulk Silver Conductivity in Less Than 15 Seconds.* Advanced Materials, 2012. **24**(19): p. 2620-2625.

3 Experimental Techniques and Equipment

3.1 Introduction

This chapter will outline the experimental techniques and equipment used in this thesis. The first section will examine the printing, coating and subsequent drying and sintering methods used to deposit and process the functional inks, the second section will detail the analysis methods used to characterise the materials used in the experiments. The third section will describe the manufacturing and analysis of dye-sensitised solar cells.

3.2 Printing and coating methods

3.2.1 Coating methods

Two methods for coating ink films are described in this section; mechanical K-bar coating and bar-coating.

3.2.1.1 Mechanical K-Bar coating

A common method for applying a coating to a substrate is using a k-bar [1]. An RK automatic K-bar coater [2] was used to deposit ink films(see Figure 3-1). A bar is used to draw ink over a substrate at a constant speed and pressure. The bars are produced by winding steel wire over a steel rod, leaving a regular series of grooves, which control the wet ink film thickness (WFT). Different WTFs can be achieved by using bars with wound wires of different diameters. The backing surface is a Melinex/foam/rubber combination.

Samples of dimensions of ca. 80mm x 100mm were coated at an arbitrary speed of 3 (defined as the number on the speed control dial) using a Meyer bar 1, which

gives a nominal WFT of 6μm. The repeatability of the coating is referred to in Chapter 6.

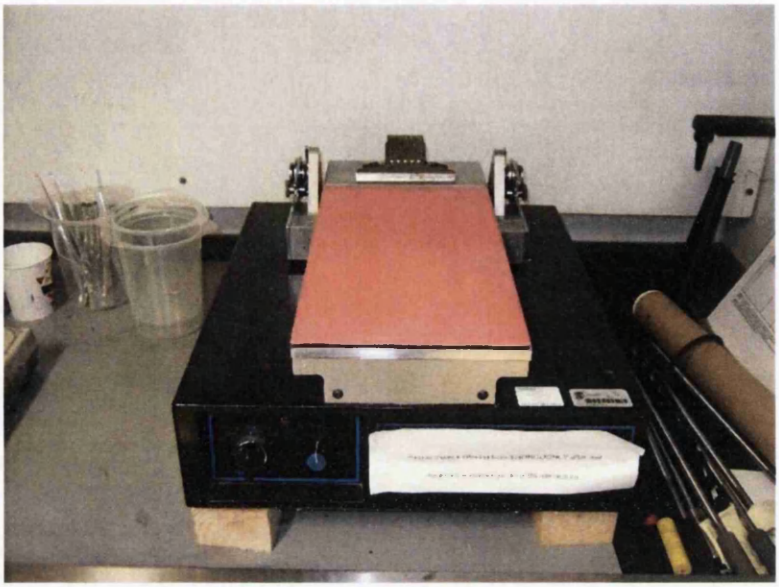

Figure 3-1 An RK control coater

3.2.1.2 Bar-coating

Where experiments were carried out away from the university, where there were no coating apparatus available, it was necessary to use a simple coating method which could be transported easily. It was decided to use a bar-casting method similar to that used in TiO_2 deposition for DSC electrodes [3]. It is reproducible method for coating a large area. A schematic of the process is shown in Figure 3-2.

Usually in DSC preparation the substrate is glass and an impression sheet is not required. Here the substrate is plastic so a flat stainless steel impression sheet was used. Substrate was mounted onto a flat stainless steel sheet and attached using 3M Scotch tape (thickness 50μm) across the top with two strips of tape were placed lengthways down the substrate. This created a mask with a 30mm x 80mm area with the thickness of the ink film controlled by the tape. Ink was applied onto the top edge of the tape and a glass bar was drawn-down by hand

from above the ink to the bottom of the substrate coating it. The tape was subsequently removed and the now coated substrate was ready for drying and sintering. See Chapter 6 for information on the repeatability of the process.

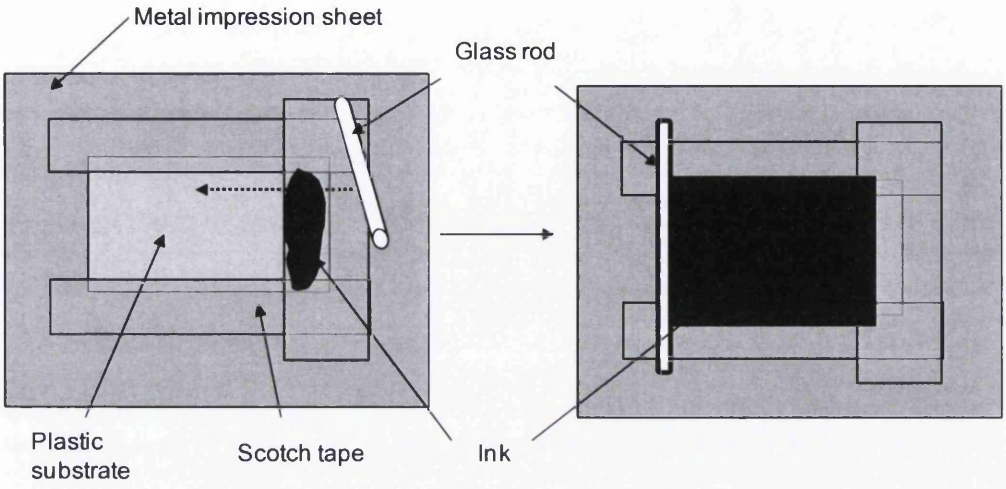

Figure 3-2 Schematic of the bar-casting process

3.2.2 Flexographic printing – IGT F1

The IGT F1 printability tester (see Figure 3-3) is designed to simulate the flexographic printing process [4]. It is a commonly used method for laboratory testing [5-7]. It comprises of an anilox roll, reverse angle doctor blade, printing cylinder and an impression cylinder. The photopolymer printing plate is attached to the printing cylinder using mounting tape, as per a full size press. The plate width is just 50mm, which limits the maximum image width to 40mm. The substrate is mounted onto a rigid substrate carrier and secured using tape.

To print, the anilox is brought into contact with the plate cylinder. Ink is then applied directly onto the anilox behind the doctor blade. The drive of the plate cylinder rotates the anilox which facilitates the simultaneous inking up of the plate and anilox. The cylinder can be set to rotate for a number of rotations to ensure a uniform ink deposit. Once this number of rotations has completed the plate cylinder moves into contact with the substrate by engaging the impression cylinder. The drive of the plate cylinder pulls the substrate carrier through the printing nip. Whilst printing is in progress the anilox remains in contact with the

plate cylinder ensuring that the plate is continually inked up. Once the print is completed all contacts then disengage.

Print speed, impression forces, both plate to substrate and anilox to plate, as well as doctoring settings can all be altered.

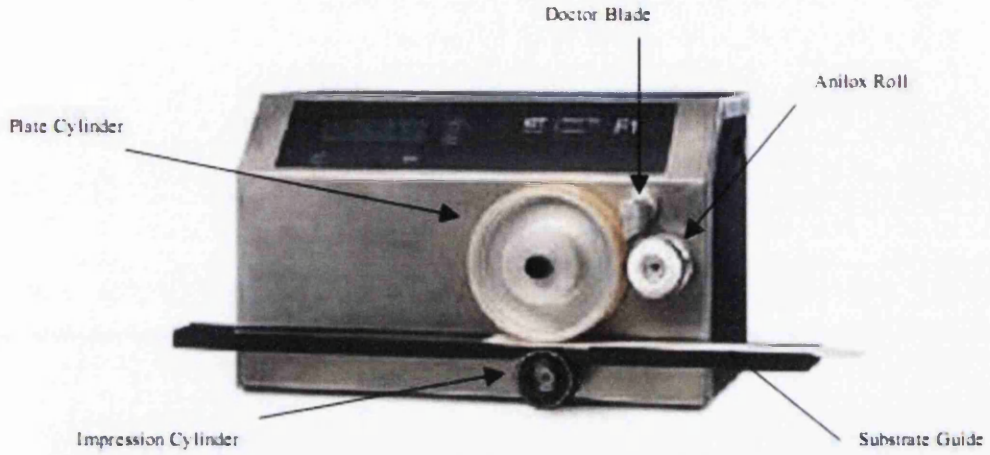

Figure 3-3 F1 Printability tester

The convention for using solvent based inks is to clean all components after each print to prevent particles in the ink 'drying in' to the anilox cells and ink drying on the plate. However, in this study, cleaning after each print would not be practicable due to the large number of experimental samples required. To overcome the cleaning issue a minimum of three persons were present for experiments. All substrate was pre-cut and once printing started the process was constant until experiments were completed. One advantage that this continuous printing run had was that the process was stabilised after the first few prints overcoming the issues that Cherry highlighted [8].

The IGT F1 printability tester is representative of the flexographic process but it differs to a full size press in that the samples are passed through the nip via a friction contact because the printing cylinder pulls the substrate guide through. On a full press the substrate is driven by the web feed. A result of this is that printing pressures are larger than would be seen on a full press which increases ink spreading. The repeatability of the process is referred to in Chapter 4.

3.2.3 Flatbed screen printing

The DEK 248 is a semi-automatic flatbed screen printing press (see Figure 3-4) designed for the manufacture of printed circuit boards. The substrate is carried on a vacuum table which has a vision system for the accurate registration of multiple layers. The main housing contains the screen which is secured into the press by four support pins attached to the frame. A flow coat and squeegee are mounted directly onto the printing head above the screen. Printing pressure is manually controlled by a dial on the printing head. All other process parameters are set in the software. Full operational method is described in the manufacturers' handbook [9]. For the repeatability of the process see Chapter 4.

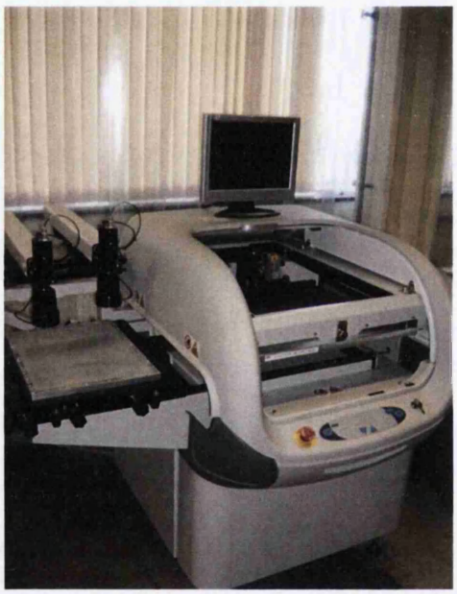

Figure 3-4 DEK 248 press

3.3 Ink drying and sintering

In chapter 2 the various methods for drying and sintering nanoparticle conducting inks were discussed. To provide a comparison between methods three different ways of drying/sintering are used; Thermal drying in an oven and radiative methods using IR drying using mid-IR emitters and NIR emitters.

3.3.1 Conventional oven

A Heraeus Vacutherm VT6025 hot-air oven, with digital temperature control, was used for all conventional oven drying [10]. The oven was allowed to stabilise for an hour prior to use due to the ceramic lining in the oven surround. Samples were dried at atmospheric pressure at a specified time and temperature.

3.3.2 Infrared (IR or MIR) Drying

Infrared radiation causes vibrations in the bonds of functional groups within a material. These vibrations cause thermal agitation of heat. Mid-IR is being used as a drying method on the TATA Steel's PV Accelerator pilot-line to decrease the process time for several of the functional layers in a DSC. Mid-IR drying was carried out using an SC Driers UV/IR/Convection combination belt furnace. The unit was set at 140°C with the IR lamps on at 100% power for a minimum of 15 minutes prior to experiments to ensure the temperature throughout was constant. Dwell time in the furnace was controlled by the manual speed dial and preset.

3.3.3 Near infrared (NIR) radiation

3.3.3.1 Introduction to NIR

NIR drying is a relatively new technology which has been investigated for use in a variety of applications, such as paint curing for continuous coil coating [11, 12] and rapid sintering of TiO_2 pastes for application in DSCs [3]. NIR is the region of the electromagnetic spectrum situated between the visible and IR regions in the waveband of 800-1500nm (Figure 3-5). An NIR emitter produces a large energy density across a relatively short waveband which means that objects can be selectively irradiated.

This section will outline the equipment used for NIR drying and characterise the emitter output in two ways; through a model based on blackbody theory and measured using a spectrometer.

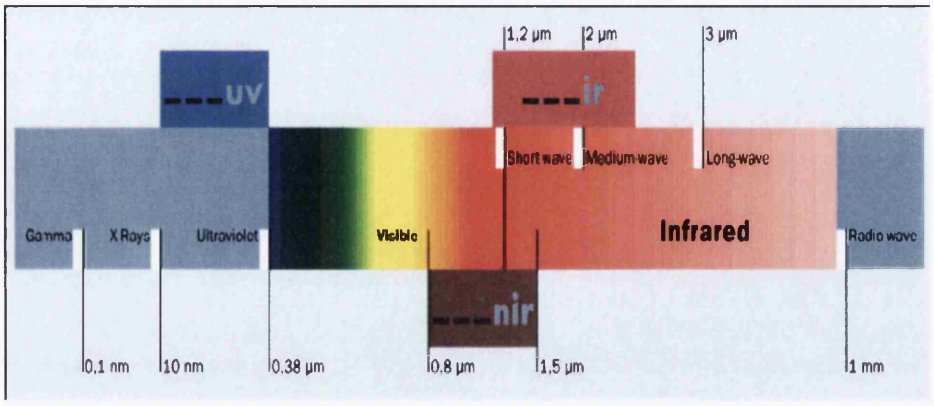

Figure 3-5 The electromagnetic spectrum

3.3.3.2 Laboratory unit operation

The NIR system used for experiments in this thesis was the AdPhos NIR/IR Coil lab LV2. It consists of one lamp module, containing 6 x HB-NIR emitters with variable output power settings and a variable speed conveyor with a sample holder attached, shown in Figure 3-6.

Figure 3-6 Adphos NIR/IR Coil lab LV2

Extraction is required over the entry and exit of the emitter housing. Samples using polymer foil substrates are mounted onto a PTFE block, of dimensions 200mm x 100mm, which is placed in the metal sample holder. The line speed and emitter powers are set by the operator using a touch screen control panel.

The heat transfer and temperature rise of samples were not able to be measured. Two methods were attempted: Firstly, thermocouples were attached to the samples but the thermocouples absorbed the NIR which caused damage to the polymer substrates. Secondly, an IR camera was tested but the NIR intensity was too large and saturated the detectors.

3.3.3.3 NIR Emitter characterisation

To better understand the energy emitted by the HB-NIR emitters the output has been characterised in two ways; firstly, by using a theoretical model based on blackbody radiation theory and secondly, by using a portable UV/VIS/NIR spectrometer to empirically measure the output.

3.3.3.3.1 Theoretical blackbody model

The output of the HB-NIR emitters was initially modelled according to blackbody theory [13] and this section describes the model.

The model is created by using Planck's law to calculate the spectral radiance at each wavelength interval. The missing piece of information required in the equation is the emitter temperature. The colour temperature of a Tungsten-halogen lamp, corrected for the ratio of input voltage/nominal voltage is used to approximate the emitter temperature. Data for the electrical inputs and colour temperature was supplied by the emitter suppliers Adphos, see Table 3-1.

Table 3-1 Modeled spectral emittance key data

Emitter power (%)	**Colour temperature (K)**	**Voltage corrected temperature (K)**	**Peak wavelength λ_m (nm)**	**Spectral emittance at λ_m ($Wm^{-2}nm^{-1}$)**
100	3200	3140	923	1.34×10^{-6}
50	3200	2430	1192	3.71×10^{-7}
30	3200	2010	1442	1.44×10^{-7}

The spectral emittance of the HB-NIR emitter is modelled in Figure 3-7 for different emitter powers using the temperatures presented in Table 3-1. The model predicts that the peak wavelength will increase as filament temperature decreases.

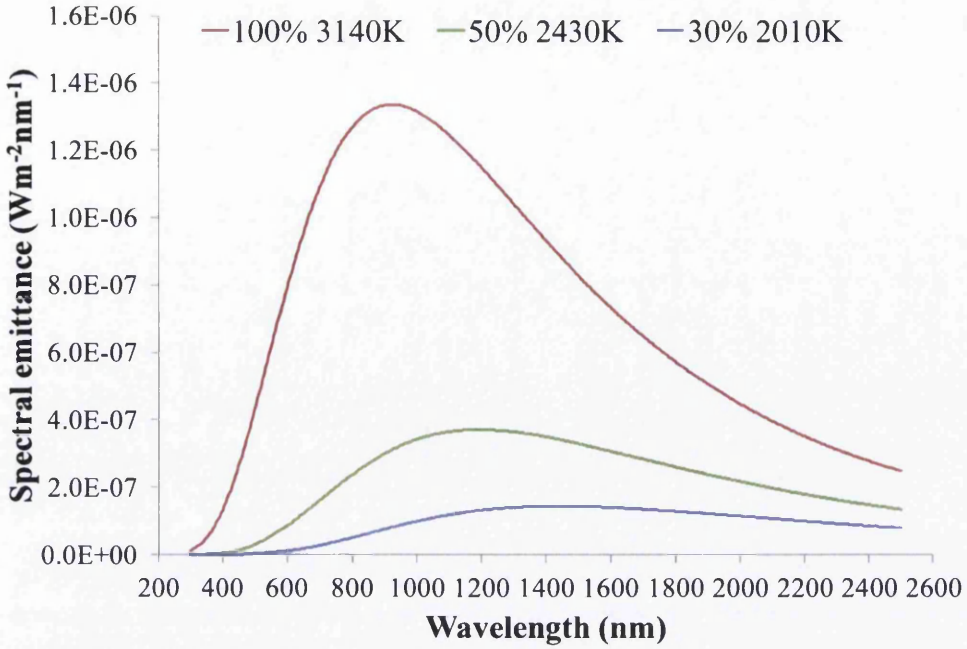

Figure 3-7 Modeled spectral emittance for Adphos HB-NIR emitters at 100%, 50% and 25% power

3.3.3.3.2 Empirical spectroscopic measurements

The empirical spectral emittance was measured using Ocean Optics portable spectrometers; HR2000+ UV/VIS and NIRQUEST256 NIR. Both spectrometers were used simultaneously using a fibre optic input fibre with splitter cable with a cosine corrector attached to the input fibre. Details on the operation of the Ocean Optics spectrometers can be found in the handbook [14].

Both spectrometers were calibrated using a Deuterium Tungsten-Halogen calibration light source (DH-2000-CAL) from Ocean Optics and calibration files supplied by Ocean Optics. A calibration is valid for as long as the fibre optic input cable remains attached the SMA connector.

To measure the total absolute irradiance and spectral emittance of the HB-NIR emitters from the Adphos NIR/IR Coil lab LV2 the sample stage from the coil lab unit was first removed to prevent the stage impacting the optical fibre. The input fibre, with cosine corrector attached, was positioned on the exit side of the

lamp housing and clamped into position perpendicular to the emitters at a vertical distance of 100mm and a horizontal distance of 50mm. Due to the high temperatures emitted from the lamps it was not practical to place the collecting fibre any closer to the emitters so as not to risk thermal damage to the fibre and cosine corrector. The spectrometers were then setup using the spectra suite software and integration time was automatically set. Prior to measuring the emitters were set at the desired power setting and the speed set at 1m/min giving an emitter run time of approximately 30 seconds. The emitters were run twice before a spectral measurement was taken to ensure the emitter filaments were sufficiently warm.

Previous work carried out with Dr. I. Mabbett and Ms. C. Gowenlock in Swansea University Materials Engineering department measured the UV/Vis output of the HB-NIR emitters [11]. This data gave an idea of the energy outputted by the emitters but for a limited waveband which did not include the NIR region of the spectrum.

The absolute irradiance for the HB-NIR emitters in the AdPhos Coil Lab LV2 between 500-2000nm is shown in Figure 3-8 for 100%, 50% and 30% emitter powers. The empirical data shows that the emitters have peak irradiance in the NIR.

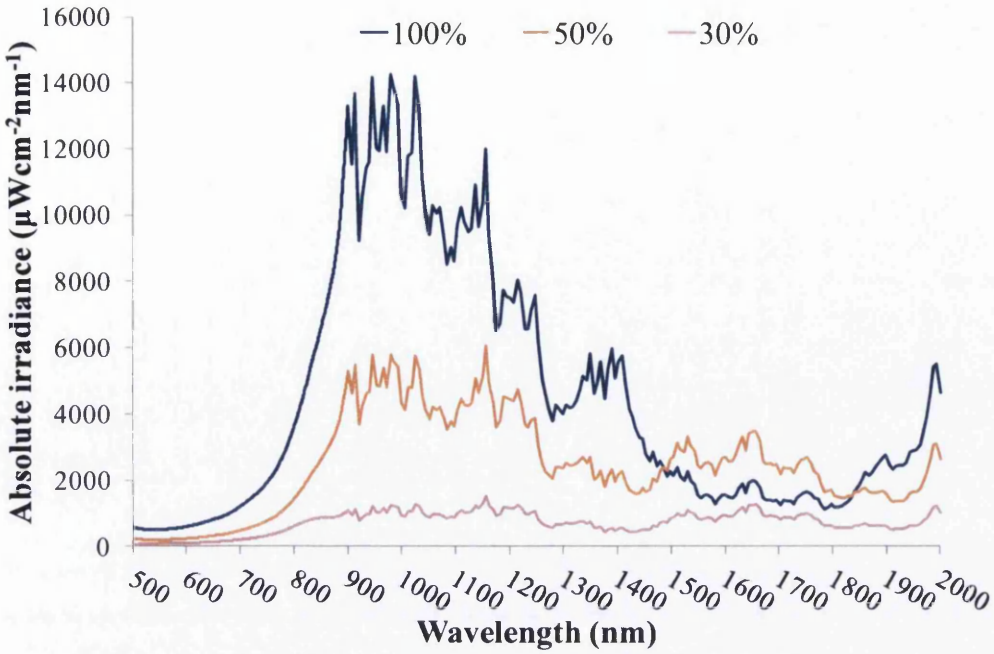

Figure 3-8 Empirical absolute irradiance of HB-NIR emitters

A comparison between the theoretical peak wavelength and the actual peak wavelength and the outputs at these peak wavelengths is shown in Table 3-2. The theoretical peak wavelengths, λ_m, predicted by the model are very close to the measured λ_m with the slight exception at 30% power. The measured absolute irradiance at λ_m is very close to the theoretical spectral emittance at λ_m with the value at 50% power higher than predicted.

Table 3-2 Comparison in key data for the modeled output and the measured output

Emitter power (%)	Peak wavelength λ_m (nm)	Absolute irradiance at λ_m ($\mu Wcm^{-2}nm^{-1}$)	Theoretical peak wavelength λ_m (nm)	Theoretical spectral emittance at λ_m ($\mu Wcm^{-2}nm^{-1}$)
100	980	14251	923	13354
50	1156	6058	1192	3707
30	1156	1521	1442	1435

3.4 Print characterisation

3.4.1 White light interferometry

White light interferometry (WLI) is a non-contact system which uses white light to produce a detailed 3D profile. It works on the basis of an interferometer where two or more wave motions interact and combine resulting in an additive or subtractive wave which is determined by the recombining phase. This interference results in fringes of light that are either light or dark in colour dependant on the phase of recombining light, see Figure 3-9.

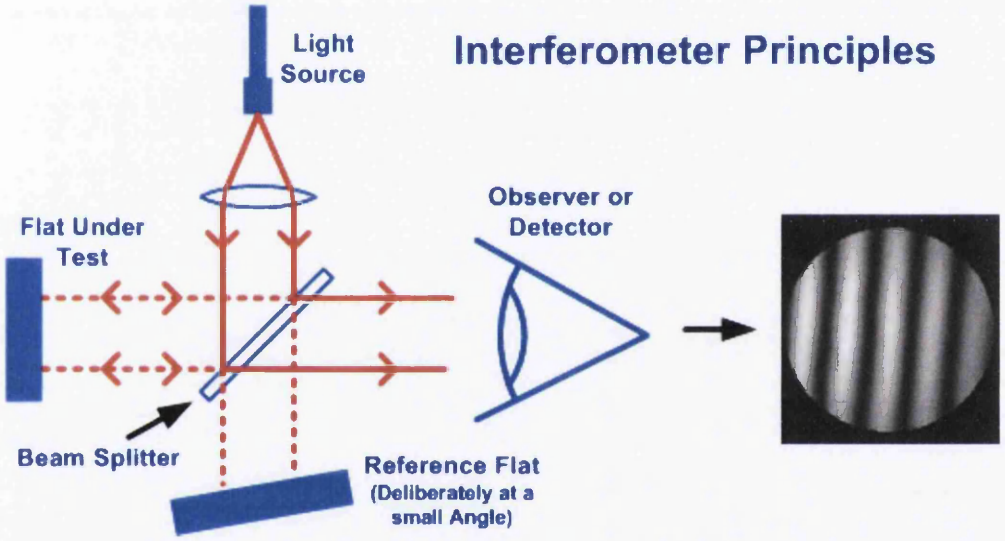

Figure 3-9 Principles of interferometry, taken from [15]

There are two main types of WLI available, phase shifting interferometry (PSI) and vertical scanning interferometry (VSI). Both use identical principles but in PSI the light is filtered and the system measures the phase of the interference fringes rather than the degree of fringe modulation or coherence as per VSI. PSI is the oldest technique and is well suited to the measurement of smooth continuous surfaces and is very precise but it has limited dynamic range of about 200nm and as such is unsuitable for most surfaces found in the printing industry. Consequently if the distance between adjacent measurement points is greater than 0.25x the wavelength of the light, height errors will be introduced of

multiples of 0.5 wavelengths. Conversely, with VSI the interferometric objective scans the surface vertically at varying heights, so the focus varies at each position. As the sample is scanned at varying heights the fringe contrast or modulation increases as the sample is brought into focus and decreases as it falls out of focus. The fringe modulation is recorded at each plane of focus from which the signals are processed to produce the subsequent surface parameters and profile, see Figure 3-10.

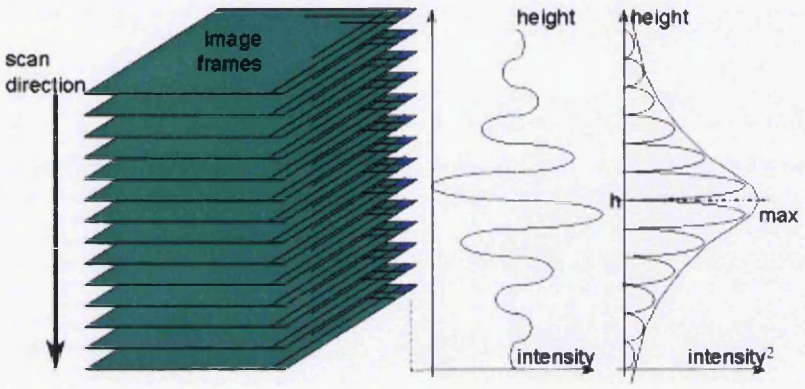

Figure 3-10 Fringe contrast and focus in VSI

Vertical scanning is a very flexible technique allowing large scan areas which are limited only by the lens magnification and depth limited by the movement of the objective verses the reference mirror. As such, scan lengths of 1mm and above are achievable.

The basic principle of interferometers is that light reflected from a reference mirror combines with the light reflected from the sample surface producing interference fringes from which a 3D topographic image of the surface can be constructed. The system has flaws in that it relies on a sufficient quantity of light being reflected from the sample surface to produce the interference fringes as without these there would be areas of missing data in the produced image.

3.4.2 Cross-sectional area, width and height analysis

To measure the 3D profiles of the printed lines a WYKO NT2000 fixed interferometer workstation, mounted onto an air-table to minimise vibration, was used. VSI was used because the scan lengths required were greater than the range of PSI. The maximum possible magnification was used to maximise the number of pixels. For 1.0mm lines 2.5x magnification was used and for 0.5mm to 0.1mm 5x magnification was used. Features wider than 1.0mm require multiple scans which are stitched together. A minimum of 5 scans were taken per line, measured at different points on the line. This was to ensure a good statistical sample was taken. A typical profile for a line measured using WLI is shown in Figure 3-11.

Once the WLI data was collected the cross-sectional area was determined by processing the individual data files through a bespoke software developed by Dr D. Deganello [16]. The software was designed for measuring the volume of gravure cells and has since been developed for measuring flexographic plates and printed lines. The data files are first converted to ASCII format before loading into the software. The data is inverted and the zero point, on the substrate, is set. Then the area of the line is selected and the data pasted into a spreadsheet. Data for the entire scan is presented giving height, width and area for each pixel of data.

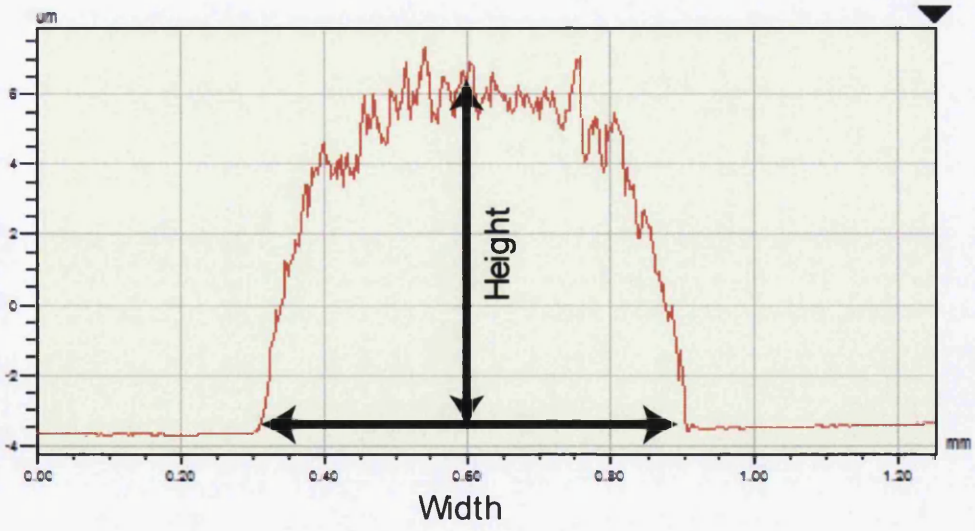

Figure 3-11 A typical line profile measured using WLI

To measure the film thickness of area part of the ink film is selectively removed to expose the substrate and this area is scanned with the WLI. A typical profile is shown in Figure 3-12.

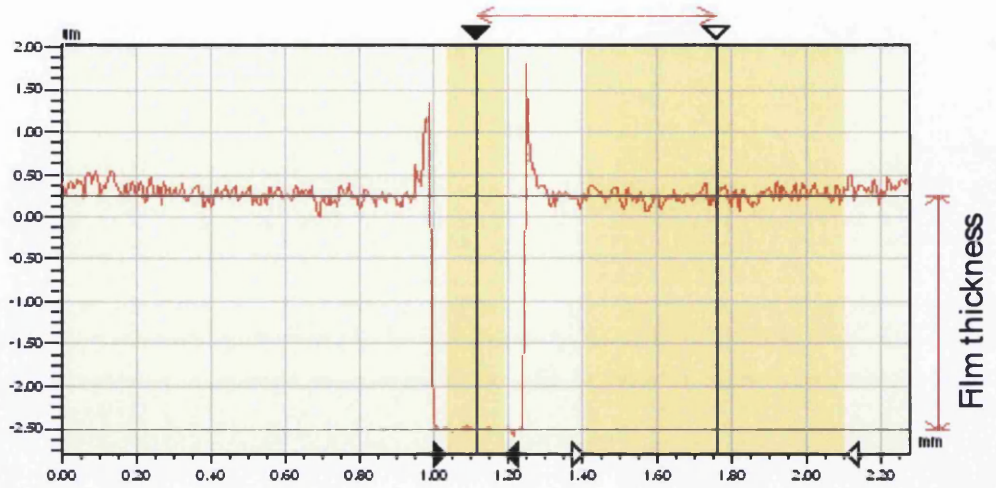

Figure 3-12 Measuring the film thickness of a coating using white-light interferometry

3.5 Electrical characterisation methods

Conducting samples were characterised by measuring their resistance using a four-point 'Kelvin' method to minimise the error in the measurement by eliminating the internal resistance of the leads.

3.5.1 Resistance

Resistance is defined through Ohms law which states that the current moving through a conductor between two points is directly proportional to its potential difference between the two ends. For a material with a linear resistance, where the line of potential difference (V), in volts, verses current (I), in amperes, on a graph passes through the origin, resistance (R), in ohms, is defined as the slope of the graph as shown in Equation 3-1:

$$R = \frac{V}{I}$$ *Equation 3-1*

Figure 3-13 shows the electrical diagram for a two point and four point resistance measurement. A conventional multimeter measures resistance using a two-wire ohms method. The multimeter inputs a stable current and the voltage drop is measured by the meter. The resistance measured therefore includes the sample resistance (R_s) and the resistance of the leads (R_{LEAD}). This method only works well if the resistance of the sample is much greater than that of the test leads and contact resistance otherwise the error in the measurement becomes too large. When the sample resistance is expected to be less than or equal to that of the test leads then a four-wire method is required. A four-wire method eliminates the issue of internal resistance by applying a stable current through two source wires and independently measuring the voltage of the sample through two sense wires.

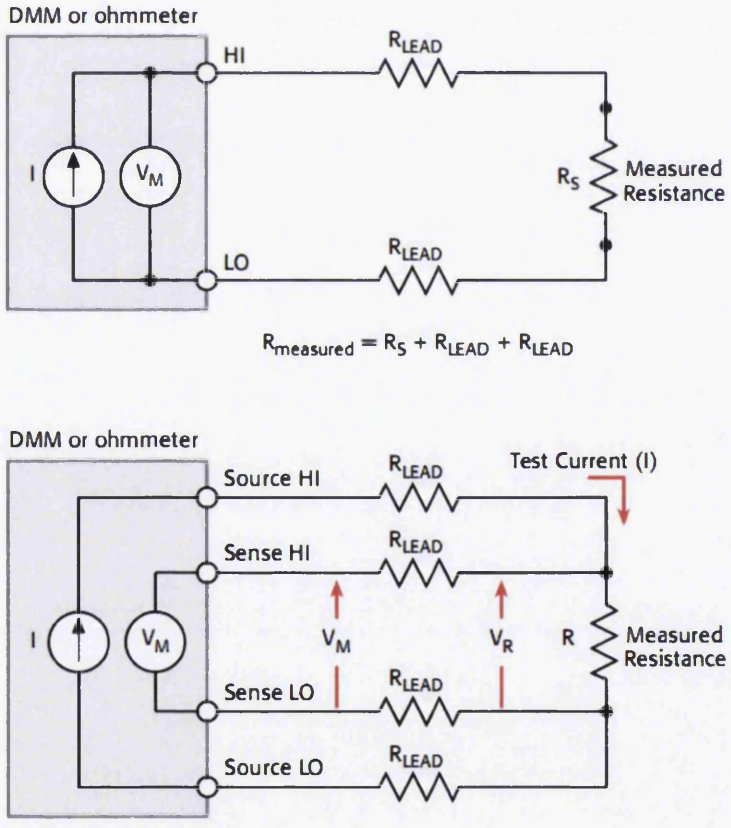

Figure 3-13 Two wire vs. four wire resistance measurements

3.5.1.1 Experimental setup for resistance measurements

Resistance was measured using a Keithley 2400 source meter connected to a Signatone S-116O probe station with 5μm titanium probe tips. The probes were spaced 5mm apart with a four-point probe setup used. Measurements were computer controlled allowing 100 measurements to be taken per sample point with a gap of 10ms per measurement. This allowed for very accurate measurements with a standard error of 4.52×10^{-5}. Five sets of resistance measurements were taken at different places either along the printed track or coated/printed area.

3.5.1.2 Volume resistivity

Resistivity is the measure of how a material resists the flow of electrical current. A low resistivity indicates that a material will readily conduct. There are two types of measured resistivity, weight resistivity, measured in units of ohm grams per metre squared (Ω.g m^{-2}), and volume resistivity, measured in units of ohm metres (Ω.m). During this thesis only volume resistivity is used.

Volume resistivity (ρ) is a measure of the resistance per unit volume and is calculated by Equation 3-2:

$$\rho = R \times \frac{A}{l} \qquad \textit{Equation 3-2}$$

Where A is the cross-sectional area of a track and l is the probe spacing.

To measure resistivity the resistance was measured as explained above and the cross-sectional area was measured using whitelight interferometry as outlined on page 3-15. Resistivity is frequently expressed as a ratio to bulk metal. To calculate the measured resistivity is divided by the bulk resistivity (N.B. The resistivity of silver is $1.59 \times 10^{-8}\Omega$.m).

3.5.1.3 Sheet resistance/resistivity

Sheet resistance is the measure of resistance of thin films that are nominally uniform in thickness. It is applicable to 2D systems where the thin film is considered as a 2D entity. Sheet resistance implies that the current flow is along the plane of the sheet, not perpendicular to it [17].

In a regular 3D conductor resistance can be written by rearranging Equation 3-2 to Equation 3-3:

$$R = \rho \frac{l}{A} = \rho \frac{l}{w.t} \qquad \textit{Equation 3-3}$$

Where w is width and t is thickness. If the resistivity is combined with the thickness then resistance can be written as in Equation 3-4:

$$R = \frac{\rho}{t} \frac{l}{w} = R_s \frac{l}{w} \qquad \textit{Equation 3-4}$$

Where R_s is the sheet resistance. For a square, $l = w$, so sheet resistance can be considered as Equation 3-5:

$$R_s = \frac{\rho}{t} \qquad \textit{Equation 3-5}$$

The units of sheet resistance are ohms per square (Ω/□). As $R_s \neq R$, a geometric correction factor (CF), which takes into account the sample size, shape and probe spacing, is required to convert measured 4-point resistance into sheet resistance, see Equation 3-6:

$$R_s = \frac{V}{I} \times CF \qquad \textit{Equation 3-6}$$

To measure sheet resistance the equipment setup was as described on page 3-16. Resistance was measured, as previously explained, and multiplied by a correction factor (see Equation 3-6) of 4.53 which is derived by Smits [17]. Before measuring the equipment was calibrated against a known standard from NPL.

3.6 Substrate and ink characterization methods

3.6.1 UV/VIS/NIR Spectroscopy

UV/VIS/NIR spectroscopy enables measurements of transmission and reflectance of materials across a wide bandwidth ranging from 200nm, in the UV, to 2500nm, in the NIR. This makes it an ideal method to characterize the substrates and inks which are to be exposed to NIR radiation.

Typically, UV/Visible absorptions relate to electronic transitions. The energy gap is that required to promote a valance electron to a higher energy orbital. Absorptions tend to be broad and described by the wavelength of maximum absorption. Mid infrared (IR) absorptions relate to vibrational transitions within molecules. Organic materials absorb strongly here and absorptions characteristically appear sharper than UV/Vis absorptions. NIR absorptions can be electronic or overtones of molecular vibrations. NIR transitions first appear similar to UV/Vis absorptions but get noisier and more like IR absorptions as the wavelength increases, usually after 2500nm. NIR penetrates deeper into many organics and can be used in applications where this deeper penetration is required.

A Perkin Elmer Lambda 750S high performance spectrophotometer [18] was used to measure the transmission and reflectance spectra of the polymer substrate and nanoparticle silver ink respectively. The Lambda 750 covers the whole of the NIR region of the spectrum up to 2500nm so the effect of the radiation from the HB-NIR emitters on both the substrate and the ink can be assessed. The instrument works in an identical way to that described in section 3.3.3.3.2: Light

from the source is passed through a monochromator to the sample and onto the detector.

3.7 Colorimetric measurements

3.7.1 Introduction

Colour is a phenomenon associated with the physical interaction of light energy with an object. Light is a form of electromagnetic radiation and visible light appears in the spectrum in the waveband between 380-700nm. When light in the visible waveband incidents with an object it reflects. The colour that is observed by the human eye is related to which wavelengths are absorbed by the object and which are reflected [19].

There are two type of reflectance; specular and diffuse. Specular reflectance is when the incident beam is reflected when the angle of incidence equals the angle of reflection and that the incident, normal and reflected directions are coplanar. Typical specular surfaces are mirrors or glossy in appearance. The reflecting material of a mirror was traditionally aluminium or silver. Diffuse reflectance is the reflection of light from a surface at many different angles with an ideal diffuse surface having equal luminance from all directions in the hemisphere surrounding the surface. Typical diffuse surfaces are matt in appearance.

Reflectance can be measured using spectrophotometry. As a means of quantifying colour, colorimetry was developed for use in the graphics industry as a means of quality testing prints by detecting discrete changes in printed colour. Reflectance spectra are converted into a series of Cartesian coordinate values which fit into a three dimensional colour space from which minute changes in colour can be tracked. The most complete colour space specified by the International Commission on Illumination (Commission Internationale d'Eclaireage, or CIE) is CIELAB and is illustrated in Figure 3-14 [19, 20].

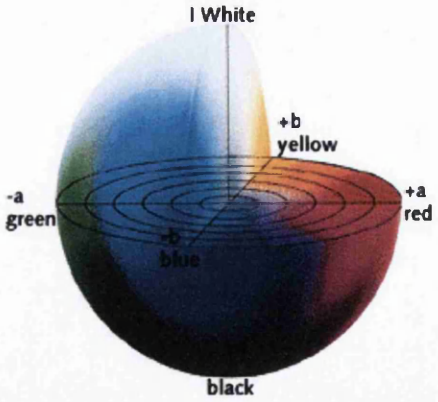

Figure 3-14 CIELAB colour space reproduced from [21]

CIELAB describes all the colours visible to the human eye and was created to serve as a device independent model for use as a reference. The three coordinates of CIELAB are a^*, which represents the position between red and green (a negative value indicates green and a positive value indicates red), b^*, which represents the position between yellow and blue (a negative value indicates blue and a positive value indicates yellow) and L^*, which represents the lightness of the colour ($L^* = 0$ yields black and $L^* = 100$ indicates diffuse white).

3.7.2 Colorimetric measurements

Reflectance colour measurements were performed using a spherical spectrophotometer, an X-Rite SP64 [22] (D_{65} illuminant/10° observer angle), against a calibrated white and dark background. A spherical spectrophotometer, see Figure 3-15, utilises an integrating sphere which the light source is reflected around to provide a diffuse light source. The reflected light is collected at 8° to the normal and is made up of both the specular and diffuse components. The specular component can be included or excluded from the data. If it is to be excluded a light trap is placed at -8° to block the directly reflected radiation. For the measurements in this thesis only the specular excluded (Diffuse) data was collected due to the reflective nature of the samples. Before samples were measured the spectrophotometer was calibrated using standard light and dark surfaces.

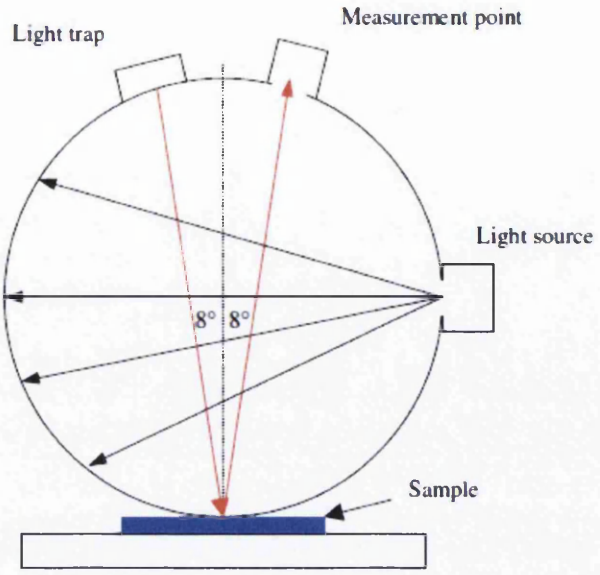

Figure 3-15 Schematic of a spherical reflectance spectrophotometer

3.8 Dye-sensitized solar cell building and characterization

3.8.1 Introduction

DSCs were introduced in chapter 1. This section will outline the procedure for manufacturing flexible DSCs with using titanium and ITO/PET substrates for the working electrode (WE) and counter electrode (CE) respectively. A schematic of the cell design is given in Figure 3-16.

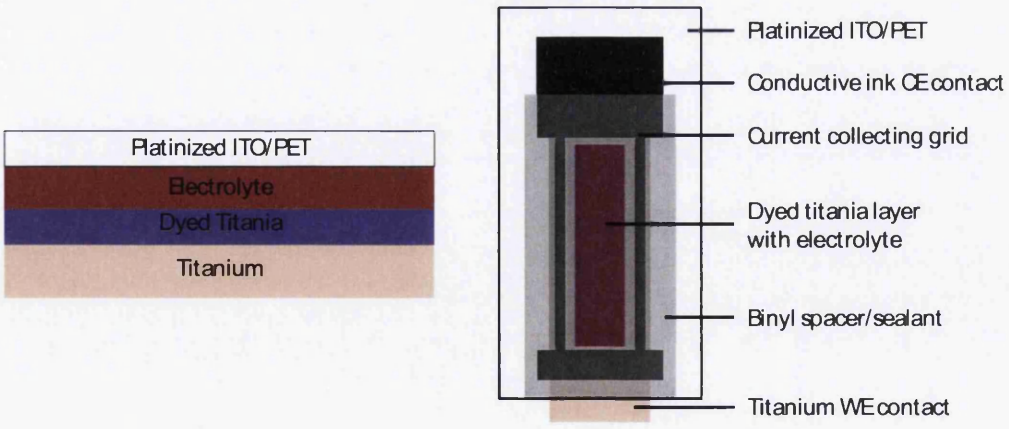

Figure 3-16 Schematic of the cell design

3.8.2 Working electrode fabrication

The substrate used for the WE was titanium foil (60μm thickness). Titanium was chosen because it has been shown to be a suitable substrate in the literature (C.F. Chapter 2). The titanium was firstly cleaned and degreased using an acetone bath in an ultrasonicator as suggested by Ito *et al* [23]. Then the metal surface was deoxidized by rubbing with a fine emery paper before being washed again in acetone. Prepared substrate was kept in acetone until used to minimize the risk of contamination.

The titanium dioxide paste used was a commercially available paste from Dyesol (DSL-18NRT). It is a transparent paste with an Ethyl Cellulose binder in a terpineol solvent. The paste was chosen because it is easy to print and commercially available. The paste was screen printed, as previously explained on page 3-5, using a 43T polyester mesh with a 45° thread angle, as specified by Dyesol. The image to be printed was a series of eight 10mm x 40mm strips (see Figure 3-17). The area of the WE was chosen to be 4cm^2 (1cm x 4cm) so that the effect of using current collectors could be better assessed. Standard WE areas in the published literature were found to be typically <0.25cm^2.

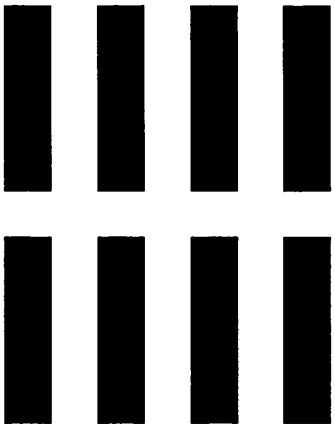

Figure 3-17 Screen image for DSC working electrodes

Post-printing the counter electrodes were dried through an IR/convection belt (SC Driers combination belt furnace) oven for 2 minutes (IR lamps at 100%

power) to dry off excess solvent before being placed in an air tight box. The WEs were then transported for sintering which was carried out in a high temperature furnace (Thermolyne – Thermo Scientific) at 500°C for 30 minutes. On removal from the furnace the working electrodes were allowed to cool to room temperature. A TiO_2 thickness of 22.5μm (±1.5μm) was achieved.

Sintered TiO_2 films were sensitized by fully immersing them in 0.3mM dye (N719 from Dyesol) solution, namely (cis-bis(isothiocyanato)bis(2,2'-bipyridyl-4,4'- dicarboxylato)-ruthenium(II) bis-tetrabutylammonium), in ethanol for 16 – 20 hours. N719 dye was chosen because it is the most commonly used high performance dye.

3.8.3 Counter electrode (CE) fabrication

CE substrate was indium tin oxide (ITO) coated polyethylene terephthalate (PET, LR-15 175μm thick, sheet resistance: 15Ω/□). ITO/PET was chosen because it has been shown by Philip [24] to be a viable substrate for DSCs and it is a relatively low cost flexible substrate. Three different CE were made:

- Controls with no current collectors
- Screen printed current collectors using a PTF microparticle silver ink
- Flexographic printed current collectors using a nanoparticle silver ink

Considering each type of CE in turn:

Control CEs were prepared by washing the ITO/PET with ethanol before being dried and chemically platinized (see below).

Screen printed current collectors were prepared by firstly washing the ITO/PET substrate in ethanol to remove contaminants. A PTF microparticle silver ink from Dyesol (DYA-100) was then screen printed (using a DEK 248 press) using a stainless steel screen (77 threads per cm with a 45° mesh). Printed samples were dried in an oven (Heraeus vacutherm) at 150°C for 2, 5 or 10mins.

Flexographic printed current collectors were printed using an IGT F1 printability tester (on page 3-3) using a nanoparticle silver ink formulated for flexographic printing (InkTec TEC-PR-030). Samples were dried and sintered in an oven (Heraeus vacutherm) at 130°C for 10minutes. The drying and sintering time was found through scoping trials to give the best conductivity.

The current collector design (see Figure 3-18) consisted of a large area (20 mm x 25 mm) terminal with two current collecting tracks (42 mm x 2mm) connected by a busbar (6 mm x 25 mm). The design was chosen to compliment test cells produced by TATA Steel Colors although there were size limitations due to the 50mm maximum substrate width of the flexographic printer which meant that the overall width of the design was limited to 25mm.

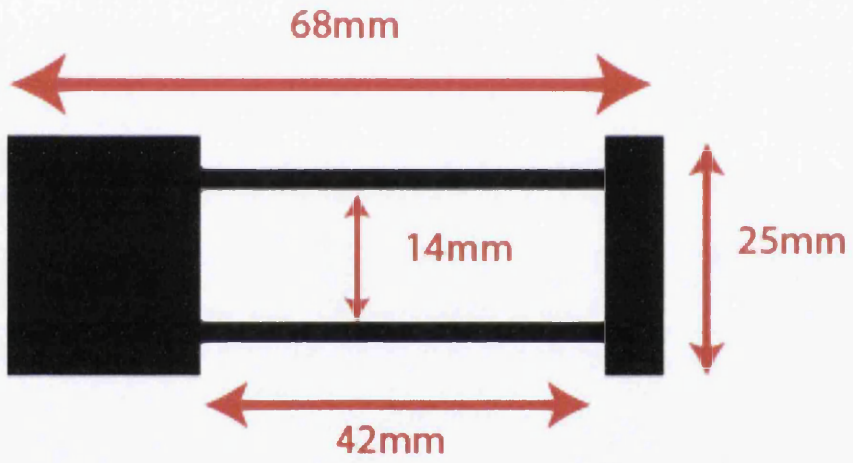

Figure 3-18 Current collector design with 2mm wide tracks

The CEs were chemically platinized according to the method developed by the Jun [25]. The platinizing agent (5mM hexachloroplatinic acid dissolved in isopropyl alcohol (IPA)) was dribbled over the substrate and a sponge roller was twice rolled over the CE to homogenize the solution. They were then dried with warm air, to remove the IPA, and placed into an oven at 60°C for 6 minutes. Once removed a reducing agent (0.27g Sodium borohydride in a 100mL solution, 60/40 of ethanol/water) was swirled over the CEs for approximately 30 seconds or until a distinct colour change has been observed. The CEs were then

alternately washed with water and IPA and repeated before the CEs were air dried and put in an oven at 60°C for 6 minutes.

3.8.3.1 Electrolyte and sealant materials

Sealant and spacing material used was a thermoplastic Binyl© film (25μm thick). The Binyl was laser cut to size prior to use and was applied to both the WE and CE and tacked on at 120°C. Usually only the WE has a layer of sealant applied and then the CE is sealed on top. In this case both electrodes were surrounded with a layer of Binyl to ensure the silver tracks were insulated from the electrolyte to prevent corrosion. The two electrodes were sealed together using a heat press at 120°C for 20 seconds. At the bottom end an unsealed gap was left for electrolyte filling by sandwiching a piece of PTFE coated plastic in between the electrodes. Once electrolyte filling was completed the cell would be completely sealed. Originally it was planned to use the more commonly used thermoplastic Surlyn© (50μm thick) and tack it onto the CE. However, joining the electrodes together was difficult as the Surlyn© did not adhere well to the titanium metal of the WE.

The electrolyte (0.5M lithium iodide, 0.05M iodine and 0.5M *tert*-butyl pyridine in 3-methoxypropionitrile) was taken from reported literature [26]. A vacuum injection method was used to fill the cells whereby the cells were placed bottom end down (where a gap in the sealant was left) in a shallow bath of electrolyte which was itself placed in a desiccators and put under vacuum. As the vacuum was subsequently released it allowed the electrolyte to fill slowly. Once filling was completed the unsealed end was then sealed using a heat press.

A schematic of the DSC manufacturing process is shown in Figure 3-19.

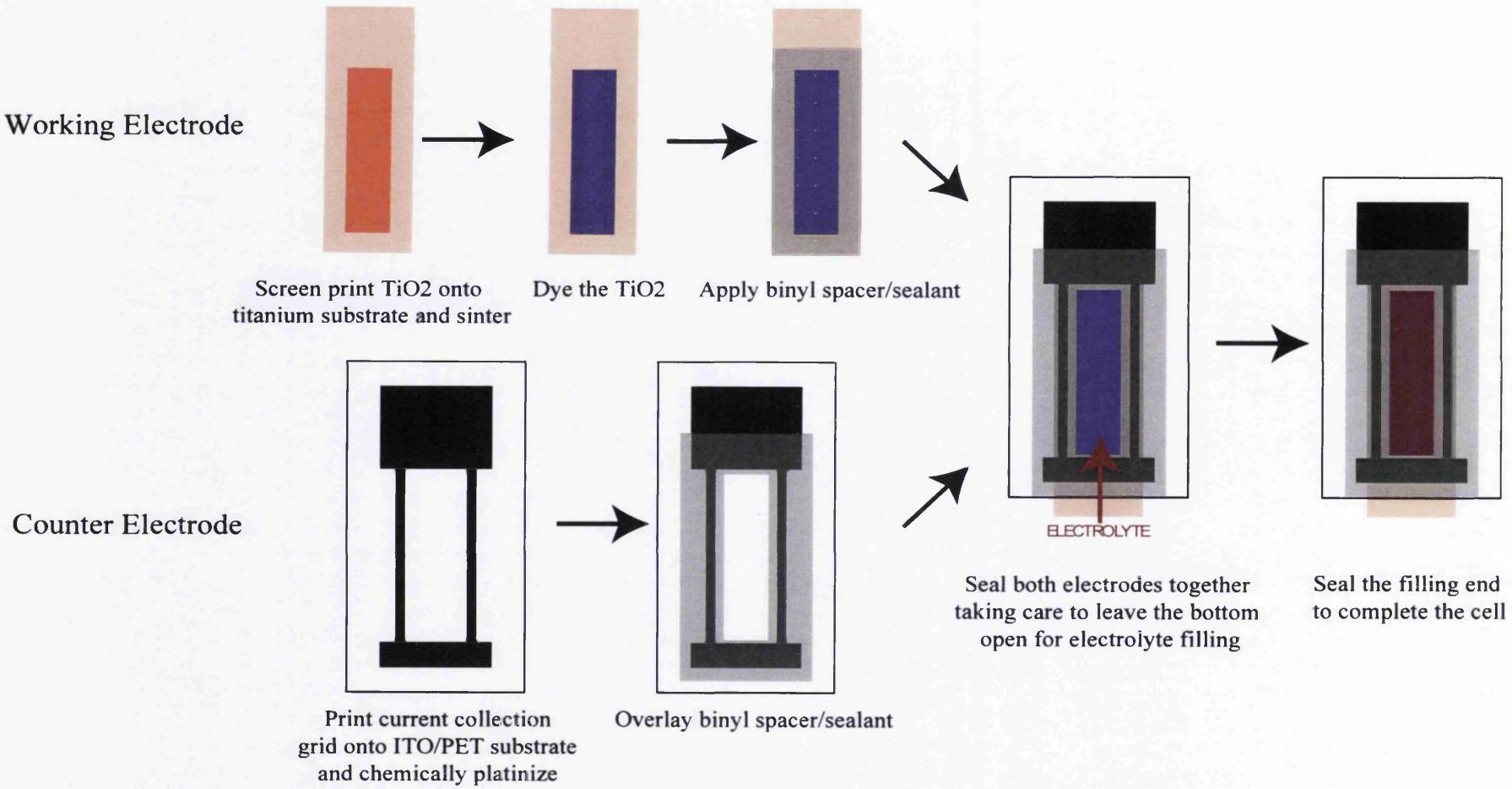

Figure 3-19 Schematic of flexible DSC device manufacturing

3.8.4 Measurement of cell performance

3.8.4.1 Background

The equivalent circuit model of a photovoltaic cell is shown in Figure 3-20. I_L represents a photon current source, r_s series resistance, r_{sh} a shunt resistance and the element between I_L and r_{sh} is a diode. The element r_{sh} represents the loss due to diode leakage currents, while r_s represents the ohmic losses in the front surface of the cell.

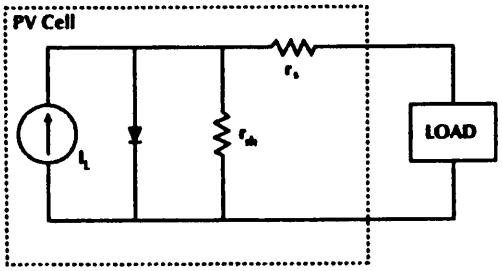

Figure 3-20 Equivalent circuit model of a photovoltaic cell

Figure 3-21 shows a typical current voltage (I-V) curve of a solar cell. The curve passes through three significant points:

- Short circuit current (Isc), which occurs at the point on the curve where the voltage is zero. At this point the power output of the cell is also zero.
- Open circuit voltage (Voc), which occurs at the point on the curve where the current is zero. The power output of the cell at this point is also zero.
- Maximum power (Pm) is the point on the curve where the current (Im) and voltage (Vm) are at their maximum.

The I-V curve is based on the cell being under standard conditions of sunlight and cell temperature, as described by the AM 1.5 standard for solar irradiation, and assumes there is no shading of the cell. Standard sunlight conditions on a clear day are assumed to be 1000 Watts of solar energy per square meter ($1000Wm^{-2}$). This condition is referred to in the literature as 'one sun' or AM1.5.

From I-V measurements the key performance parameters of a cell, such as energy conversion efficiency (η) and fill factor (FF), can be determined.

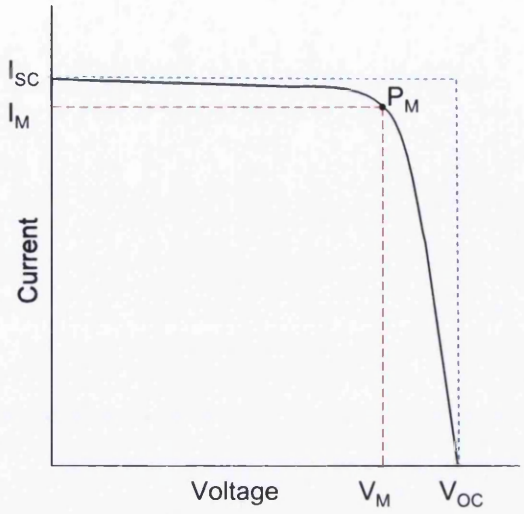

Figure 3-21 A typical current voltage curve for a solar cell

Overall energy conversion efficiency (η) is calculated from Equation 3-7:

$$\eta = \frac{P_m}{P_{in}} \qquad \textit{Equation 3-7}$$

Where Pin is the power input to the cell.

The fill factor (FF) determines the shape of the solar cell I-V characteristic and is a useful parameter for determining how well a cell is working. A perfect cell has a FF of 1. FF is calculated from Equation 3-8:

$$FF = \frac{I_m V_m}{I_{sc} V_{oc}} \qquad \textit{Equation 3-8}$$

3.8.4.2 Current voltage (I-V) measurements

The I-V characteristics of the DSCs were measured using an Oriel Sol3A (94023A) utilising a Xenon arc lamp (150 W), an AM1.5 filter and a Keithley

2400 source meter. A certified (Oriel 91150V) monocrystalline silicon reference cell calibrated by the National Renewable Energy Laboratory (NREL) was used to adjust the solar simulator to the standard light intensity of one sun ($1000W/m^2$). All cells were illuminated from the counter electrode side, i.e. before reaching the semiconductor layer the light had first to pass through the counter electrode substrate, platinized layer and electrolyte. Measurements were made within hours of constructing the cells. The repeatability of the cells is discussed in Chapter 5.

3.9 Closure

This chapter has outlined the experimental techniques and equipment available for the investigation of different printing and coating technologies for depositing conductive inks and methods for drying and characterising them. A Method for building and characterising flexible DSCs has also been described. The next section of work will investigate the printing technologies mentioned in this chapter.

3.10 References

1. *Standard Practice for Applying Coil Coatings Using The Wire-Wound Drawdown Bar*, in *ASTM D4147 - 99(2007)e1*. 2007, ASTM.
2. http://www.rkprint.co.uk/?page_id=14 26th September 2012
3. Watson, T., I. Mabbett, H. Wang, L. Peter, and D. Worsley, *Ultrafast near infrared sintering of TiO2 layers on metal substrates for dye-sensitized solar cells.* Progress in Photovoltaics. **19**(4): p. 482-486.
4. http://www.igt.nl/gb/awm/bestanden/products/f1-uk.pdf Accessed: 26th September 2012
5. Hamblyn, S.M., *The role of the plate in the ink transfer process in flexographic printing*. 2004.
6. Cherry, J.A., *Ink release characteristics of anilox rolls*. 2007.
7. Beynon, D.G., *Plate to substrate ink transfer in the flexographic printing process*. 2007.
8. Cherry, J.A., *Ink release characteristics of anilox rolls*. 2007, Swansea University.
9. *DEK 248 Operators Manual.*
10. Heraeus, *Operating Instructions: Vacutherm Drying Oven VT6025*. 04.2003 ed.

11. Mabbett, I., *Applications of near infrared heating to the coil coating industry.*
12. Knischka, R., U. Lehmann, U. Stadler, M. Mamak, and J. Benkhoff, *Novel approaches in NIR curing technology.* Progress in Organic Coatings, 2009. **64**(2-3): p. 171-174.
13. Atkins, P.W. and J. De Paula, *Atkins' Physical Chemistry*. 2002: Oxford University Press.
14. Ocean Optics, *HR2000+ High-speed Fiber Optic Spectrometer*
15. http://www.oldham-optical.co.uk/Interferometer.htm Accessed: 21/08/12
16. Personal communication with Deganello, D.
17. Smits, F.M., *Measurement of Sheet Resistivities with the Four-Point Probe.* The Bell System Technical Journal, 1958: p. 711-718.
18. *Lambda 750 UV/VIS/NIR spectrophotometer operators manual*: Perkin Elmer.
19. Hunt, R.W.G., *Measuring Colour*. 1998: Fountain.
20. Hunt, R.W.G., *The Reproduction of Colour*. 2005: Wiley.
21. http://www.sapdesignguild.org/goodies/glossary_color/index1.html Accessed: 3/03/2012
22. X-Rite, *SP60 Series Sphere Spectrophotometer: Operator's Manual (Models: SP60, SP62 and SP64).*
23. Ito, S., N.-L.C. Ha, G. Rothenberger, P. Liska, P. Comte, S.M. Zakeeruddin, P. Pechy, M.K. Nazeeruddin, and M. Graetzel, *High-efficiency (7.2%) flexible dye-sensitized solar cells with Ti-metal substrate for nanocrystalline-TiO2 photoanode.* Chemical Communications, 2006(38): p. 4004-4006.
24. Philip, B., *Investigation of metal substrates for photovoltaic applications*. 2010, Swansea University.
25. Jun, Y., J. Kim, and M.G. Kang, *A study of stainless steel-based dye-sensitized solar cells and modules.* Solar Energy Materials and Solar Cells, 2007. **91**(9): p. 779-784.
26. Lindstrom, H., A. Holmberg, E. Magnusson, L. Malmqvist, and A. Hagfeldt, *A new method to make dye-sensitized nanocrystalline solar cells at room temperature.* Journal of Photochemistry and Photobiology a-Chemistry, 2001. **145**(1-2): p. 107-112.

4 Comparison of printing technologies for the deposition of conductive tracks

4.1 Introduction

Traditional printing technologies are increasingly being considered for the manufacture of printed electronic devices. By using printing to manufacture companies can potentially achieve high volume, high speed production with a target to deliver a low cost end product. Printing technologies and their application to printed electronics have been previously discussed in Chapter 1.

A printed conductive track has to fulfil several key requirements. To maximise conductivity the printed track must be homogenous, with no defects, and the conducting particles in the printed ink film must be in contact with one another and closely packed together. Void spaces between conductive particles will increase electrical resistance and inhibit the conductivity.

Tata Steel chose to develop their first generation DSC product using screen printing. Screen printing is a thick-film deposition method and can be used to print most of the required layers in a DSC (Cf. Chapter 1). R2R manufacturing by screen printing is possible but it is not a rapid, high volume, technology compared with other printing technologies, such as flexography. This alternative printing technology can print thin-films and could provide an alternative method for printing the current collectors in DSCs with potential savings in materials costs.

This chapter aims to compare flexographic printing with screen printing for their suitability to printing conductive tracks with a potential application as current collecting grids in DSCs. Factors to be evaluated are; morphology, spreading (gain), deposit thickness (average height and maximum height) and cross-sectional area through a combination of experimental and literature data.

4.2 Screen printing

4.2.1 Introduction

Flatbed screen printing has been used for printing electronic circuits since the 1970s [1-3]. Screen printed current collecting grids have been used for silicon solar cells [3, 4]. For DSCs, screen printing has become the deposition process of choice for printing the functional layers [5] including; the titania working electrode and current collectors. The screen printing process has been discussed in Chapter 1.

4.2.2 Factors affecting print quality in screen printing

There are a multitude of factors, which were introduced in Chapter 1, which will affect how a feature will screen print including the; mesh, emulsion, squeegee, snap, print speed and ultimately the ink itself.

The thread count of the mesh determines the open area to be filled with ink; the smaller the thread count, the greater the open area. The open area determines the volume of ink which can be contained in the stencil; the larger the open area is the greater the volume of ink. The volume of ink pushed through the stencil will affect the thickness of the print. Figure 4-1 shows how the thread count impacts the open area, for both polyester and stainless steel meshes. Generally, as the thread count increases the open area decreases, with stainless steel meshes resulting in a larger open area. How the open area affects the theoretical ink volume is shown in Figure 4-2; the greater the open area, the greater the theoretical volume of ink which can be printed is.

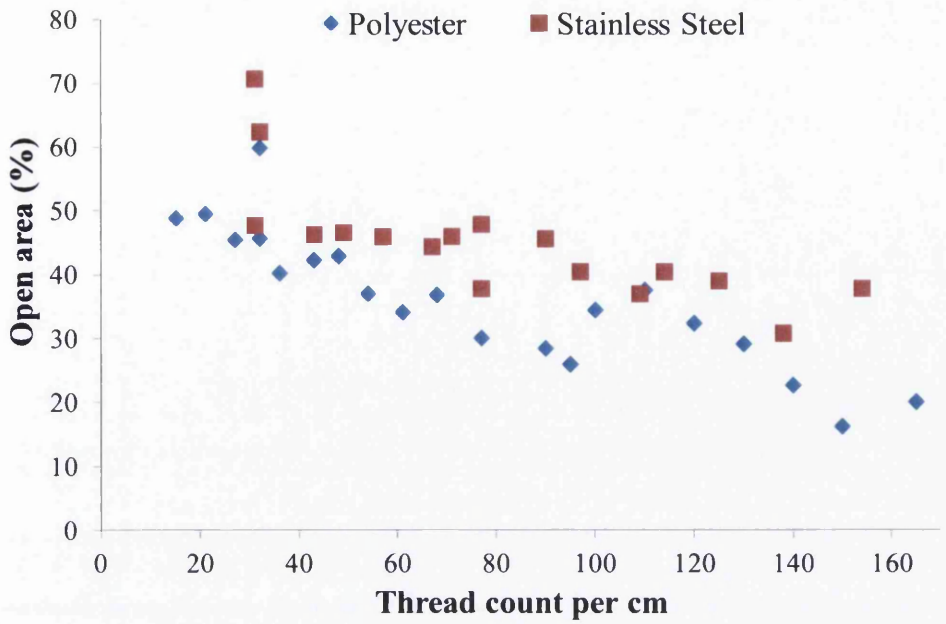

Figure 4-1 How thread count affects the open area in a screen printing mesh (Data from DEK)

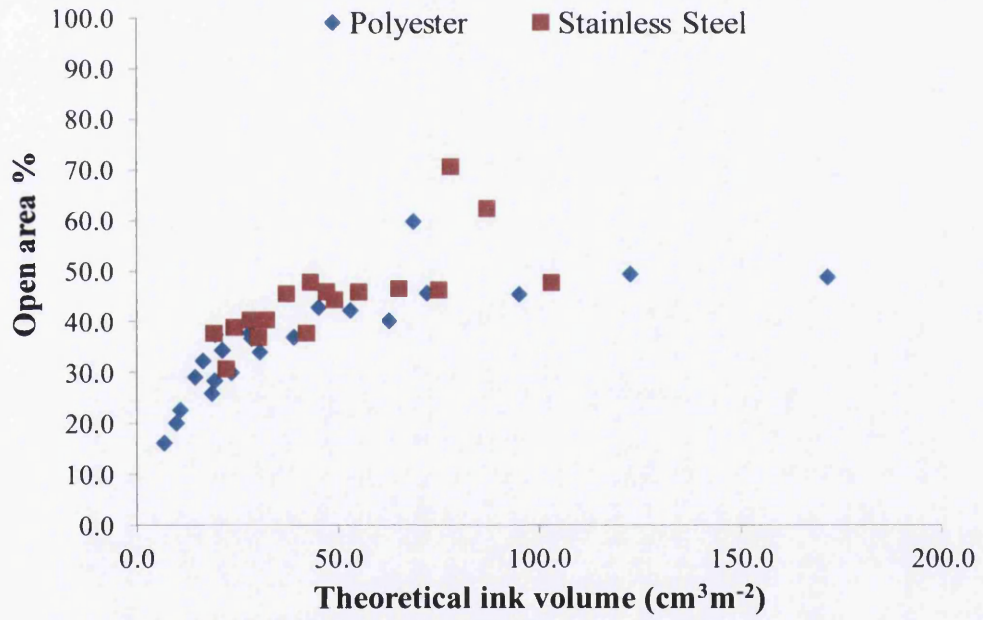

Figure 4-2 How ink volume changes with mesh open area for polyester and stainless steel screens (Data from DEK)

The emulsion coating on the mesh can be used to increase the wet film deposit by increasing the thickness of the stencil; a thicker stencil means more ink can be pushed through. However, a thicker stencil does not necessarily mean that the profile will be rounded as the ink that is not held in the mesh is not supported in the centre, only on the edges, and so for wide features the centre of the print appears 'slumped'.

Figure 4-3 shows how the specified mesh can affect the size of the features to be printed. The images are of a 77 threads per cm (77T) and 43 threads per cm (43T) screen with a mesh angle of 22.5° and shows a 0.3mm and 1.0mm wide line in the stencil. The difference in thread size and visual open area is clear and the 43T screen would pass a higher volume of ink through than the 77T.

a)

b)

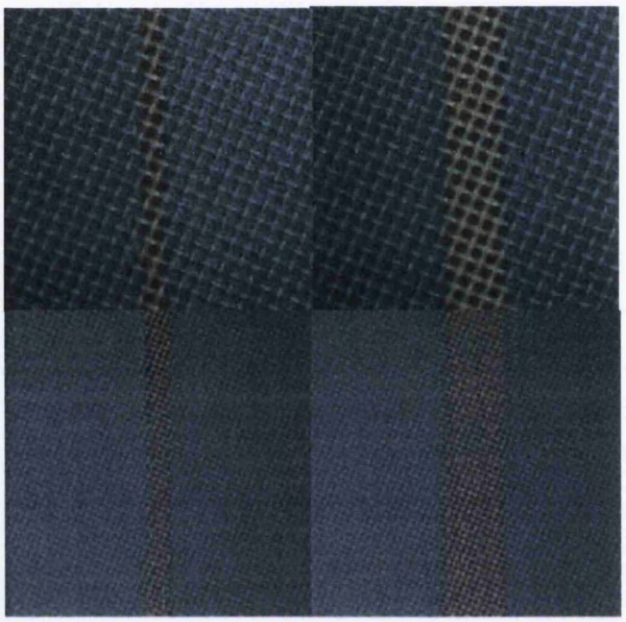

Figure 4-3 Microscope image of 0.4mm and 1.0mm line features on: a) a 43T coarse mesh and b) a 77T fine mesh at 10x magnification

The squeegee has a large effect on the print [6, 7]. Changing the angle of the squeegee can change the solid density and film thickness; increasing the angle from the horizontal will reduce the ink deposit. The shape can affect the print as a high aspect ratio (tall and thin) is affected by pressure and can bend which leads to ink manipulation and an increase in film thickness compared to a

squeegee with a small aspect ratio which is more rigid and is not affected by pressure. Material type is important to consider for the squeegee as a hard squeegee will tend to print a thinner feature over a softer material squeegee.

Snap-off gap has a big effect on the quality of the print [8]; a large snap gap can cause visible mesh images in the print, a small snap can result in the substrate sticking to the screen.

4.2.3 Screen printing trial

The trial was a simple experiment to gain some basic practical understanding of the screen printing process and to observe how a conductive ink behaves when different width lines are screen printed.

4.2.3.1 Experimental procedure

The press used in this trial was a DEK 248 semi-automatic flatbed screen printer. Printed tracks (Widths: 2.0mm, 1.0mm, 0.6mm, 0.3mm) were printed using a 77T stainless steel screen with a base emulsion and a mesh orientation of 45° (See Table 4-1). Substrate was a PET foil from Dupont Teijin films (Melinex ST504 175μm). The ink was a PTF microparticle silver ink from Dyesol (DYA100). After printing the ink was dried in an oven at 150°C according to the manufacturers' specification. Line profiles were analysed using whitelight interferometry and the electrical resistance of the lines were measured using a four-point probe method.

Table 4-1 Screen specification for trial

Thread count (per cm)	Thread count (per inch)	Mesh width (μm)	Thread diameter (μm)	Thread spacing (μm)	Open area (%)	Theoretical ink volume (cm^3m^{-2})
77	200	90	40	130	48	43

4.2.3.2 Printed lines analysis

Figure 4-4 shows the line profiles for screen printed lines printed in the print direction. Profiles are rounded and are uniform in shape regardless of the width. The topography of the lines, in Figure 4-5, and the edges of the lines appear smooth and without breaks. Continuity of the line is important for conductivity as defects will impact on the performance. The lines have large cross sections, as shown in Figure 4-6, which increase linearly with width which will be beneficial for achieving a low volume resistivity and therefore a good electrical performance.

Spreading, or gain from the nominal width, is an important issue to take into consideration for DSCs. In a module, where there are several DSC cells linked together, current collectors are printed in between the cells and they need to be kept insulated to protect them from the corrosive electrolyte solution. Insulating requires an overprinting process and so spreading could potentially affect over-printing registration. Figure 4-7 shows that all the printed tracks were wider than specified. The 0.3mm line shows the smallest gain (1.4%) and the 0.6mm line exhibits the largest (11%). Spreading is expected as the ink is still fluid after it has printed and before it has dried.

Thickness is linked to the mesh thread count and stencil emulsion thickness [8]; a high thread count gives a low thickness, a thick emulsion will increase thickness but will affect the profile of the line. Figure 4-8 shows the average and maximum heights of the lines printed in the test; the wider the line, the greater the height. Average heights are consistent for line widths of 2.0mm and 1.0mm line resulting in a thickness of ~9μm. Below 1.0mm the average height drops. The reason for the decrease in height is because the volume of ink transferred is less.

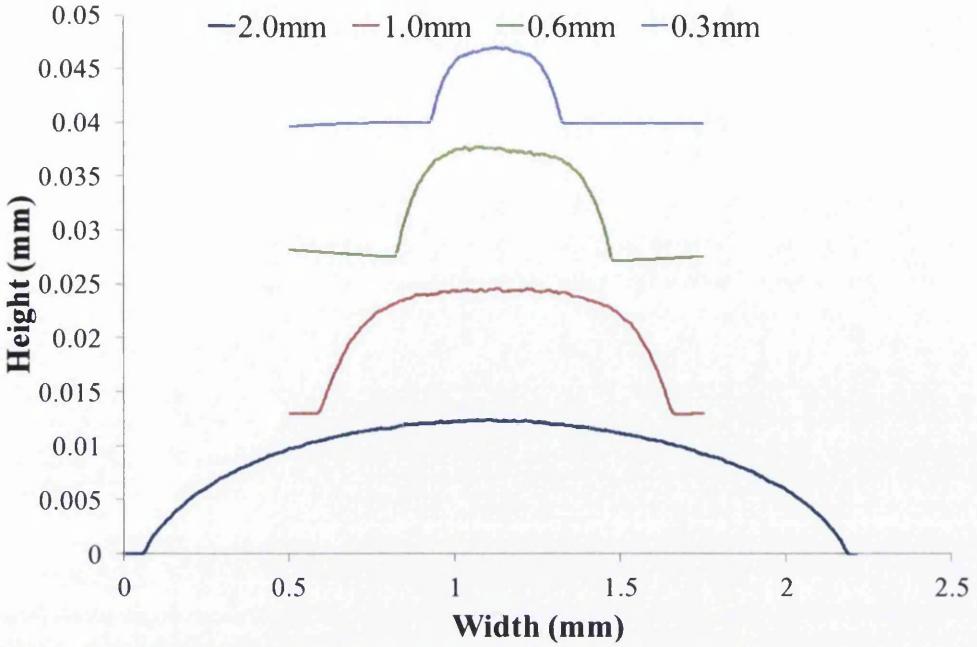

Figure 4-4 Screen printed cross-section profiles in the print direction

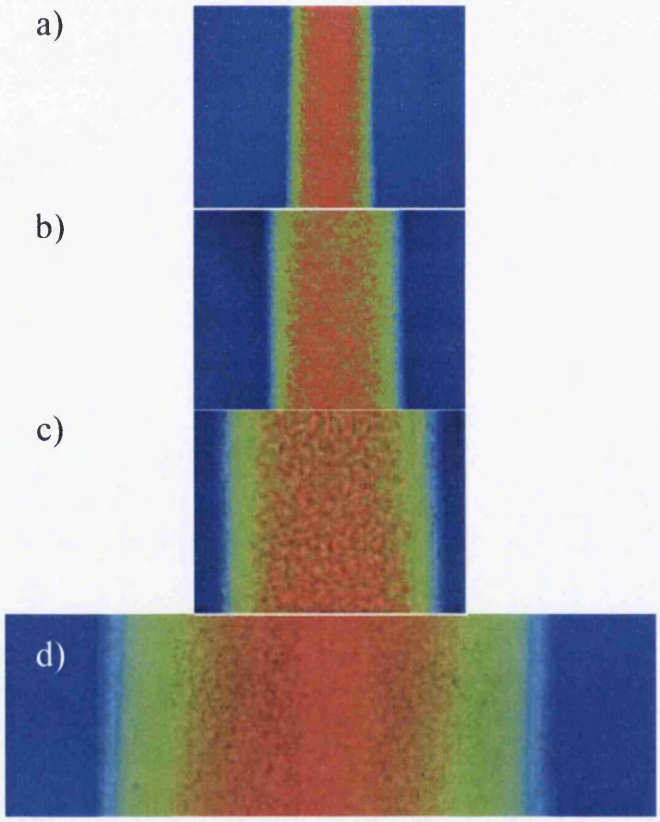

Figure 4-5 Whitelight interferometer line topography images for: a) 0.3mm, b) 0.6mm, c) 1.0mm, d) 2.0mm screen printed lines

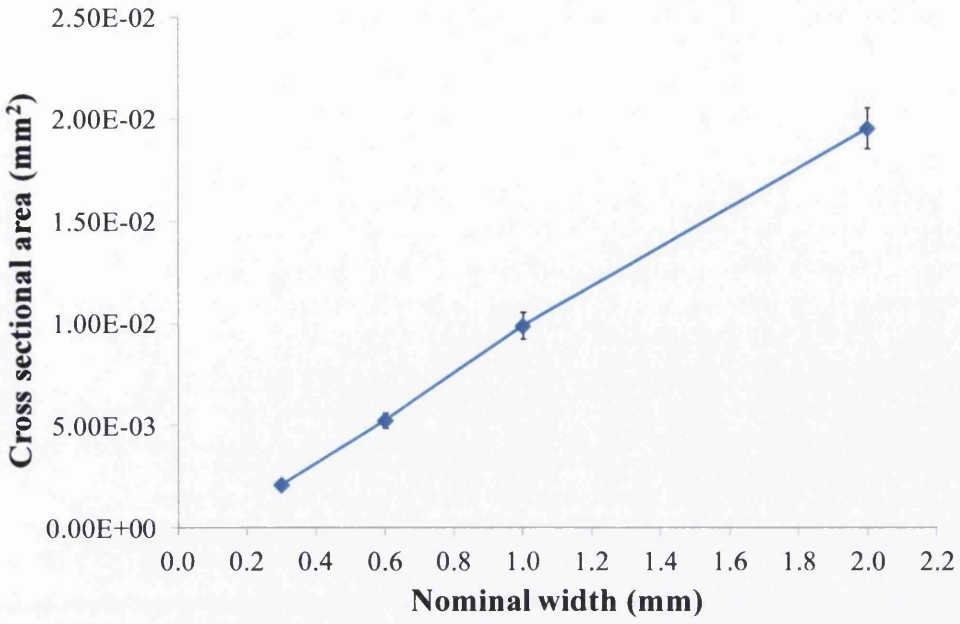

Figure 4-6 Cross sectional area verses line width for screen printed lines

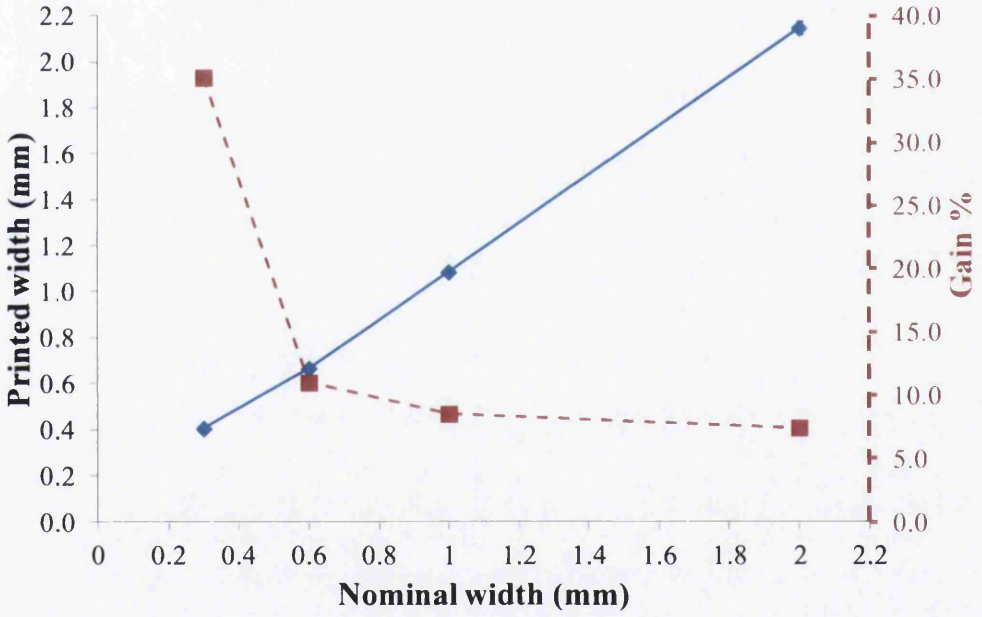

Figure 4-7 Line gain from the nominal width for screen printed lines

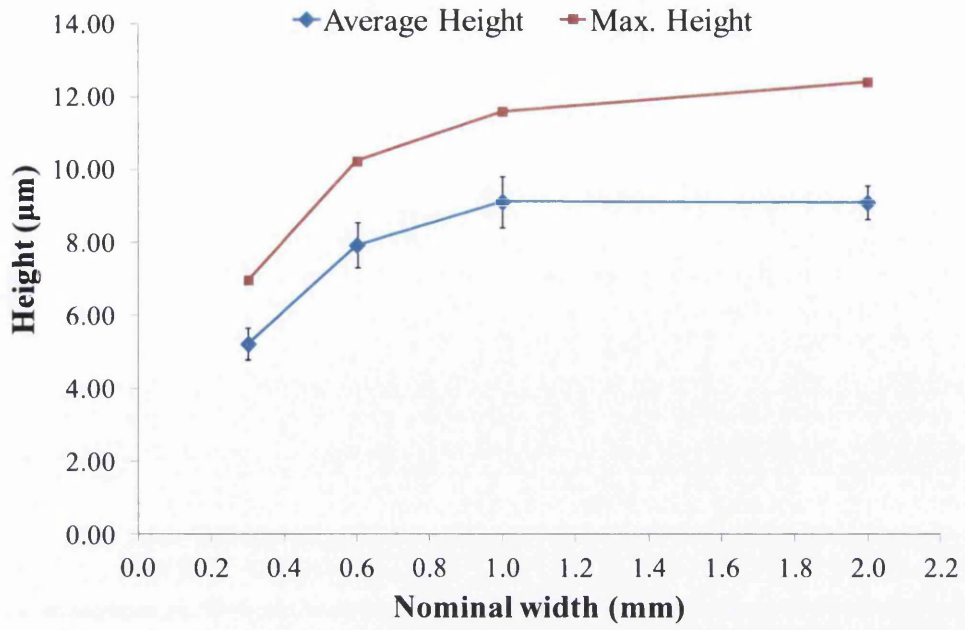

Figure 4-8 Comparison of average and maximum heights for screen printed lines

4.2.4 Summary

Screen printing is a process well suited for printing conductive features. It can deposit thick films facilitating large conducting areas and lines which are homogenous, which will facilitate a low electrical resistance, and give rounded uniform profiles, which are beneficial for overprinted layers as there is minimal sharp discontinuity.

The printed ink film is determined by the screen mesh. The coarser the mesh is the greater the theoretical ink volume. A coarse mesh increases the mesh opening and the larger this open area is the greater the volume of ink that can pass through.

Printed lines do vary from the design specification although this does depend on the mesh. The stencil holds the printing image and if the mesh is varied then the line morphology will change depending on the mesh opening.

Resolution is affected by the mesh; a coarse mesh with a large mesh opening will print large features but fine features will only print if the opening is smaller than the line width and lines will appear wavy. A fine mesh will improve resolution but film thickness will be compromised.

Line height is affected by the mesh opening. A large mesh opening allows more ink to pass through. If the image on the stencil is close in dimension to the thread diameter then the mesh can act as a block restricting the amount of ink transferred. An emulsion can be added to the screen to add height to the mesh. Whilst this increases the volume of ink in the stencil the amount of ink transferred to the substrate is only affected at the edges of the image as there is no extra mesh structure in the middle to support the extra volume of ink.

Screen printing is capable of printing a large range of ink volumes and so the range of print heights is large. The range of inks in terms of particle loading and rheology is also large. As a result screen printing is well suited for the printed electronics industry. The main limiting factor is the poor resolution, as features below 100μm are unlikely to print, as the thread diameter limits how fine the mesh can be woven, hindering the process ability for printing thin-films. With the film thickness, resolution and image master determined by the screen one cannot be changed without affecting the others.

4.3 Flexographic printing

Flexography has been reported as a method to deposit printing electronic features for conducting grids for OLEDs [9, 10] and low cost circuitry for silicon PV [11].

The flexographic printing process was introduced in Chapter 1. In summary; a specified volume of ink is transferred from an engraved anilox roll, whose cell geometry controls the volume of ink, onto a flexible polymer plate, which holds the image in relief to be printed, and the plate then transfers the ink to the substrate.

Flexography differs from screen printing and rotogravure in that the image carrier (the plate) does not act as a primary ink metering device which is the anilox roll. The advantage of this is that the same image carrier can be used so the nominal image resolution remains the same but the film thickness can be adjusted by using a different specification of anilox roll.

This trial was designed to assess the flexographic process for printing a series of lines using a nanoparticle silver ink. Two anilox rolls with different volumes were used to compare the effect of changing the amount of ink printed.

4.3.1 Factors affecting print quality in flexography

Two key factors which can affect the print quality for printing conductive features using flexography are the anilox roll and the plate.

The anilox roll controls the amount of ink ultimately printed with film thickness controlled by the anilox cell volume; a large anilox cell volume gives a greater film thickness. This has been shown by Deganello *et al* [10] for printed silver grids where the heights and cross-sectional areas of their tracks increased with increasing anilox volume. Increasing the anilox cell volume also increased ink spreading.

The plate is an important parameter to consider as the photopolymer will have its own surface energy which will affect the way the ink is transferred onto the substrate. Modifying the surface of a plate can improve feature resolution as demonstrated by Kwak *et al* who achieved conductive features with widths of ~20μm [12].

The plate deforms on engagement, due to the printing pressure, which causes ink spreading [13]. The modulus of the plate material will affect the print; a plate material with a high modulus will deform less under pressure and would lead to greater ink spreading than a plate material with a lower modulus. The effect of

the modulus can be compensated by changing the type of mounting tape used to adhere the plate to the plate cylinder; a plate with a high modulus and high elasticity could be mounted by a tape with a low modulus and vice-versa [14]. Spreading is inherent of the flexographic process [15] as ink is transferred from the polymer plate to the substrate at the printing nip (the point of contact where the substrate passes between the plate and the impression cylinder). Ink is forced out from the centre of the image relief causing spreading to occur. Spreading is affected by the plate-to-substrate engagement pressure; the greater the pressure the greater the spreading. Consequently the printed line will always be wider than the specified nominal value. Deganello *et al* found that their printed tracks gained from their nominal values by as much as 370% for a 20μm nominal width [9].

4.3.2 Flexographic printing trial

The trial was designed to assess flexographic printed conductive tracks for its potential use for current collectors in DSCs. The ability of flexography to be able to change the volume ink deposit without changing the image master gave the opportunity to produce samples with two different anilox rolls to offer a comparison.

4.3.2.1 Experimental procedure

Samples were printed using an IGT F1 flexographic printability tester, as described in chapter 3 at a speed of 0.4m/s and a printing force of 75N and anilox to plate force of 75N. The photopolymer plate was produced with a 0.64mm relief. The image was tracks which were 40mm in length and ranging in width from; 0.1mm, 0.2mm, 0.3mm, 0.5mm, 1.0mm and 2.0mm. Prints were produced using two different volume anilox rolls; $8cm^3m^{-2}$ and $24cm^3m^{-2}$ which are defined in Table 4-2. The ink used was a nanoparticle silver (InkTec, TEC-PR-030), formulated for flexographic printing, which was dried and sintered in an oven, according to manufacturers specification at 130°C for 10 minutes.

Table 4-2 Anilox roll specifications

Reference	Anilox volume (cm^3m^{-2})	Line ruling (l/cm)	IGT Part number
AR8	8	140	402.409
AR24	24	80	402.416

4.3.3 Print analysis

Figure 4-9 shows the profiles of the printed tracks printed using the anilox roll AR8. Figure 4-10 shows tracks printed using the anilox roll AR24. The lines have elevated edges caused by the effect of the ink being pushed out from the centre of the plate upon engagement. The effects of the raised edges are amplified due to the higher printing pressures and are a trait of the printability tester, which is pressure driven. A full size press has driven rollers and the engagement contact at the nip can be controlled by changing the engagement distance. This distance cannot be controlled on the printability tester, only the printing force. Deganello *et al* [9, 10] printed on a web-driven press and reported profiles which were rounded with no raised edges. Roughness of the lines is difficult to determine due to the nature of the ink transfer; as the plate disengages from the substrate ink is pulled apart until filament breakup occurs. This leads to an elevation of the centre of the line which gives the bulk area of the line.

Figure 4-11 and Figure 4-12 show the topography of the printed lines for the AR8 and AR24 respectively. Edges appear fairly smooth although tracks printed using the larger volume anilox which are wider than 0.3mm start to appear wavier but this is likely to be caused by the increase in ink volume. All lines, with the exception of the 0.1mm nominal width, show a concentration of ink in the centre of the print. This should ensure that conductivity through the track is good. For anilox AR8 the 1.0mm and 2.0mm wide lines begin to appear more mottled as the ink has settled and for the higher volume anilox AR24 the 2.0mm feature shows this mottling but to a lesser degree.

Cross-sectional areas of the tracks are shown in Figure 4-13. Area is shown to increases linearly with respect to width, with the trend identical for both anilox rolls. The variability in the area is small with the wider tracks showing the greatest deviation. Areas are larger for anilox AR24 than anilox AR8 because AR24 has a greater cell volume and therefore transfers more ink to the substrate. This uniformity in the ink transfer to the plate ensures that consistent images can be reproduced with a large degree of accuracy.

Figure 4-14 shows the degree of spreading from the nominal width for the AR8 anilox. The percentage gain is greater for thinner lines. A nominal width of 0.1mm yielded a printed width of 0.24mm, a gain of 145%, whereas a nominal width of 2.0mm gave a printed line width of 2.08mm, a gain of 4.2%. Increasing the volume of ink by using anilox AR24 printed further increases the spreading (see Figure 4-15. If both anilox are compared (see Figure 4-16) then it is observed that a larger volume of ink will lead to an increase in gain. The spreading is a potential point of concern when designing printed electronic circuits, as it could cause a short-circuit, and is a factor which will need to be considered for printing current collectors for DSCs.

The average height (see Figure 4-17) is greater across all line widths for the AR24 anilox, due to the increased ink volume, but the trend for both anilox rolls is identical. Average height is almost constant between widths of 2mm and 0.5mm (approx. 0.64μm for AR24 and approx. 0.28μm for AR8) and then falls below track widths of 0.5mm. This decrease in the average height is visible in the 2D profiles (Figures 3-23 and 3-24) where the 0.1mm, 0.2mm and 0.3mm lines show a slumped centre which will result in a decreased average height.

Maximum height follows a similar trend for both anilox. Figure 4-18 shows that the maximum height falls from 0.1mm and 0.2mm for both anilox but the profiles show that the characteristic raised edges effectively split the 0.1mm lines into two, with the maximum height being at the edge of the line not the centre. For a fixed print force the smallest features on the plate exert a greater force at the nip because they have the smallest feature area. Conversely, wider features on the plate will have lower effective pressures. This pressure effect can be

related to ink spreading; thinner lines will see more ink pushed out to the edges so less ink remains in the centre.

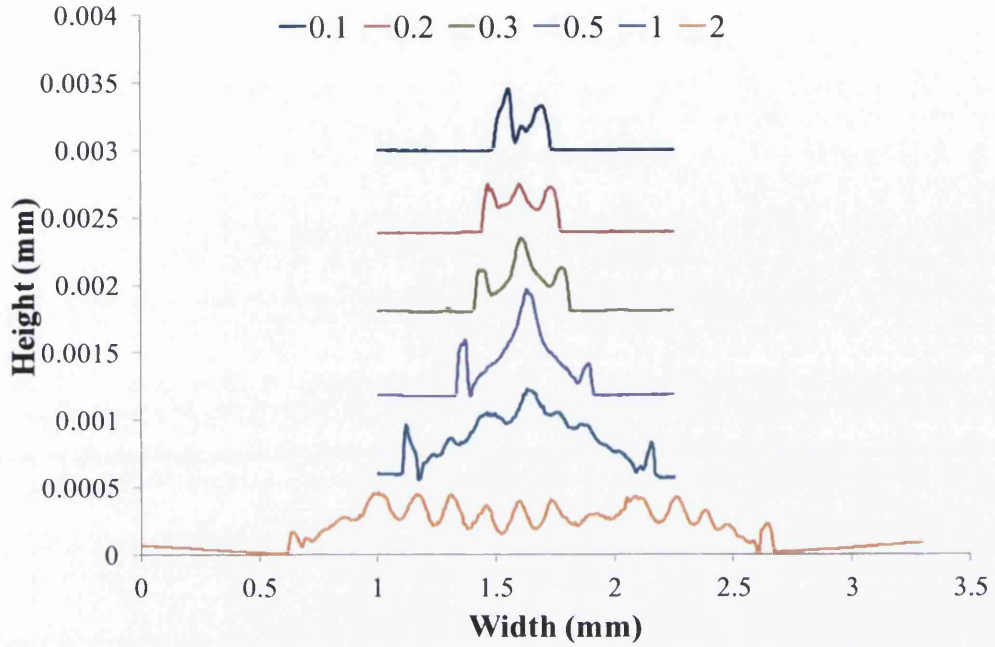

Figure 4-9 Flexographic printed cross-section profiles for anilox AR8

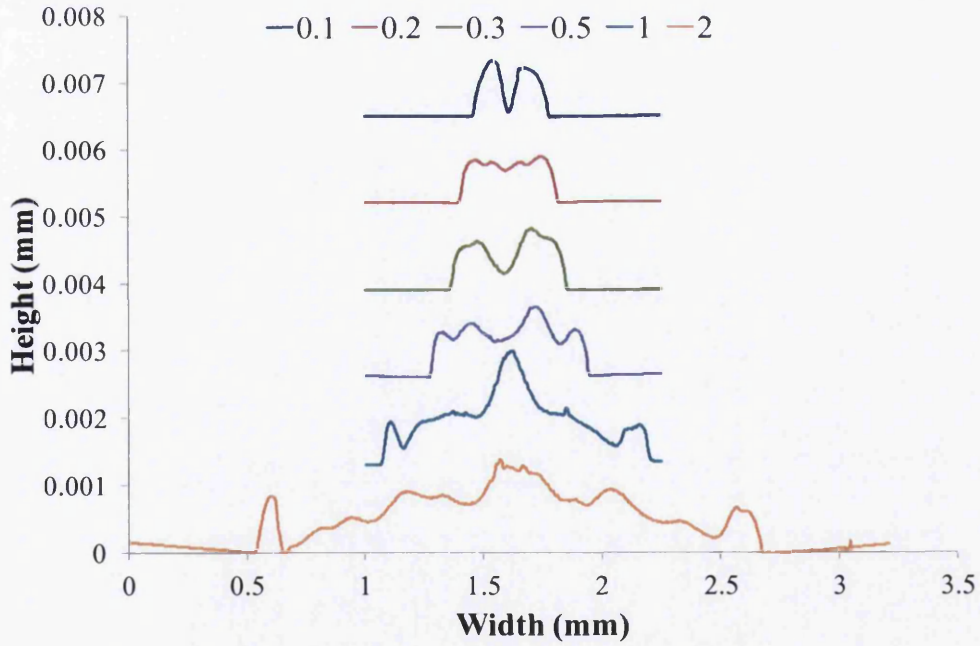

Figure 4-10 Flexographic printed cross-section profiles for anilox AR24

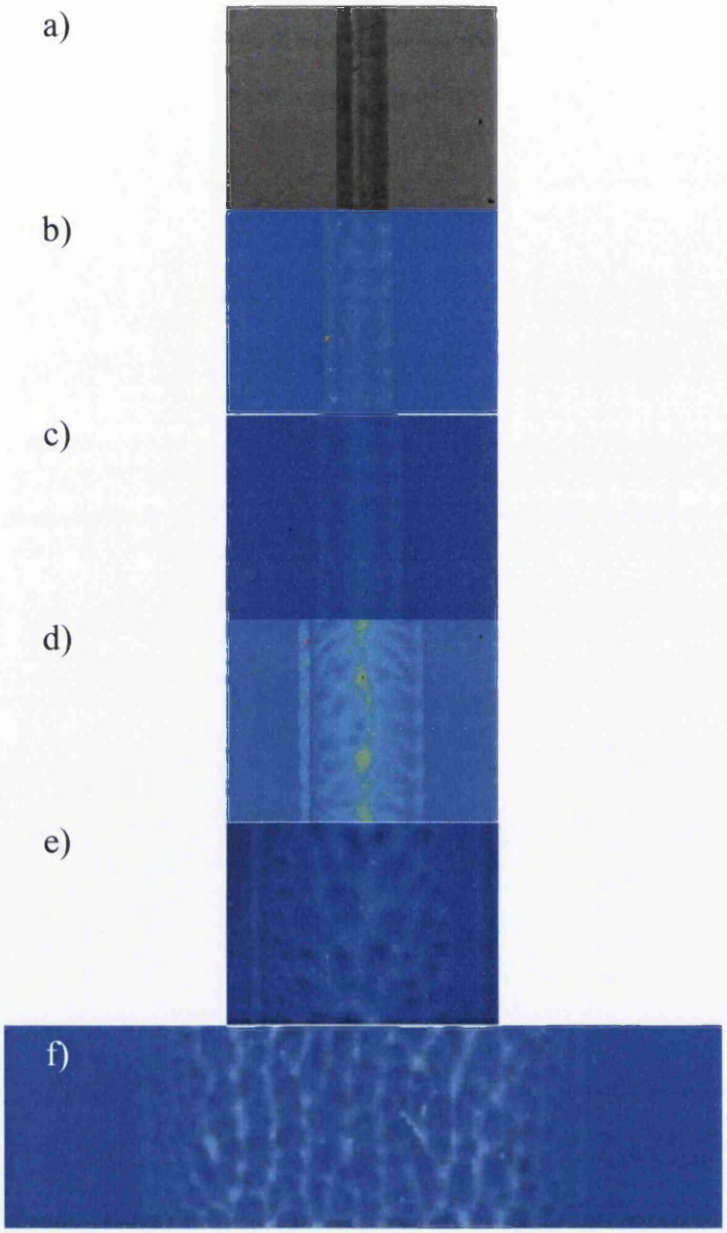

Figure 4-11 Whitelight interferometer topography images for flexographic printed lines using an anilox AR8 where: a) 0.1mm, b) 0.2mm, c) 0.3mm, d) 0.5mm, e) 1.0mm, f) 2.0mm

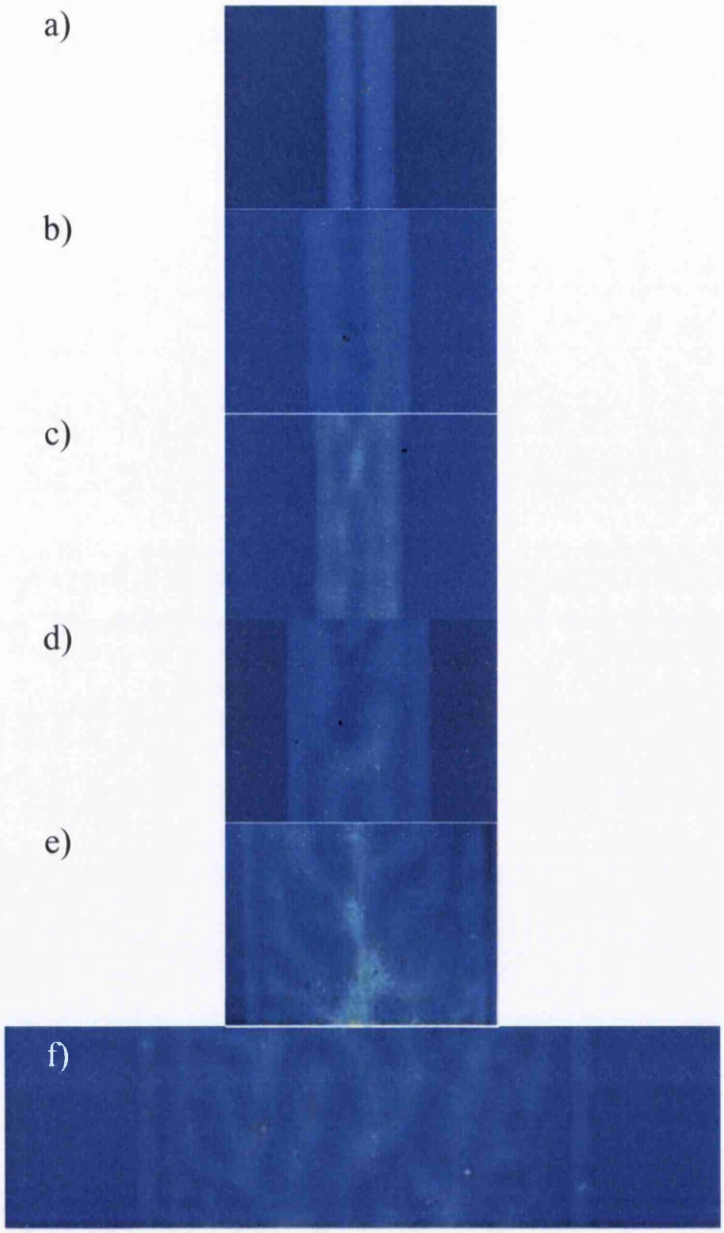

Figure 4-12 Whitelight interferometer topography images for flexographic printed lines using an anilox of volume 24cm^{3}m^{-2} where: a) 0.1mm, b) 0.2mm, c) 0.3mm, d) 0.5mm, e) 1.0mm, f) 2.0mm

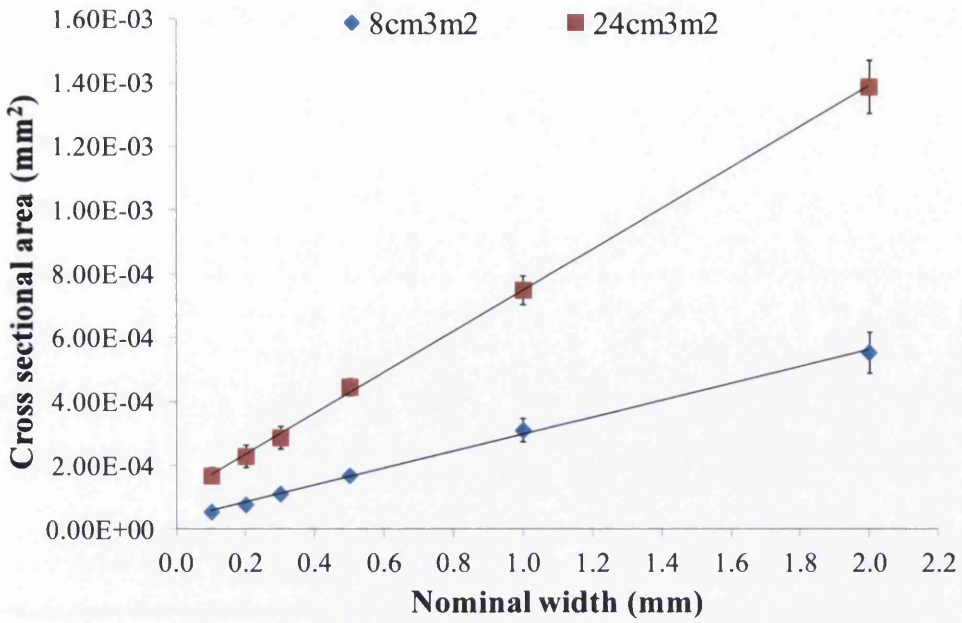

Figure 4-13 Comparison of cross sectional areas for different anilox volumes

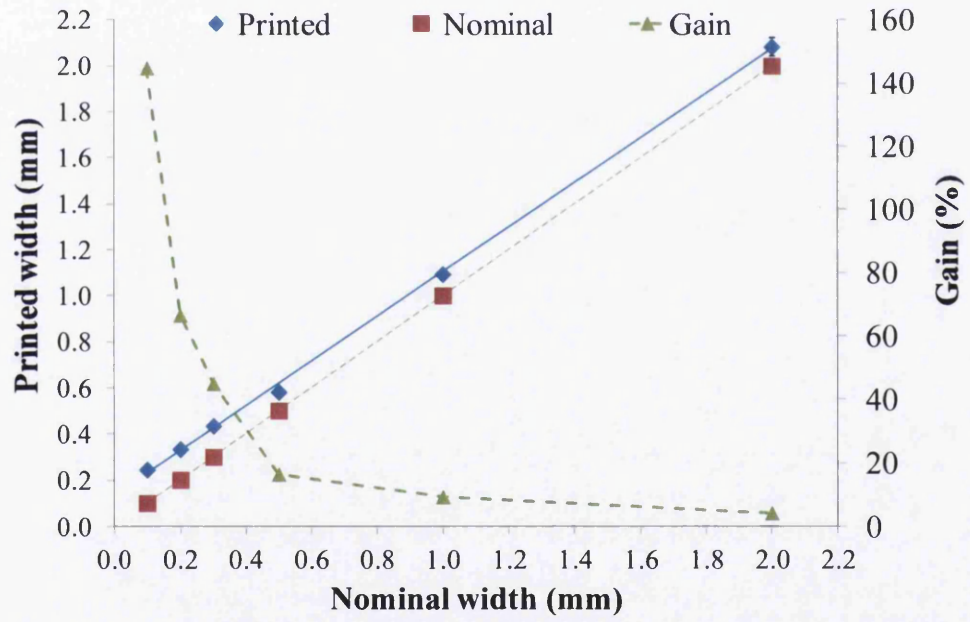

Figure 4-14 Spreading from the specified line width for anilox AR8

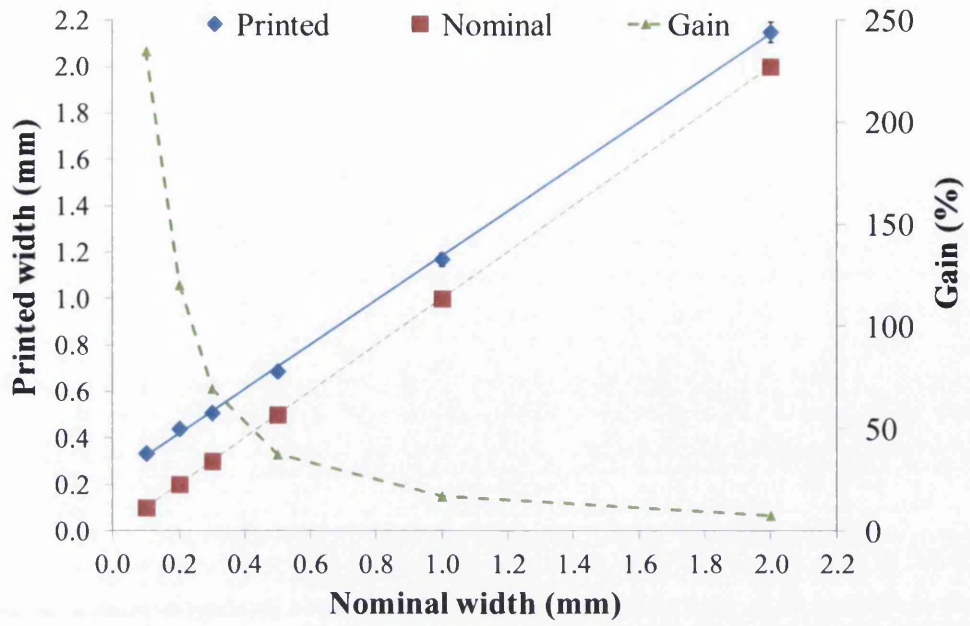

Figure 4-15 Spreading from the specified line width for anilox AR24

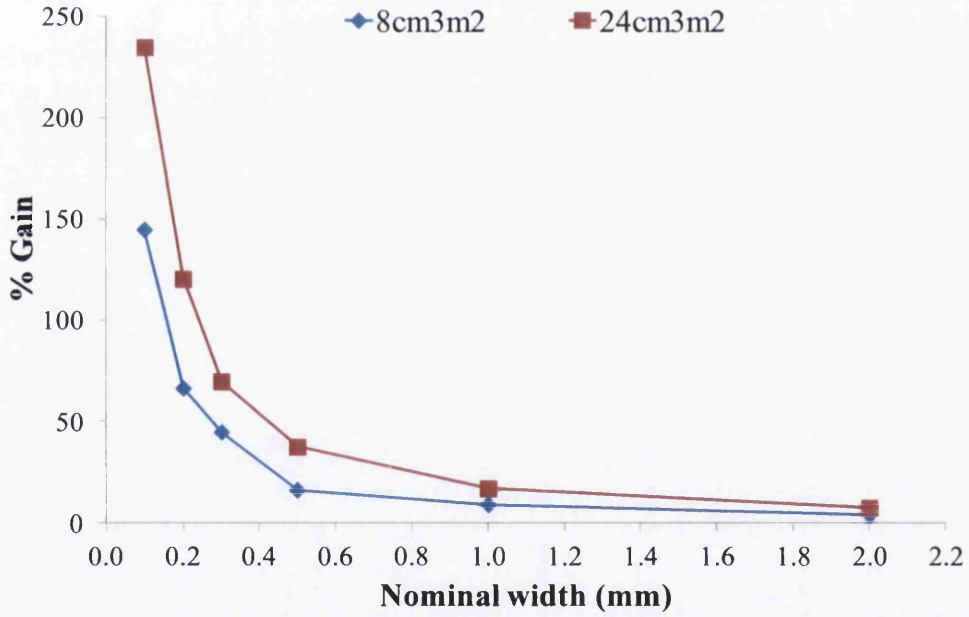

Figure 4-16 Comparison of line gain for different anilox volumes

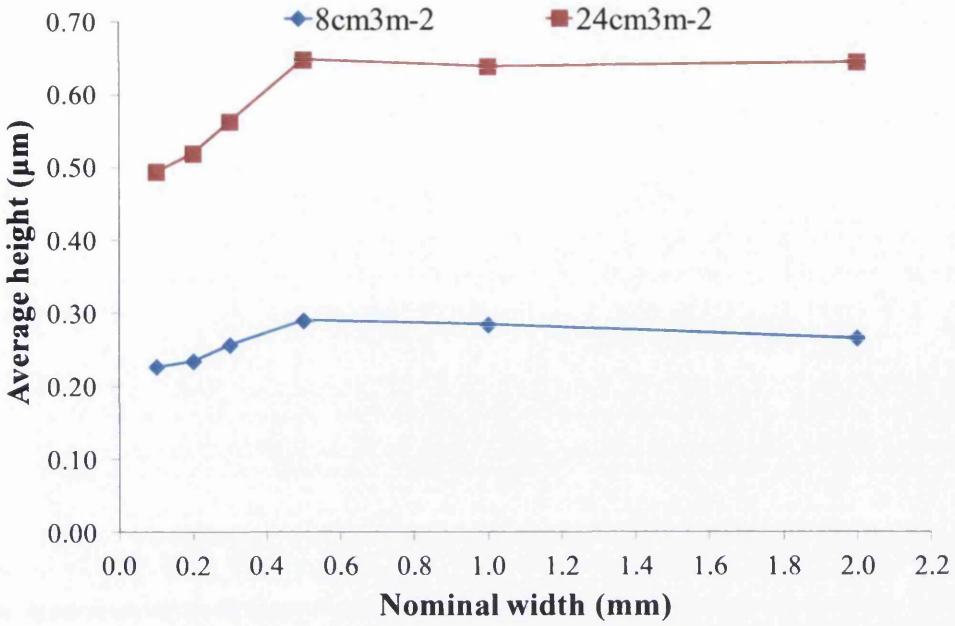

Figure 4-17 Average height comparison for different anilox rolls

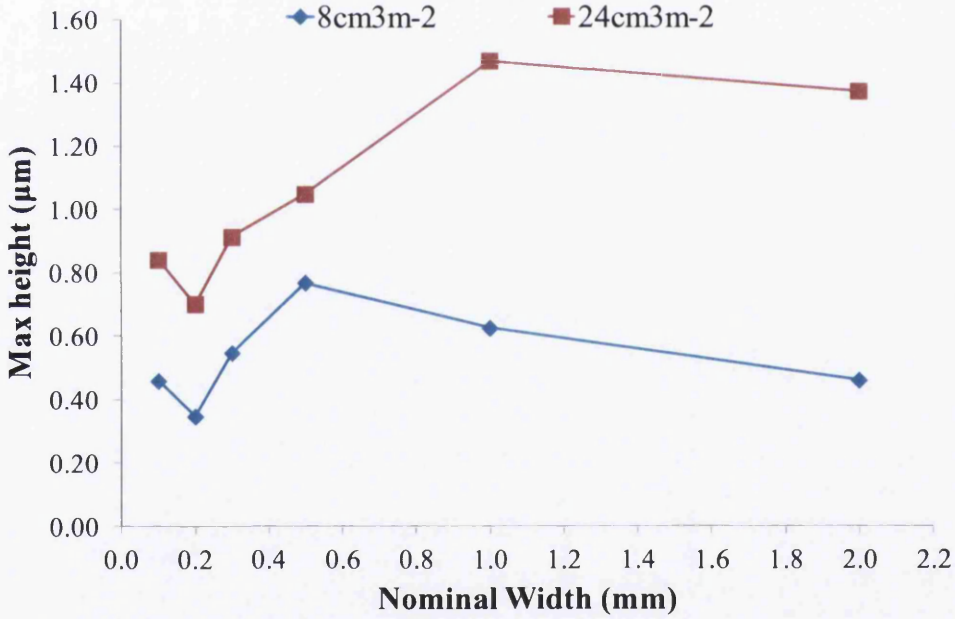

Figure 4-18 Maximum height verses line width for two anilox rolls

4.3.4 Summary

Flexographic printing can be used to print conductive tracks with excellent electrical performance. Line profiles were affected by the pressure driven nature of the printability tester and have raised edges which are not seen on profiles reported in the literature which were printed using a full size press [9, 10]. Anilox cell volume controls the thickness of the printed ink film; the larger the cell volume the greater the thickness. Printed lines are wider than specified and spreading increases with increasing anilox volume. Due to the top surface of the line being not clearly defined the roughness of the lines could not be interpreted.

For printing current collectors for DSCs the ink spreading poses a potential issue as silver is corroded by liquid electrolyte and requires isolation. Providing the gain value is known the plate image can be designed to compensate. The ability to change the volume of ink by changing the anilox specification enables the same plate to be used which reduces research costs.

4.4 Comparison of the printing technologies

4.4.1 Introduction

A comparison between screen and flexographic printing is presented using data from the printing trials. Tracks with a nominal width of 1.0mm will be compared (N.B. A comparison for the 0.3mm wide tracks could also be made but the trends are identical to those presented in this section). As each process used different silver conductive inks (because of the rheological requirements of each process) the electrical performance of inks is not compared.

This section should serve as a guide as to finding the advantages and disadvantages to consider for each printing process with respect to printed electronics and in particular for printing current collectors for DSCs so that decisions for which processes can be further investigated in this thesis.

4.4.2 Results and discussion

Comparison data for each printing process is presented in Table 4-3.

Figure 4-19 shows the profiles for the 1.0mm wide lines. The screen printed track has a much larger film thickness than the flexographic printed tracks and has the most rounded shape, suiting a low electrical resistance, because there is a greater metallic component, and best suited for overprinting, as there are minimal sharp discontinuities.

The topography of the tracks (see Figure 4-20) shows that the screen and flexographic printed tracks are continuous and have smooth edges, which minimise the possibility of a short circuit if tracks are adjacent to one another and benefits overprinting, as there are fewer discontinuities. The screen printed line has a low surface roughness whereas the flexographic lines have peaks in the centre and at the edges, where the ink is pushed out to during printing. Roughness of the flexographic line surface cannot be measured because the centre of the line is more raised than the edges because of the way the ink releases from the plate on disengagement.

For printing conductive tracks the results of the track morphology indicate that, screen printing is ideal as it is offers a line with a homogenous rounded profile and flexography is also good, particularly in the centre of the line where the bulk of the ink is, but the undulations in the profile could cause issues for overprinting, although film thickness is an order of magnitude smaller than the screen printed line.

The track with the largest cross-sectional area should yield the best electrical performance, as it should possess the greatest amount of conducting material. Differences in the cross-sectional area are shown in Figure 4-21. The largest area is exhibited by the screen printed track and it would be expected to be the best method for printing a high conductivity track with the flexographic printed track being much worse.

Spreading (see Figure 4-22) is much greater for the flexographic printed tracks. The reason for this trend is due to the processes: **Flexography 'squeezes' ink** between the plate and substrate upon printing, thus forcing it out from the centre. Screen printing pushes a comparatively large volume of ink through a mesh and the ink will settle and spread on the substrate. When considering current collector design for DSCs spreading is an important factor to consider as it cause the current collectors to come into contact with the active cell area and potentially contaminating it.

As Figure 4-23 shows, the screen printed track has the largest average height (9.12μm), then the flexographic printed tracks (AR24 = 0.64μm, AR8 = 0.29μm). The maximum height of the screen printed line was the greatest and the small volume anilox AR8 flexographic line gave the smallest. The difference between the screen printed tracks and others is of an order of magnitude with the ink deposit being >90% less for flexographic printed tracks. This offers a potential saving in materials costs.

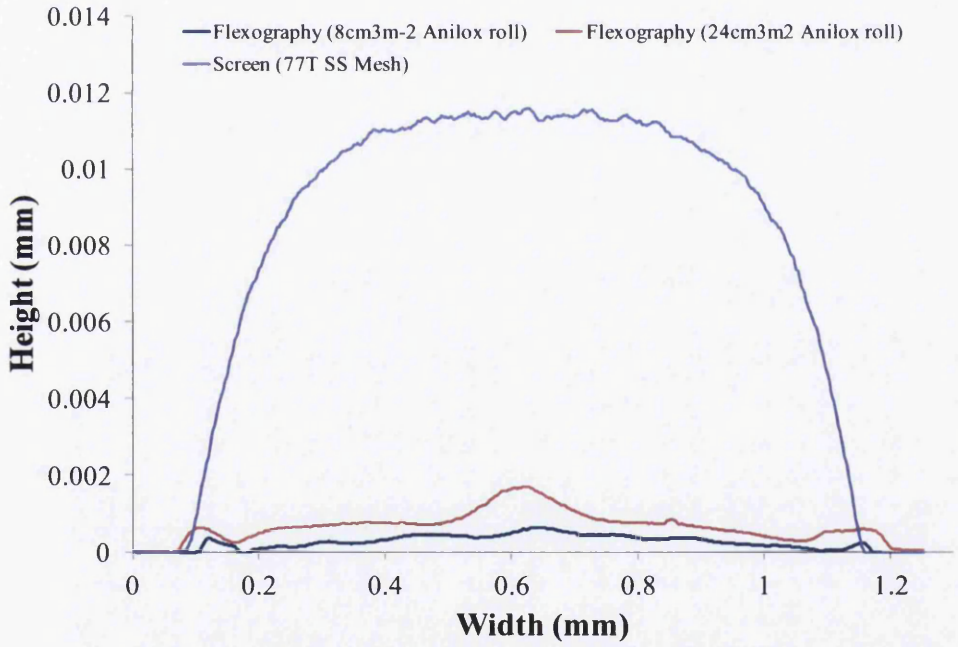

Figure 4-19 Comparison of cross-section profiles for different printing technologies

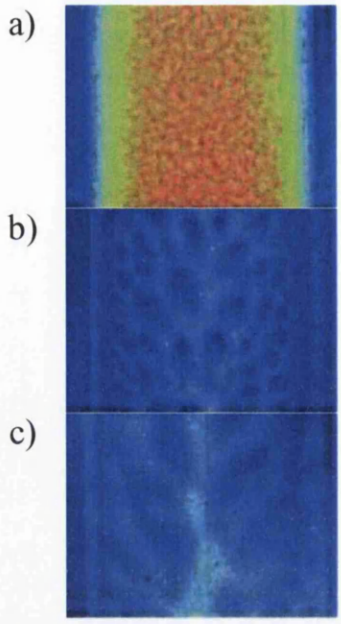

Figure 4-20 Whitelight interferometer topography images for 1.0mm wide lines printed using: a) screen printing, b) flexography (AR8), c) flexography (AR24)

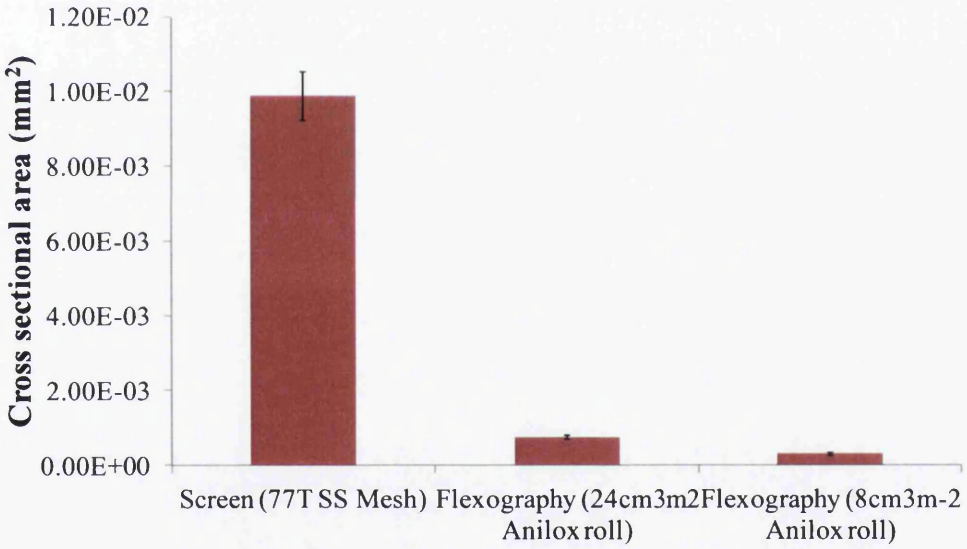

Figure 4-21 Comparison of the cross-sectional areas for a 1.0mm wide line printed using different printing technologies

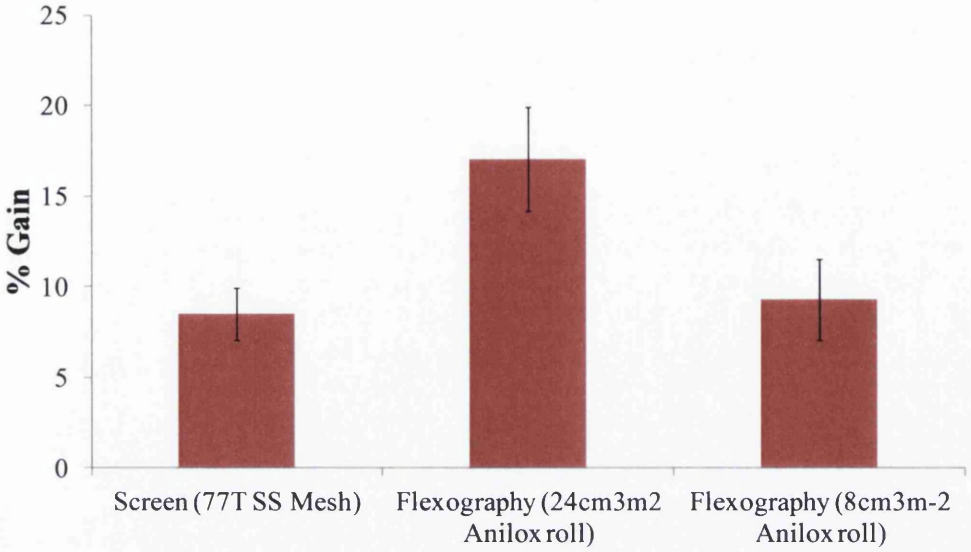

Figure 4-22 Comparison of the percentage width gain from the nominal 1.0mm line width for each printing technology

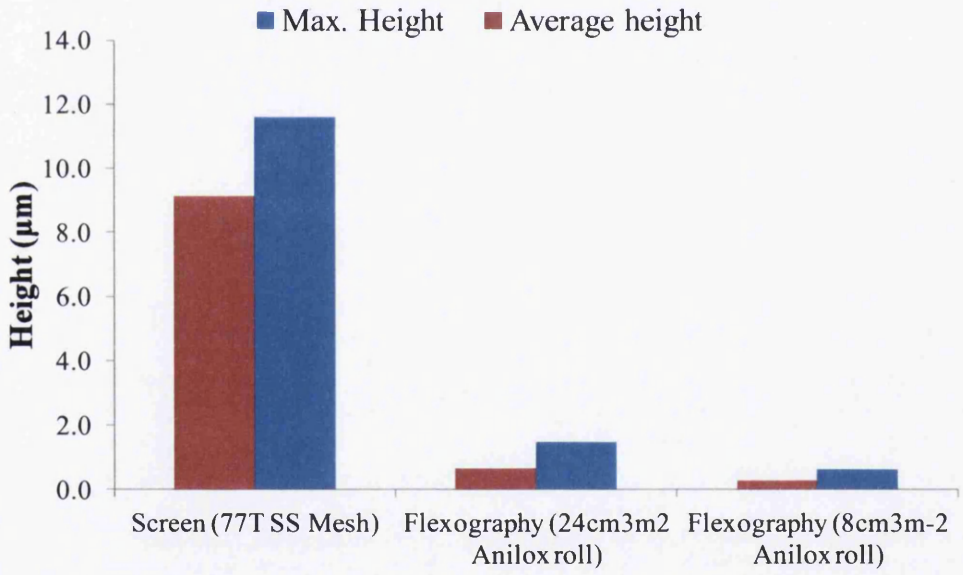

Figure 4-23 Comparisons of the maximum and average height for each printing technology

Table 4-3 Comparison of key factors for 1.0mm tracks deposited using different printing technologies

Printing technology	Printed width (mm)	Gain (%)	Average height (μm)	Maximum height (μm)	Cross-sectional area (μm^2)	Ra (μm)	Ra / Average height
Flexography (AR8)	1.093 ± 0.022	9.28	0.285	0.625	311.2 ± 26.52	-	-
Flexography (AR24)	1.170 ± 0.029	17.05	0.639	1.471	750.2 ± 44.57	-	-
Screen (77T)	1.085 ± 0.014	8.50	9.118 ± 0.697	11.60	9892 ± 657.8	1.92	0.21

4.5 Conclusions

For printing current collecting grids for DSCs flexography offers a thin-film alternative to screen printing with a printed thickness which is ~90% less. In terms of silver metal used this represents a potentially large saving in the materials cost.

Both printing technologies tested in this chapter have advantages and disadvantages regarding their suitability for printing conductive tracks for current collectors in DSCs:

- Screen printed tracks exhibited excellent continuity with few apparent defects. The large volume of ink printed ensures that the cross-sectional area is large making it an ideal process for printing conductive features. A disadvantage is that a large cross-sectional area means that a high volume of ink is printed and therefore a greater amount of silver metal is used which is expensive. Feature resolution and film thicknesses are controlled by the mesh.
- Flexographic printed tracks have smooth edges with the bulk of the ink in the centre of the line giving continuous, highly conductive tracks. The ink build up at the edges of the lines, caused by the nature of the printability tester, results in an area of the line which may not actually benefit the overall conductivity. Printed thickness can be varied by changing the volume of the anilox roll without changing the image master, something which cannot be done with screen and rotogravure.

4.6 References

1. Horwood, R.J., *Towards a better understanding of scrren print thickness control.* Electrocomponent Science and Technology, 1974. **1**: p. 129-136.
2. Firor, K. and S. Hogan, *ENVIRONMENTAL TESTING OF SINGLE-CRYSTAL SILICON SOLAR-CELLS WITH SCREEN-PRINTED SILVER CONTACTS.* Ieee Transactions on Reliability, 1982. **31**(3): p. 270-275.
3. Frisson, L., P. Lauwers, R. Mertens, R. Vanoverstraeten, and R. Govaerts, *SCREEN PRINTED METALLIZATION OF SILICON SOLAR-CELLS.* Electrocomponent Science and Technology, 1980. **7**(1-3): p. 107-111.
4. Ju, M., Y.-J. Lee, J. Lee, B. Kim, K. Ryu, K. Choi, K. Song, K. Lee, C. Han, Y. Jo, and J. Yi, *Double screen printed metallization of crystalline silicon solar cells as low as 30 mu m metal line width for mass production.* Solar Energy Materials and Solar Cells. **100**: p. 204-208.
5. Hashmi, G., K. Miettunen, T. Peltola, J. Halme, I. Asghar, K. Aitola, M. Toivola, and P. Lund, *Review of materials and manufacturing options for large area flexible dye solar cells.* Renewable & Sustainable Energy Reviews. **15**(8): p. 3717-3732.
6. Owczarek, J.A. and F. Howland, *A study of the off-contact screen printing process. I. Model of the printing process and some results derived from experiments.* Components, Hybrids, and Manufacturing Technology, IEEE Transactions on, 1990. **13**(2): p. 358-367.
7. Fox, I.J., M.F.J. Bohan, T.C. Claypole, and D.T. Gethin, *Film thickness prediction in halftone screen-printing.* Proceedings of the Institution of Mechanical Engineers Part E-Journal of Process Mechanical Engineering, 2003. **217**(E4): p. 345-359.
8. Cao, k., k. Cheng, and z. Wang, *Optimization of screen printing process.* ICEPT: 2006 7th International Conference on Electronics Packaging Technology, Proceedings, ed. B. Kenyun. 2006. 320-323.
9. Deganello, D., J.A. Cherry, D.T. Gethin, and T.C. Claypole, *Patterning of micro-scale conductive networks using reel-to-reel flexographic printing.* Thin Solid Films. **518**(21): p. 6113-6116.
10. Deganello, D., J.A. Cherry, D.T. Gethin, and T.C. Claypole, *Impact of metered ink volume on reel-to-reel flexographic printed conductive networks for enhanced thin film conductivity.* Thin Solid Films. **520**(6): p. 2233-2237.
11. Frey, M., F. Clement, S. Dilfer, D. Erath, and D. Biro, *Front-side Metalization By Means Of Flexographic Printing*, in *Proceedings of the Siliconpv 2011 Conference*, S. Glunz, et al., Editors. p. 581-586.
12. Kwak, M.K., K.H. Shin, E.Y. Yoon, and K.Y. Suh, *Fabrication of conductive metal lines by plate-to-roll pattern transfer utilizing edge dewetting and flexographic printing.* Journal of Colloid and Interface Science. **343**(1): p. 301-305.
13. Yusof, M.S., T.V. Korochkina, T.C. Claypole, and D.T. Gethin, *An investigation into deformation of photopolymer plate during printing solid lines in flexography.* Constitutive Models for Rubber V, ed. A. Boukamel, et al. 2008. 433-437.

14. Bould, D.C., T.C. Claypole, and M.F.J. Bohan, *An investigation into flexographic printing.* Proceedings of the Institution of Mechanical Engineers Part B-Journal of Engineering Manufacture, 2004. **218**(11): p. 1499-1511.
15. Korochkina, T.V., J.A. Cherry, T.C. Claypole, and D.T. Gethin, *Effect of plate technology and orientation on flexographic line deformation.* Constitutive Models for Rubber Vi, ed. G. Heinrich, et al. 383-388.

5 Printing methods for metallization of flexible dye solar cells

5.1 Introduction

The scale-up of a dye solar cell (DSC) means that the photoactive area of the cell will increase in size. Increasing the size of the active area increases the distance electrons have to travel to the external load. Any resistance to the flow of electrons will impede the cell performance and because of this the sheet resistance of the transparent conducting layer (TCO) on the electrodes becomes more and more important to maintaining cell performance as cell size increases.

It is common for laboratory made DSCs to be $\leq 1cm^2$ in size and, prior to characterizing the cell performance, to metalize the electrodes through the application of a layer of metallic paste or solder to improve the electrode contact by reducing the resistance of the TCO layer. An increase in cell size greater than $1cm^2$ creates a need to deposit current collecting tracks around the active areas. When large DSCs (10cm x 10cm) have been produced on FTO glass substrates, without current collectors, efficiency has been shown to be less than 1% [1].

A simple way to reduce the electrode resistance is to use a metal substrate and these are discussed in chapter 2. The best performing metal substrates for DSCs are titanium and stainless steel as they have shown the best corrosion resistance to iodide/triiodide electrolyte [2].

Flexible DSCs using titanium as a working electrode (WE) substrate and ITO/PET [3] or ITO/PEN [4] counter electrode (CE) substrates has been demonstrated to produce DSCs with efficiencies of 2.9% and 7.2% respectively. The active area for these cells is very low with the ITO/PET cell area just $0.25cm^2$. The aims of this investigation are to produce large area flexible DSCs with titanium WEs and an ITO/PET CEs. The active area will be $4cm^2$ and current collectors will be printed onto the CE to observe their effect on the cell performance by reducing the CE resistance. Both thick film screen printing and

thin film flexographic printing methods will be used to deposit conductive inks for the current collection grids.

5.2 Experimental

Figure 5-1 illustrates the design of the flexible DSCs, which were prepared as described in Chapter 3. Printed current collectors were measured for their electrical resistance and resistivity using the four-point probe method outlined in and track geometry was measured using white-light interferometry, described in Chapter 3. It should be noted that the active area of the cells in this study is $4.0cm^2$.

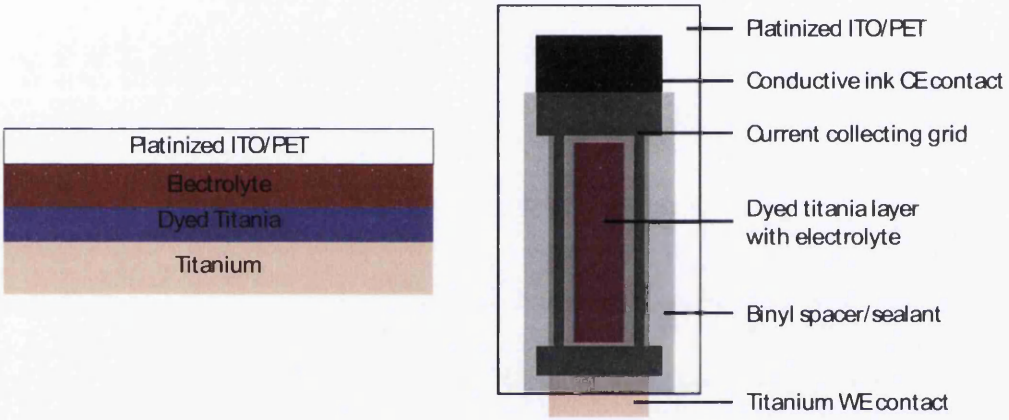

Figure 5-1 Schematic of the flexible DSC design

5.3 Results and discussion

The results are split into three sections: The first will investigate the effect of ink drying time on the cell performance for DSCs with screen printed PTF microparticle silver ink current collectors. The second investigates using flexographic printing to deposit thin-film nanoparticle silver current collectors and compares printing different track widths on DSC performance. The third section compares the performance of DSCs prepared with screen printed and flexographic printed current collectors.

5.3.1 Effect of ink drying time on the performance of DSCs with screen printed current collectors

5.3.1.1 Current collector characterization

Current collecting grids were screen printed onto the ITO/PET substrate as shown in Figure 5-2 and the track geometry data is presented in Table 5-1.

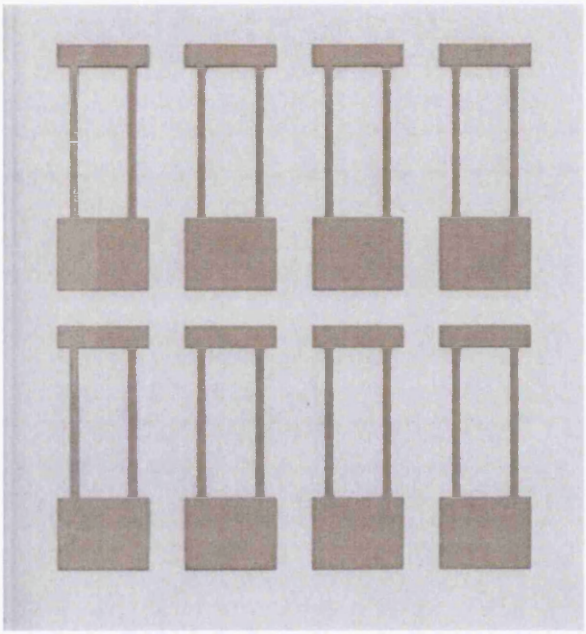

Figure 5-2 Screen printed PTF silver current collection grids for DSC counter electrode.

Table 5-1 Geometric parameters for screen printed current collectors

Nominal track width (mm)	Printed track width (mm)	Average height (mm)	Maximum height (mm)	Cross-sectional area (mm^2)
2.00	2.15 $\pm 3.09 \times 10^{-2}$	9.10×10^{-3} $\pm 4.55 \times 10^{-4}$	1.24×10^{-2} $\pm 5.59 \times 10^{-4}$	1.96×10^{-2} $\pm 9.55 \times 10^{-4}$

The electrical performance of the current collecting tracks dried in an oven at 150°C for different times is illustrated in Figure 5-3 with data presented in Table 5-2. The tracks exhibiting the lowest resistance are those dried for the longest time for 10 minutes which exhibits a resistivity which equates to approximately 6 times bulk silver. The grids dried for 5 and 2 minutes show an increase in resistivity relative to bulk silver of about 10 and 19 times respectively. The decrease in resistivity with increased drying time is because the PTF silver ink has an organometallic silver compound, present in the ink vehicle, which decomposes upon thermal heating (at ≥150°C) to form nanoparticle silver, which acts to 'chemically weld' the large silver particles, reducing the inter-particle contact resistance. The oven temperature was chosen because above 150°C the ITO/PET showed signs of thermal degradation and below 150°C the organometallic decomposition would not occur resulting in higher resistances.

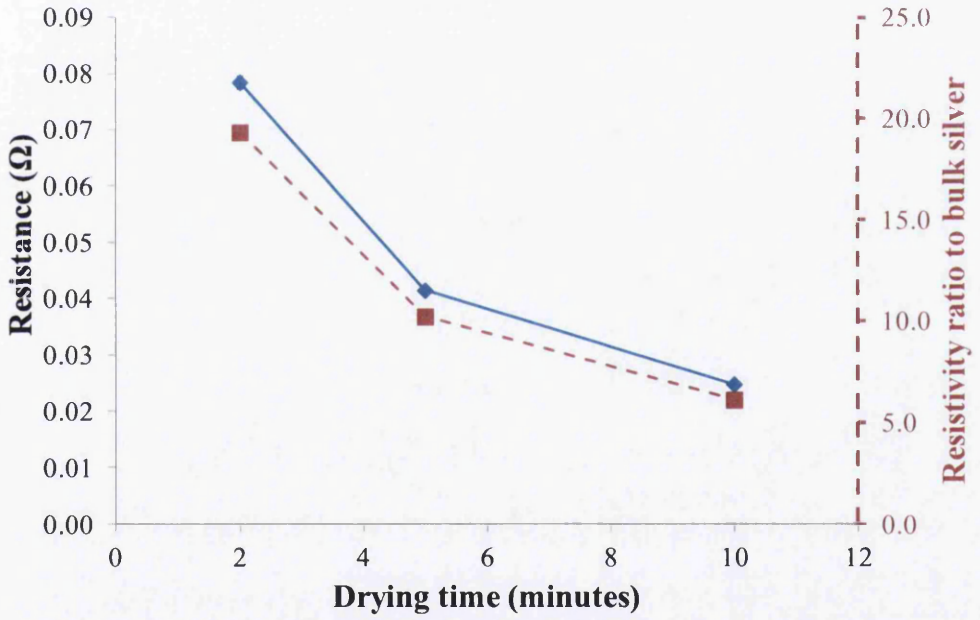

Figure 5-3 Effect of drying time on electrical performance for a 2mm wide screen printed PTF silver current collecting track.

Table 5-2 Electrical performance data for 2mm wide screen printed PTF silver tracks

Drying time (minutes)	Average resistance (Ω)	Resistivity* (Ω.m)	Ratio to bulk silver
2	0.0785 ± 0.0011	3.07×10^{-7}	19.3
5	0.0414 ± 0.0003	1.62×10^{-7}	10.2
10	0.0247 ± 0.0008	9.69×10^{-8}	6.1

*Average cross sectional area used to calculate resistivity is $1.96 \times 10^{-8} m^2$

5.3.1.2 DSC performance

Figure 5-5 shows the current voltage plots for cells produced with current collectors dried for different periods of time. Also included is a control cell produced in an identical manner but with no current collectors. Details of the cell performances are given in Table 5-3 where averaged data is presented.

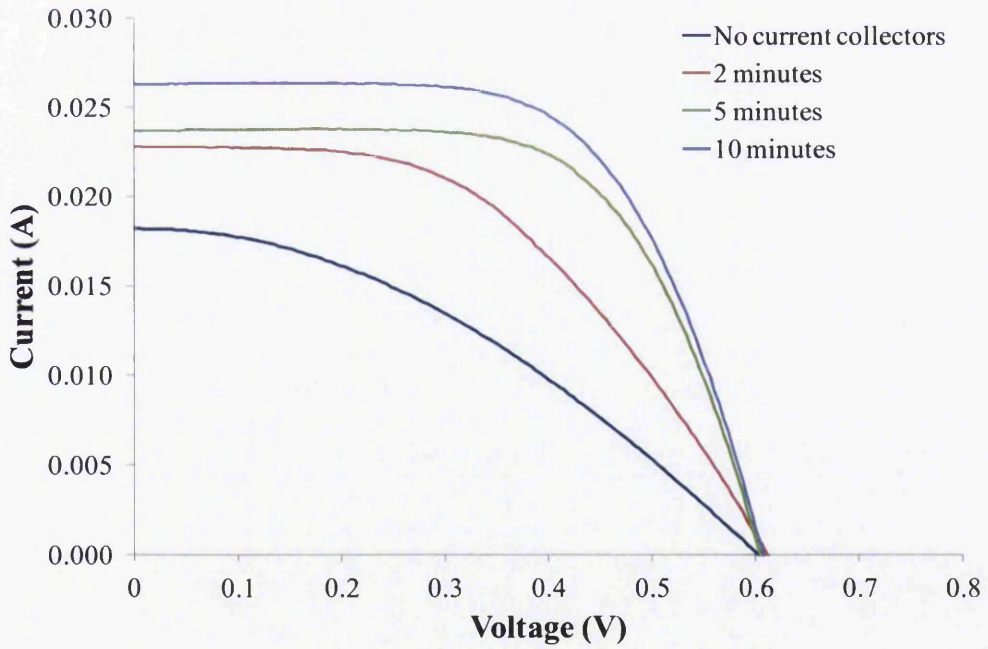

Figure 5-5 Effect of drying time on I-V responses obtained under illumination at 1 sun

Table 5-3 Comparison of averaged cell parameters for DSCs built with current collectors screen printed using a PTF silver ink and dried for different times. Standard deviations for each data set are shown in parentheses.

Current collector drying time (minutes)	Voc (V)	Isc (mA)	Jsc (mA/cm^2)	Pmax (mW)	Fill factor (%)	Efficiency (%)
2	0.61	23.4	5.84	6.91	48.5	1.73
	(0.003)	(0.001)	(0.20)	(0.89)	(4.86)	(0.22)
5	0.61	24.3	6.09	9.50	64.0	2.37
	(0.004)	(0.001)	(0.17)	(0.43)	(1.72)	(0.11)
10	0.61	26.1	6.53	10.1	63.0	2.51
	(0.009)	(0.001)	(0.32)	(0.83)	(2.15)	(0.21)
Control	0.61	16.0	3.99	3.62	37.8	0.91
	(0.009)	(0.002)	(0.62)	(0.32)	(3.20)	(0.08)

Increasing the drying time of the ink has been shown to increase the electrical performance. In terms of cell performance the Voc for all the cells is constant but slightly lower than reported in the literature for cells made using the same electrolyte [5]. This is believed to be because of the thick TiO_2 layer (22.5μm) the injected electrons are required to travel much further to reach the titanium substrate. This effect is also magnified because the cells are reverse illuminated, i.e. incident light has to pass through the CE and electrolyte before reaching the WE.

The Isc (and Jsc) increases with ink drying time with the control cells, with no current collectors, showing the lowest value. The highest short circuit current density (Jsc) values agree with those reported in the literature for cells built using ITO/PET CEs on titanium [3] and cells built with FTO glass on titanium [6] which are $6.71mA/cm^2$ and $6.94mA/cm^2$ respectively. However, the Jsc value is some way off the $13.6mA/cm^2$ reported by the Gratzel group [4].

The maximum power (Pmax) also increases with the drying time of the ink. Pmax values for the control cells are almost half that of the worst performing cells with current collectors which shows the effect that even poorly conducting silver ink has.

The fill factor, FF, (NB. ratio of Pmax / Jsc x Voc) is an important indicator of cell performance and the closer to 100% the better the cell performs. A current collector drying time of 5 minutes (64%) actually results in a 1% improvement in FF over the cells with 10 minutes drying time (63%). This is despite the Jsc and Pmax values being less. The 2 minute dried cells record the lowest FF for cells with current collectors of 48.5% and the control cells have the lowest FF with 37.8%. The differences in FF can be visualized by observing the I-V plots (Figure 5-5). In comparison to the literature, the FFs are slightly higher than those reported by Onoda (54%) [6] and Chang (61%) [3] but lower than Ito (68%) [4].

Light to electricity conversion efficiency shows that cells with the best performing current collectors, i.e. a longer drying time, outperform the rest. A drying time of 10 minutes results in cells with an efficiency of 2.51%. Reducing the drying time and efficiency falls to 2.37% and 1.73%, for 5 minutes and 2 minutes respectively, and is 0.91% for the control cells.

Table 5-4 shows data for the electron impedance spectroscopy (EIS) scans run on the cells to determine the substrate resistance (Rs) of the cells. The scans were run at open circuit bias of -0.6V. The plan was to use the data to see the effect that the drying time of the ink, or increase in electrical performance, had on Rs. The results show that the highest Rs are shown by the control cells. There is then a marked decrease of an order of magnitude in Rs when current collectors are used with the 5 minutes dried cells showing lower Rs than the 10 minutes cells. The standard deviations of the data, also presented in the table, are extremely large so the data is not very conclusive although the literature reports that Rs increases with the sheet resistance of the substrate [7].

Table 5-4 How drying time affects the substrate resistance of a DSC measured using EIS.

Current collector drying time (minutes)	Substrate resistance, Rs (Ω)*	Standard deviation (Ω)
2	1.97	1.18
5	1.52	0.43
10	1.60	0.34
Control	49.0	42.3

*Measured at a bias of -0.6V

5.3.1.3 Summary

DSCs with screen printed current collectors (Figure 5-6) have shown that the drying time of the conductive ink is of great importance to the performance of the cell. The longer the drying time the lower the resistivity of the ink and the greater the Jsc, FF and efficiency. DSCs with current collectors which have not been optimized for best resistivity outperform DSCs with no current collectors.

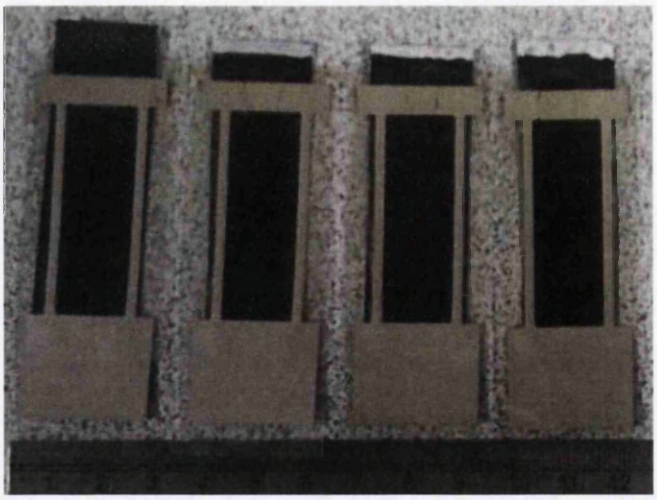

Figure 5-5 Flexible DSCs with titanium WE and ITO/PET CE with screen printed current collectors

5.3.2 Flexographic printed current collectors

DSCs have been shown to perform well with screen printed current collectors using a PTF microparticle silver ink. Screen printing is by nature a thick film deposition technology (see Chapter 4) and the DSCs produced using screen printed current collectors had an average track height of 9.1μm. With the cost of silver representing a large cost component in the manufacture of DSCs [8] reducing the amount of silver without compromising cell performance is an attractive goal. Flexographic printing has been employed to print a nanoparticle silver ink to see if printing a thin-film of silver can produce good performing DSCs. The benefits of using a nanoparticle ink, rather than a PTF ink, are that particle sintering at low temperatures, even room temperature, is possible which is beneficial when polymer substrates, which are temperature sensitive, are used. Cells with current collectors with 2mm wide tracks have been produced to compliment the screen printed current collectors using a small volume and large volume anilox.

5.3.2.1 Current collector characterization

Table 5-5 gives the specifications for the anilox rolls used in this study. The cell volumes for the anilox rolls are an order of magnitude in difference to allow a range of thin-films to be deposited.

Table 5-5 Anilox roll specifications

Reference	Cell volume (cm^3/m^2)	Line ruling (l/cm)	Line ruling (l/inch)	IGT Part number
AR2.7	2.7	235	600	402.419
AR12	12	120	300	402.411

Examples of the current collectors which have been flexographic printed can be seen in Figure 5-7 and their geometries are presented in Table 5-6. Cross-sectional areas of the tracks with anilox volume, which follows the trends

observed in chapter 4. The printed width will always be wider than the specified width due to the nature of flexographic printing (c.f. Chapter 4) and current collectors were designed to take the spreading into consideration so that no encroachment of the silver into the active area of the cell would occur. Average heights for the tracks are 74nm for the AR2.7 anilox and 436nm for the AR12.

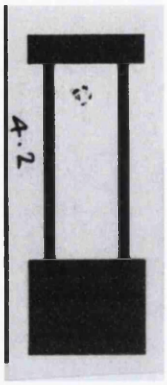

Figure 5-7 Flexographic printed current collectors for DSC counter electrodes

Table 5-6 Geometric parameters for flexographic printed current collecting tracks

Anilox	Nominal track width (mm)	Printed track width (mm)	Average height (mm)	Maximum height (mm)	Cross-sectional area (mm^2)
AR2.7	2	2.21 $\pm$ 4.51 x 10^{-2}	7.42 x 10^{-5}	1.54 x 10^{-4}	1.64 x 10^{-4} $\pm$ 1.39 x 10^{-5}
AR12	2	2.37 $\pm$ 5.2 x 10^{-2}	4.36 x 10^{-4}	9.05 x 10^{-4}	1.03 x 10^{-3} $\pm$ 8.25 x 10^{-5}

The electrical performances of the nanoparticle silver ink tracks are shown in Table 5-7. The ink was dried for 10 minutes in an oven at 130°C which was found to be the optimal sintering time. Tracks printed using the AR2.7 anilox exhibit higher resistances than those printed using the AR12. This is due to the difference in printed thickness.

Table 5-7 Electrical performance of flexographic printed current collectors

Anilox	Track width (mm)	Resistance (Ω)	Resistivity (Ω.m)	Ratio to bulk silver
AR2.7	2	2.41 ±0.13	7.19×10^{-8}	4.97
AR12	2	0.36 ±0.01	7.41×10^{-8}	4.66

5.3.2.2 DSC performance

Figure 5-8 shows representative current voltage plots for the DSCs produced with current collectors using different anilox volumes. Details of the cell parameters are given in Table 5-8.

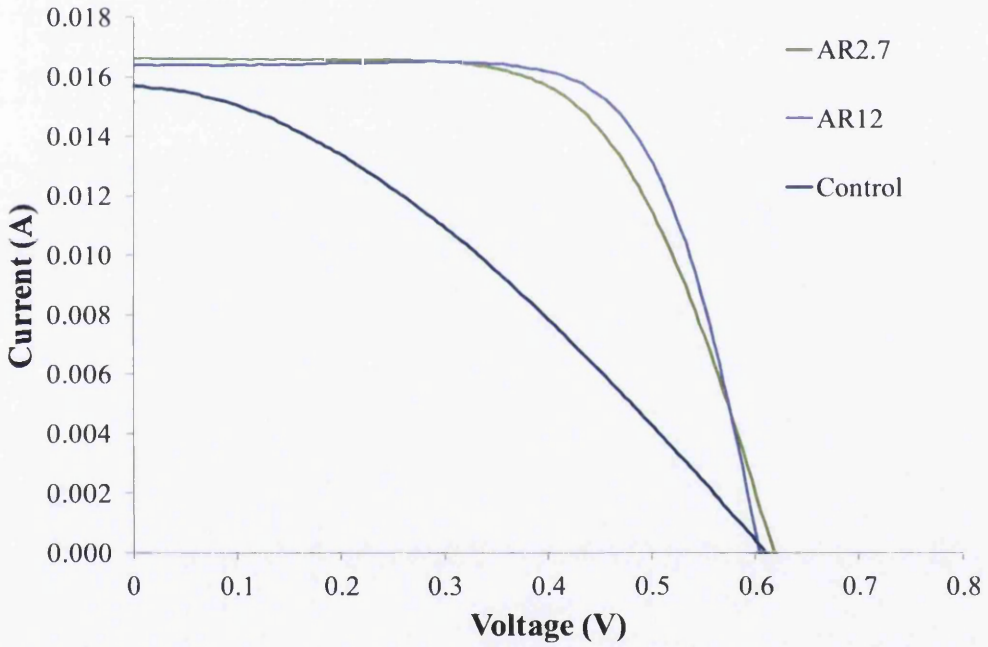

Figure 5-8 Current voltage responses obtained under illumination at 1 sun

Table 5-8 Comparison of measured cell parameters for flexographic printed current collectors. Standard deviations are shown in parenthesis.

Anilox	Track width (mm)	Voc (V)	Isc (mA)	Jsc (mA/cm^2)	Pmax (mW)	Fill Factor (%)	Efficiency (%)
AR2.7	2	0.61 (6e-3)	16.9 (3e-3)	4.23 (0.63)	6.54 (0.85)	63.7 (1.62)	1.63 (0.21)
AR12	2	0.60 (5e-3)	16.7 (2e-3)	4.17 (0.50)	6.98 (0.79)	69.6 (1.04)	1.74 (0.20)
Control	n/a	0.61 (9e-3)	16.0 (2e-3)	3.99 (0.62)	3.62 (0.32)	37.8 (3.20)	0.91 (0.08)

In general cells built with current collectors printed using the larger volume AR12 anilox outperform those built using the smaller volume AR2.7 anilox. Both types of cells with current collectors show a clear improvement in performance over the control cells built with no current collectors.

Considering each of the parameters individually:

The Voc values are nearly identical for all cells and is slightly lower than the 0.66V reported by Chang *et al* for cells built using titanium and ITO/PET [3]. The reasoning behind the decrease is because of a combination of the reverse cell effect and the thickness of the TiO_2 layer previously explained.

The best Isc (and Jsc) is exhibited by cells with tracks printed with the AR2.7 anilox, then the AR12 anilox and the worst photocurrent is produced by the control cells. The values of Jsc are less than comparative flexible cells reported in the literature using titanium WEs and plastic CEs [3, 4] although the active area for these cells is much larger than any reported in the literature. A reason for the AR2.7 cells producing a higher Isc than the AR12 cells could be due a variance in the platinum thickness during the chemical platinization process.

Fill factor (FF) shows an increase with anilox volume and therefore thickness of the current collectors. Control cells without current collectors exhibit a low FF. The FF values for are significantly larger than reported in the literature (54% [3] and 61% [6]) [3, 6] and cells with current collectors printed using the AR12 anilox have FFs better than those produced by the Gratzel group [4] who achieved a FF of 68%.

Efficiencies range from 1.6%, for the AR2.7 cells, to 1.7%, for the AR12 cells with the control cells just 0.9%. These are lower than those reported in the literature but this is likely to be because the cell active area ($4cm^2$) is larger than those reported ($0.25cm^2$ [3], $0.5cm^2$ [6]).

Table 5-9 presents the substrate resistance (Rs) data measured using EIS. The Rs is lower for the cells with current collectors printed using the AR12 anilox and the highest Rs is shown by the control cells. However, the variance in the data is huge so although the data follows the same trends for the cell performance and electrical performance of the current collectors it is not very reproducible.

Table 5-9 Substrate resistance of DSCs with flexographic printed current collectors

Anilox	Track width (mm)	Substrate resistance, Rs (Ω)	Standard deviation (Ω)
AR2.7	2	8.24	4.80
AR12	2	5.11	4.24
Control	n/a	49.0	42.3

5.3.2.3 Summary

Flexography has been used to print thin-film current collectors using a nanoparticle silver ink. The larger the anilox volume, used to print the current collectors, the better the performance of the cells. FFs of ~70% have been

achieved which outperforms those for similar cells reported in the literature although overall efficiencies are lower with the best at 1.7%. However, the active area of these cells is significantly higher than those presented in the literature.

5.3.3 Comparison of screen printed and flexographic printed DSCs

DSCs built with current collectors printed using screen and flexographic printing are compared. Firstly, geometric and electrical parameters and secondly, the cell parameters will be compared.

5.3.3.1 Comparison of current collectors

Table 5-10 shows geometric parameters for current collectors printed using screen and flexographic printing. The printed track widths are similar but the difference in cross-sectional areas and heights are very large. Figure 5-9 shows the normalized cross-sectional area (XSA) and current collectors flexographic printed using the AR12 anilox have a XSA which is 5% of the area of the screen printed and the AR2.7 anilox current collectors track XSA is just 1%. Average height shows a significant decrease of an order of magnitude from 9.1μm for screen printed tracks to 74nm and 44nm for AR12 and AR2.7 anilox respectively and the trend is the same for the peak heights. Flexographic printing can be considered a thin-film technology in comparison to screen printing and the amount of silver metal deposited therefore is considerably lower which represents potential savings in terms of materials used.

Table 5-10 Comparison of geometric parameters for current collectors printed using different methods

Printing method	Silver ink type	Track width (mm)	Printed track width (mm)	Cross-sectional area (mm^2)	Average height (mm)	Maximum height (mm)
Screen	Microparticle silver	2	2.15	2.0×10^{-8}	9.10×10^{-3}	1.24×10^{-2}
Flexography (AR2.7)	Nanoparticle silver	2	2.21	1.6×10^{-10}	7.42×10^{-5}	1.54×10^{-4}
Flexography (AR12)	Nanoparticle silver	2	2.37	1.0×10^{-9}	4.36×10^{-4}	9.05×10^{-4}

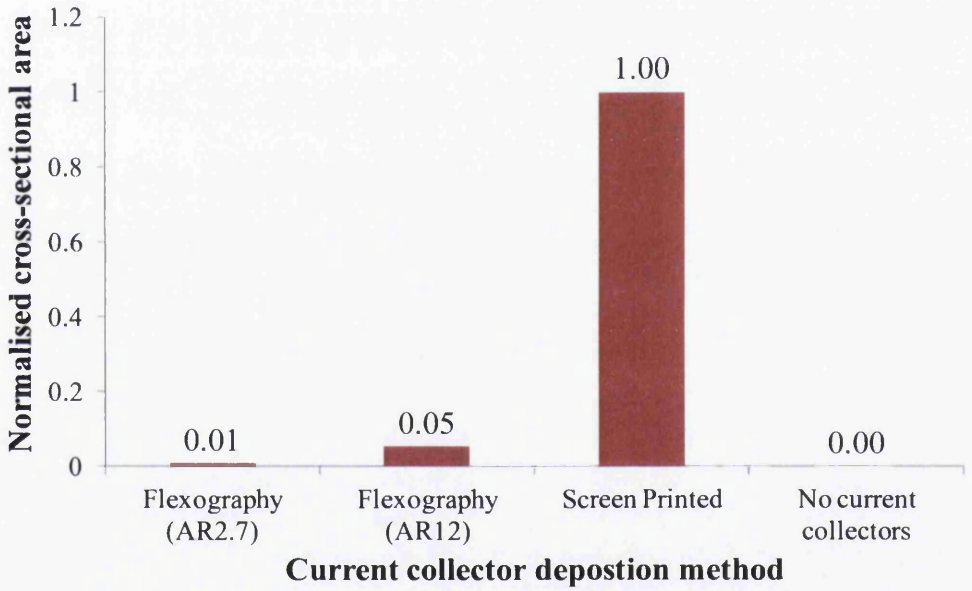

Figure 5-9 Comparison of normalized cross-sectional areas

Table 5-11 reports the measured electrical parameters for tracks printed using the different technologies. Oven process times were identical for each printing method but the oven temperature was lower for the nanoparticle silver ink as the ink was found not to require as great a temperature as the microparticle silver ink. Resistances of the screen printed tracks are an order of magnitude lower than those flexographic printed using the AR12 and two orders of magnitude lower

than tracks printed using the AR2.7 anilox. This difference is resistance between the printing methods is because of the significant difference in the printed geometry. The nanoparticle silver tracks exhibit lower resistivity's, compared to the microparticle silver ink, in spite of the difference in printed thickness. The reason for this is because of the particle sintering in the nanoparticle ink which eliminates contact resistance between particles whereas microparticle silver does not sinter.

Table 5-11 Comparison of electrical parameters for current collectors printed using different methods

Printing method	**Silver ink type**	**Oven process time (Minutes)**	**Oven temperature (°C)**	**Resistance (Ω)**	**Resistivity ratio to bulk silver**
Screen	Microparticle silver	10	150	0.02	6.10
Flexography (AR2.7)	Nanoparticle silver	10	130	2.41	4.97
Flexography (AR12)	Nanoparticle silver	10	130	0.36	4.66

5.3.3.2 Comparison of DSC performance

Figure 5-10 shows a comparison between the current voltage plots for DSCs with current collectors printed either by screen or flexographic printing and control cells built with no current collectors. Details of the cell parameters are given in Table 5-12.

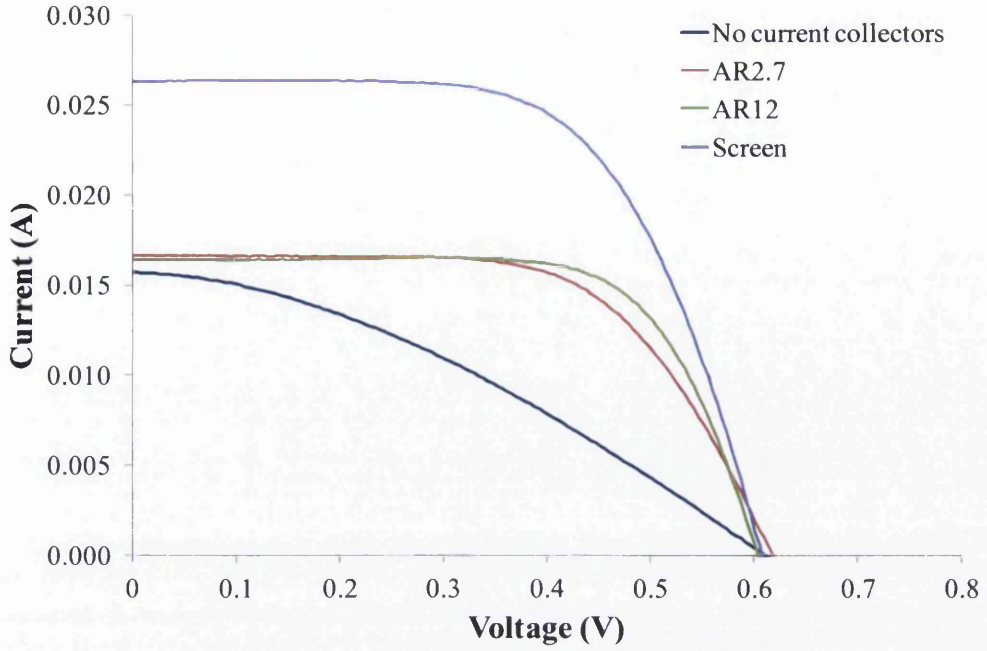

Figure 5-10 Current voltage responses obtained under illumination at 1 sun for DSCs produced with different counter electrode metallization methods. Current collector width is 2mm.

Table 5-12 Comparison of averaged cell parameters for DSCs with current collectors produced using screen and flexographic printing

Printing method for current collectors	**Voc (V)**	**Isc (mA)**	**Jsc (mA/cm^2)**	**Pmax (mW)**	**Fill Factor (%)**	**Efficiency (%)**
Screen	0.61	26.1	6.53	10.1	63.0	2.51
Flexography (AR2.7)	0.61	16.9	4.23	6.54	63.7	1.63
Flexography (AR12)	0.60	16.7	4.17	6.98	69.6	1.74
Control	0.61	16.0	3.99	3.62	37.8	0.91

The Voc value for all types of cells is fairly constant which indicates that the TiO_2 thickness is consistent. Cells with screen printed current collectors show the largest photocurrent with Isc values of 26.1mA. The reason for the difference in Isc for the flexographic printed current collectors has been previously discussed. The Pmax for cells with screen printed current collectors is also greater than those that were flexographic printed.

Figure 5-11 illustrates the difference in FFs between cells with differently deposited current collectors. The FFs for the cells with flexographic printed current collectors are higher than those deposited using screen printing. The standard deviation in the FF of cells with flexographic printed current collectors is lower than the cells with screen printed current collectors, which indicates that they are more consistent. A higher FF is indicative of lower energy losses in the cell.

A comparison between cell efficiencies is shown in Figure 5-12. Cells with screen printed current collectors have a higher efficiency than ones with flexographic printed current collectors with the best efficiencies of 2.5% and 1.7% achieved respectively. The drop in cell efficiency for the AR12 printed tracks compared to the screen printed tracks is ~31% and ~35% for the AR2.7 cells. There is more variability in efficiency for the cells with flexographic printed current collectors than those with screen printed ones.

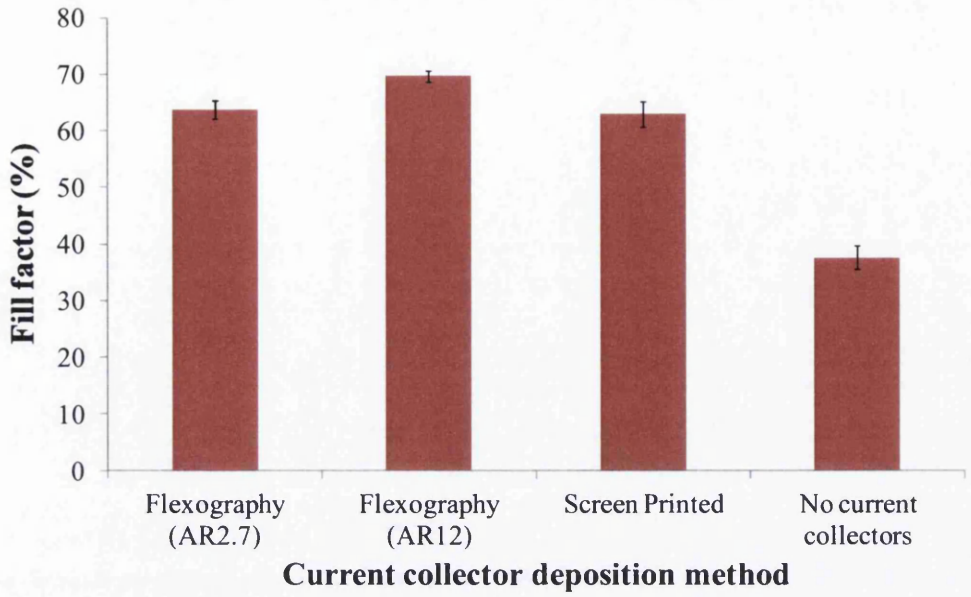

Figure 5-11 Comparison of current collector printing methods on DSC fill factor

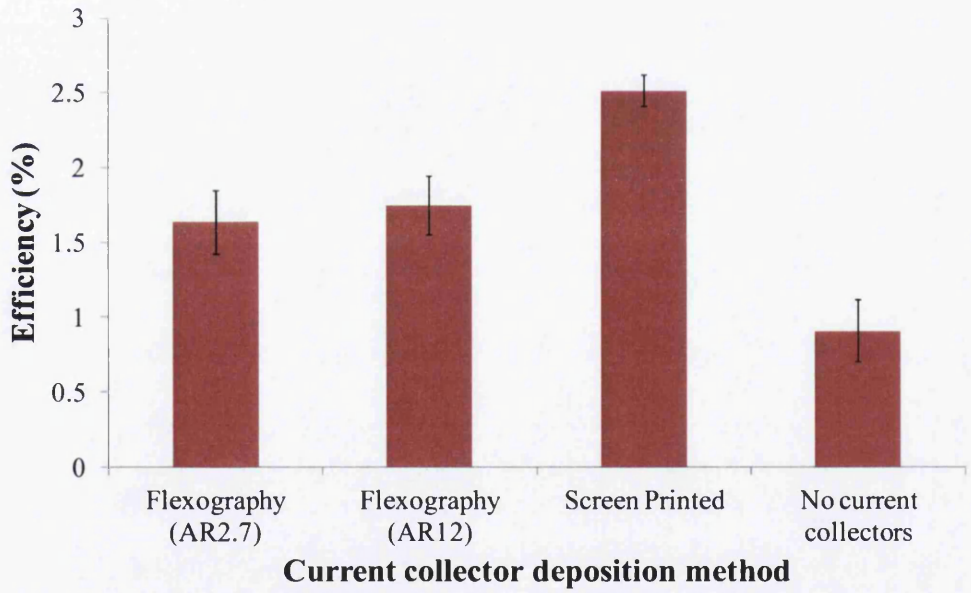

Figure 5-12 Comparison of current collector printing methods on DSC efficiency

5.3.3.3 Summary

In terms of efficiency and photocurrent cells with screen printed current collectors outperform their flexographic printed counterparts. Cells with flexographic printed current collectors show higher fill factors, with good consistency. In terms of the cross-sectional area of the printed tracks the amount of silver metal used for flexographic printed current collectors is <5.3% of the amounts of silver that screen printed current collectors do. In terms of the drop off in efficiency the cells with flexographic printed current collectors show an efficiency decrease of between 31-35%.

5.4 Conclusions

The drying times of a PTF microparticle silver ink which has been screen printed for use as a current collecting grid for DSCs have been found to have a large effect on the cell performance. An increase in drying time reduced resistance and resistivity of the printed track which reduced resistive losses in the cell improving the cell efficiency so that cells with current collectors dried at 150°C for 10 minutes resulted in cells with an average efficiency of 2.5%.

By using flexographic printing as an alternative to screen printing the deposited thickness of silver ink could be reduced by 95-99%. Anilox volume controls the volume of printed ink and current collectors printed with a larger anilox produced cells with higher performance, including FFs which are greater than any reported in the literature and which are very consistent with low variability.

When cells with current collectors printed with either screen or flexography are compared the overall efficiency and photocurrent of the cells are higher for screen printed current collectors but FFs are larger for cells with flexographic printed current collectors indicating that there are fewer energy losses in the flexographic cells. The reduction in efficiency for flexographic cells compared to screen printed cells is between 31-35%.

Flexographic printing offers an alternative method to screen printing for the deposition of current collectors for DSC application. Although an efficiency drop of 31% will occur, the deposited thickness of silver metal will be 95% less which offers a potential offset in performance through a reduction in cost of silver.

5.5 References

1. Okada, K., H. Matsui, T. Kawashima, T. Ezure, and N. Tanabe, *100 mm x 100 mm large-sized dye sensitized solar cells.* Journal of Photochemistry and Photobiology a-Chemistry, 2004. **164**(1-3): p. 193-198.
2. Philip, B., *Investigation of metal substrates for photovoltaic applications.* 2010, Swansea University.
3. Ju, M., Y.-J. Lee, J. Lee, B. Kim, K. Ryu, K. Choi, K. Song, K. Lee, C. Han, Y. Jo, and J. Yi, *Double screen printed metallization of crystalline silicon solar cells as low as 30 mu m metal line width for mass production.* Solar Energy Materials and Solar Cells. **100**: p. 204-208.
4. Ito, S., N.-L.C. Ha, G. Rothenberger, P. Liska, P. Comte, S.M. Zakeeruddin, P. Pechy, M.K. Nazeeruddin, and M. Graetzel, *High-efficiency (7.2%) flexible dye-sensitized solar cells with Ti-metal substrate for nanocrystalline-TiO2 photoanode.* Chemical Communications, 2006(38): p. 4004-4006.
5. Lindstrom, H., A. Holmberg, E. Magnusson, L. Malmqvist, and A. Hagfeldt, *A new method to make dye-sensitized nanocrystalline solar cells at room temperature.* Journal of Photochemistry and Photobiology a-Chemistry, 2001. **145**(1-2): p. 107-112.
6. Onoda, K., S. Ngamsinlapasathian, T. Fujieda, and S. Yoshikawa, *The superiority of Ti plate as the substrate of dye-sensitized solar cells.* Solar Energy Materials and Solar Cells, 2007. **91**(13): p. 1176-1181.
7. Han, L., N. Koide, Y. Chiba, A. Islam, and T. Mitate, *Modeling of an equivalent circuit for dye-sensitized solar cells: improvement of efficiency of dye-sensitized solar cells by reducing internal resistance.* Comptes Rendus Chimie, 2006. **9**(5â€“6): p. 645-651.
8. Kalyanasundaram, K., *Dye-sensitized Solar Cells*. 2009: Taylor & Francis.

6 Near infrared processing of conductive inks

6.1 Introduction

The ink processing time greatly inhibits the potential for high volume manufacturing. The most successful method at present is photonic flash sintering, or intense pulsed light (IPL) [1]. This has been proven to be a very rapid (microseconds) sintering process. The mechanism behind IPL sintering is that the nanoparticles themselves absorb the incident radiation at the particle surface plasmon resonance, which drives the sintering through thermal conduction. The first pulse sinters the top layer, forming a highly conductive skin, and subsequent pulses are absorbed by the top layer and the energy thermally conducts through the film. However, the fact that the ink film must be dried beforehand, plus the energy demands for running the xenon-arc flash lamps and potential issues with sintering thick films due to insufficient penetration of the radiation are limiting factors. When combined with microwave sintering and used as a pre-sintering drying step it took a minimum of 10 seconds to evaporate the solvent [2]. Ten seconds is still too long for a web moving at 100m/min as that is still an effective oven length of 60 meters.

Infrared methods allowed the ink deposit to be processed from wet. The ink vehicle absorbs the radiation which then facilitates particle sintering. This provides a method which is more beneficial to R2R processing. Current methods use mid and far IR (peak intensities of >4μm). In this chapter another part of the electromagnetic spectrum, near infrared (NIR) radiation is investigated as a method for rapidly drying a PTF silver ink and drying and sintering a nanoparticle silver conducting ink, both on a polymer substrate.

The NIR region of the electromagnetic spectrum is situated between the visible and the infrared in a wavelength range of 700nm to 2500nm with a peak wavelength at approximately 1000nm where typically polymer compounds do not have a strong absorbance (Cf. Figure 3-5). By contrast NIR heats metals very

effectively [3, 4] and unlike magnetic induction, heating works for a wide range of metals. Hence it is finding use for heating strip steel and galvanized steel for curing paints in roll to roll coating of metals [5, 6] at speeds up to 200m min^{-1} and as a consequence significantly reducing the footprint of the coating line, reducing capital costs [7]. Another significant potential industrial application for NIR has been for the rapid sintering of titania particles on steel and titanium surfaces for Dye-sensitized Solar Cells (DSCs) [8]. NIR has reduced the sintering time of the titania film from 30 minutes to 20 seconds and producing finished DSCs with equivalent performances.

In this chapter NIR radiation will be evaluated as a means of speeding up the drying and/or sintering process for conductive inks by implementing a single-step process without an additional pre-drying step. This will be investigated for a PTF silver ink, where the aim will be to remove the solvent rapidly to create a conductive film, and a nanoparticle silver ink. Resistances of NIR processed samples will be compared to samples dried and sintered using a conventional IR emitter and also in a hot air oven to see if the process time for drying and sintering could be reduced to help facilitate high volume printing production for printed electronic application.

6.2 Experimental

6.2.1 Materials

Two types of conductive inks were used: PTF microparticle silver and nanoparticle silver.

The PTF microparticle silver ink (Parelec, Parmod VLT DYA-100) contains a mixture of silver flakes (Diameter <10μm, 70wt%) in dipropylene glycol monomethyl ether solvent.

The nanoparticle silver ink used (InkTec, TEC-PR-030) was chosen because it was a commercially available ink which had been shown in previous work to

give excellent conductivity. Reflectance spectra of the wet and dry ink films were measured using a UV/VIS/NIR spectrometer (Perkin Elmer Lambda 750S).

The substrate used was a PET polymer film (Melinex ST505 175μm from DuPont Teijin Films). It was chosen because it is heat stabilized up to 150°C, which is the minimum process temperature for the PTF ink and higher than the temperature required for silver nanoparticle inks. The transmission spectra of the substrate was measured using a UV/VIS/NIR spectrometer (Perkin Elmer Lambda 750S).

6.2.2 Method

6.2.2.1 PTF silver ink

Tracks (1mm x 30mm) were screen printed using a DEK 248 semi-automatic screen printer (see chapter 3). The screen used was a 77T mesh.

The ink was processed in two ways: Firstly, a single step drying process was tried where the sample with as printed wet ink was exposed to NIR without pre-drying. Secondly, a two-step hybrid process was used where the printed samples were dried in an oven at 150°C for 2, 5 and 10 minutes before being exposed to NIR. The dwell times under the NIR lamps were between 2 – 20 seconds and chosen to test the samples without damaging either the ink film or the substrate. Control samples which were not exposed to NIR were also measured. These times were chosen to see if the NIR would have any effect in improving the electrical performance and reduce the overall process time.

Resistance was measured using a four-point probe (Keithley Sourcemeter). Cross-sectional area of the tracks was measured using white light interferometry so that the volume resistivity could be calculated.

6.2.2.2 Nanoparticle silver ink

Samples were prepared by bar coating (see section 3.2.1), which was used because the work was carried out away from the university laboratories and a simple, reproducible deposition was required. A strip (30mm x 80mm) of nanoparticle silver ink was deposited onto PET substrate resulting in a dry film thickness of 3.3μm (±0.3μm), measured using white light interferometry. The coating process was used because at the time of these experiments the NIR equipment was not available at the university and a fast, reproducible method was needed to produce a large area coating.

The ink was processed using three methods; hot-air oven (Heraeus Vacutherm), IR lamps (SC Driers UV/IR/Convection combination belt furnace) and six HB-NIR near-infrared emitters (Adphos NIR/IR Coil lab LV2). The power output of the IR and NIR lamps were adjusted to prevent damage to the PET substrate. Over exposure to heat can cause undesirable buckling of the PET film rendering it unusable.

For conventional hot air oven testing samples were dried and sintered at atmospheric pressure at 140°C for different times ranging between 30 and 900 seconds. For IR heat treatment samples were placed onto the belt, set at different speeds, and passed through the furnace once giving heating times between 17 and 84 seconds. NIR heating was achieved by moving the sample to be heated at a set speed, determined by the operator, under the emitters at a pre-set but variable power level. Altering the speed of the sample holder allowed the time of NIR exposure to the sample to be varied between 1.4 and 2.1 seconds.

It should be noted that the nanoparticle silver ink was processed, in all three methods, from wet with no pre-drying step; unlike photonic sintering methods which require the ink to be dry.

The sheet resistance of each sample was measured using a four-point probe (Keithley Sourcemeter).

6.3 Results and Discussion

6.3.1 NIR processing of a PTF silver ink

The first experiments focused on trying to process the PTF ink in a single drying step to remove the bulk solvent and leave a conducting ink film. It was found that under no conditions could the ink be processed from wet. Either the ink was still wet on exit from under the lamps or the solvent boiled and created a pitted ink film, see Figure 6-1. The decision was taken to abandon a single step approach and pre-dry the ink before exposing the samples to NIR.

Figure 6-1 Image of the PTF ink after exposure to NIR from wet

Figure 6-2 shows the effect of NIR exposure on the resistance of PTF with different pre-drying times. Samples dried for 5 and 10 minutes exhibit little change in resistance upon NIR exposure. This is probably because the ink film is dried and the prolonged time in the oven has allowed the organometallic silver compound to decompose, forming the nanoparticles which 'weld' the larger particles. The samples dried for 2 minutes do show a marked change in resistance with respect to dwell time under the NIR but the final resistance is still higher than that of the samples dried for longer. It is worth noting that samples dried for 10 minutes would not take exposure times greater than 15 seconds. A dwell time of 20 seconds proved to be the limit of the substrate under NIR exposure. Samples above 20 seconds were damaged with the substrate deformed.

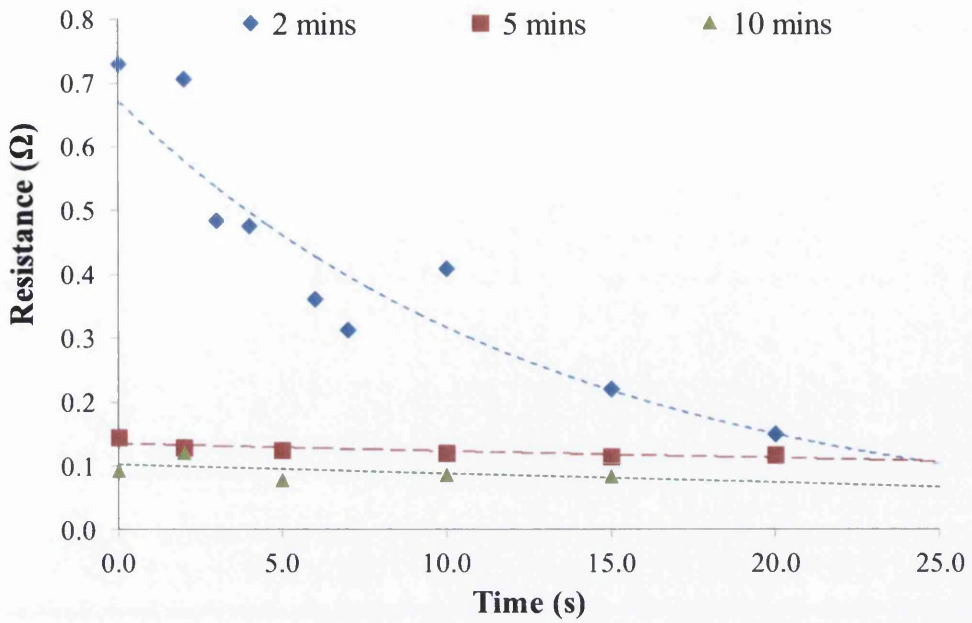

Figure 6-2 Effect of NIR exposure time on resistance for 1.0mm wide screen printed PTF silver ink pre-dried at 150°C for different times

How well the ink performed is shown in Figure 6-3 where resistivity is presented as a ratio to bulk silver. During scoping trials the best resistivity was achieved at a drying temperature of 150°C for 20 minutes. The best performing sample was 9.8 times bulk after a pre-drying time of 10 minutes. There is no benefit in using NIR after pre-drying for 5 and 10 minutes. A drying time of 2 minutes followed by an exposure to NIR for 20 seconds shows a marked reduction in performance from the control sample; from ~45 to ~10 times bulk silver. However, at a dwell time of 20 seconds the substrate was at its extreme limits of being thermally damaged.

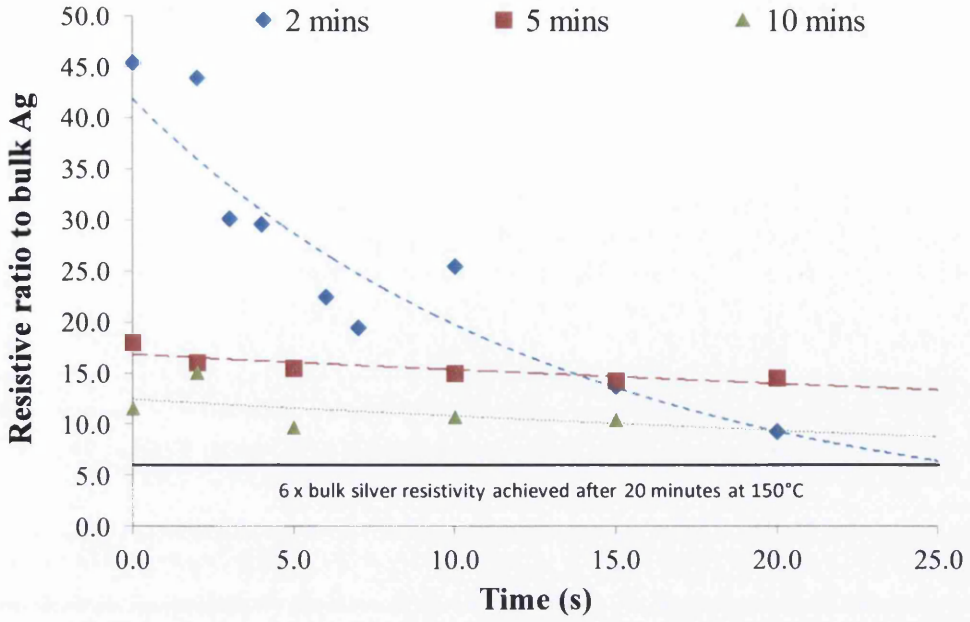

Figure 6-3 Resistive ratio to bulk silver verses NIR exposure time

Samples dried for 2 minutes show a significant reduction in resistance but the best resistivity is achieved close to the critical point where damage is likely to occur and the resistivity achieved is still greater than could be achieved by thermal heating for 20 minutes. On alternative substrates, such as glass, using NIR to reduce the process time maybe an option where temperature is not an issue with regards to causing substrate damage. On a polymer film such as PET (even heat stabilized) it is not feasible.

6.3.2 Nanoparticle silver ink

Figure 6-4 shows a comparison of sheet resistance values following heat treatment between the three drying processes; hot-air oven at 140°C, IR and NIR. A logarithmic scale had to be used to display the process time due to the large range of times between the methods to get good conductivity.

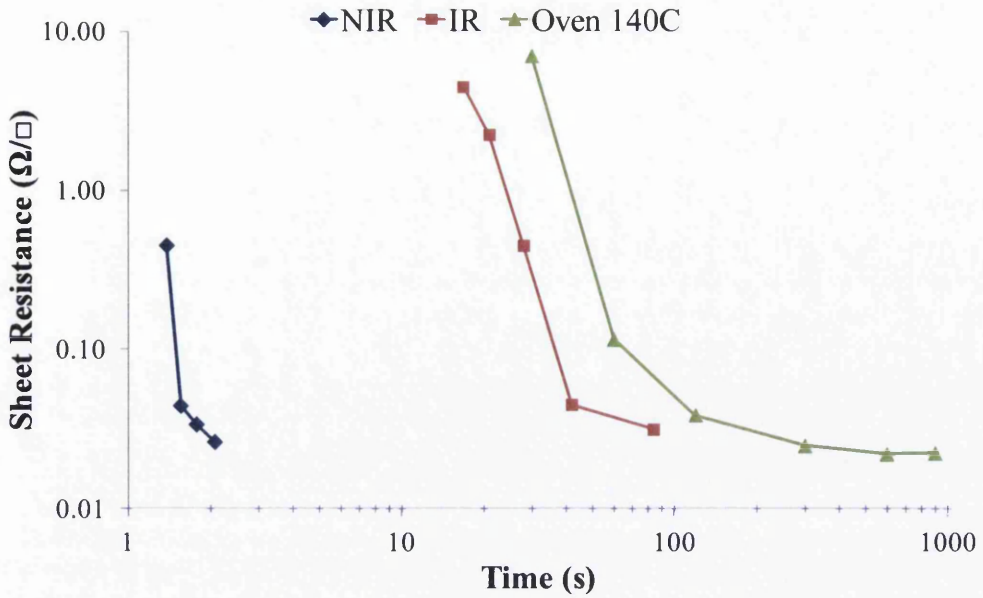

Figure 6-4 Sheet resistance verses dwell time for the three different heating methods (Axes reported in logarithmic scale)

The three heating methods shown are all capable of achieving the low sheet resistances (typically below 0.035 Ω/□). NIR sintering took 2 seconds to fully sinter the nanoparticle silver ink to a sheet resistance of 0.026Ω/□. Comparative results from the IR sinter took 84 seconds to achieve a sheet resistance of 0.032Ω/□ and the oven at 140°C took 600 seconds to record a sheet resistance of 0.022Ω/□. The sheet resistivity (presented as the resistive ratio to bulk silver) for the sheet resistance results are also presented in Table 6-1. Sintering the nanoparticle ink in the oven produced the best results and consequently resulted in a sheet resistivity with a ratio of 4.57 times that of bulk silver. The NIR sintered ink film was comparatively 5.41 times bulk silver.

Table 6-1 Comparison between best performing sheet resistance and process time

Method	Sheet Resistance (Ω/□)	Resistive ratio to bulk silver	Time (s)
Oven (140°C)	0.022 ± 0.0010	4.57	600
IR	0.032 ± 0.0013	6.65	84
NIR	0.026 ± 0.0029	5.41	2.1

The NIR method is a far more rapid method than mid-IR and a conventional hot air convection oven. This reflects the way in which the ink vehicle rapidly absorbs the NIR energy, burning off the organic components and dissipates the thermal energy to the particles which rapidly heat and sinter together at the same time.

Figure 6-5 compares the UV/VIS/NIR reflectance spectrum of the nanoparticle silver ink. In a wet state the ink appears to readily absorb in the NIR region, reflecting ~12% of the NIR radiation. In a dry state the reflectance of the ink is increased to ~70% in the visible region and ~45% in the NIR. Energy absorbed should therefore be by the ink vehicle which will transfer the energy to the particles. Heat, induced by the absorption of the NIR radiation, causes the organic components and solvents to evaporate. Energy absorbed by the silver particles induces the sintering at the edges leading to the formation of a continuous metallic layer. As the particles sinter together they reflect more of the radiation (since it turns from a dark green nanoparticle containing coating to a one more like a thin film of silver metal). This absorption of NIR energy is critical to the success of the method since it will directly heat the ink vehicle, evaporating the organic components and through heat transfer rapidly heat the silver particles to facilitate sintering. This means that the process can be single step from an as printed wet film to a fully sintered one.

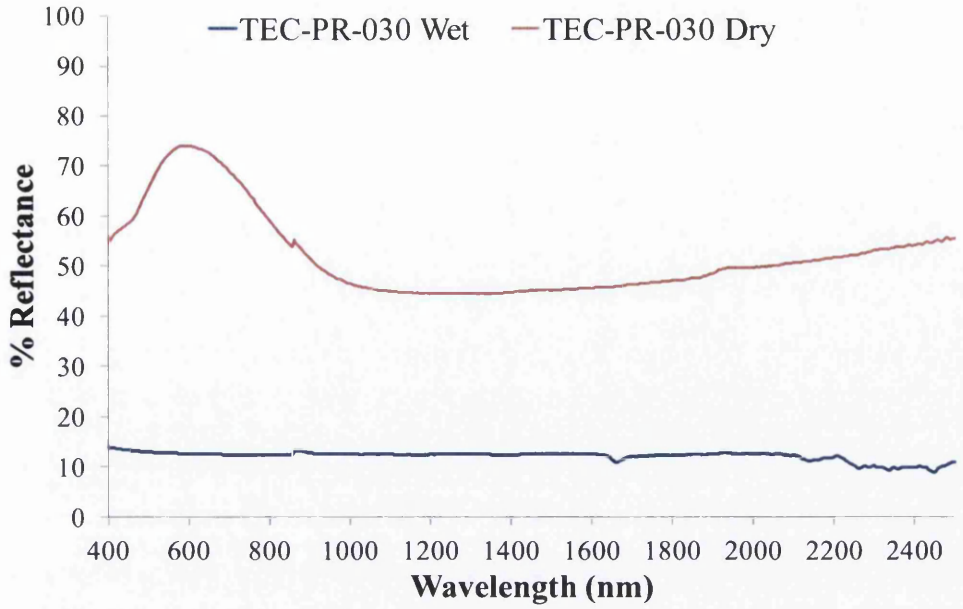

Figure 6-5 UV/VIS/NIR Reflectance spectrum of the nanoparticle silver ink

The UV/VIS/NIR transmission spectrum of the PET substrate material (Figure 6-6) shows an 90% transmission at 1000nm (Cf. the output wavelength maximum of the NIR lamps in table 2-2) but above 2200nm the transmittance drops below 70% and keeps falling as it moves into the long-wave IR. This suggests that NIR lamps will have a reduced effect of potentially charring and degrading the PET than the mid-IR lamps. The time of exposure of the substrate to NIR will be less than the time exposed to the mid-IR as the energy inputted is much greater and the peak energy density is around 1000nm where the substrate has a high transmittance, unlike the mid-IR whose peak energy density is >2200nm where most organic materials absorb strongly.

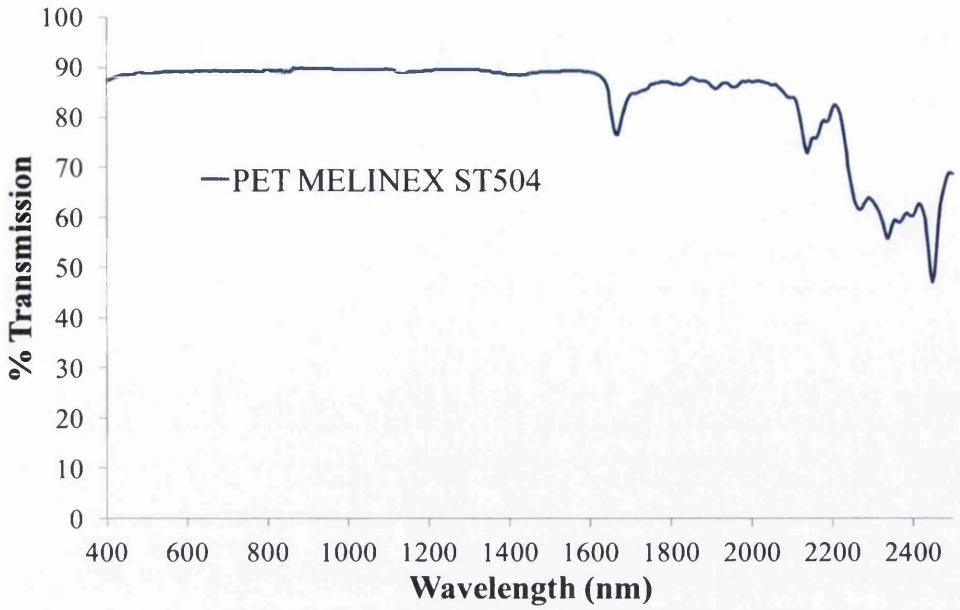

Figure 6-6 UV/VIS/NIR Transmittance spectra of a PET polymer film substrate

In chapter 3 the theoretical peak energy density of a black body NIR emitter was given 1000nm and has also been empirically measured to be at ~1000nm (Cf. section 3.3.3). Since the PET has a 90% transmittance, it should allow the ink to be dried and sintered without causing damage to the substrate. Possible damage to the substrate from heat transfer from the ink was mitigated in two ways. Firstly the rapid nature of the process is such that the heating phase is significantly shorter than IR and hot air treatment with a maximum exposure of just over 2 seconds. A second feature is that a modified sample stage, using a PTFE block, was used instead of the standard metal framed unit to avoid damage from the steel frame of the substrate holder, which heats up rapidly during NIR irradiation which would otherwise lead to thermal damage to the PET, which starts to degrade above 160°C.

6.4 Closure

The data presented demonstrated that NIR shows little benefit for use as a means of decreasing the process time for a PTF silver ink but has the potential to be employed as a method for rapidly drying and sintering a nanoparticle silver ink in a single step process.

NIR has been found to be unsuitable for drying a PTF silver ink in a single step process as solvent boil causes defects in the ink film. By employing a pre-drying step and then exposing the dried ink film to NIR a fast drying time coupled with a long NIR exposure (~20s) does show a reduction in resistance. However, the resulting resistivity is double that which can be achieved by using a longer time in an oven, plus the NIR exposure time is at the limits for causing damage to the substrate, meaning that there is little benefit to using NIR.

For a nanoparticle silver conductive ink, NIR has been shown to rapidly dry and sinter a thick ink film giving comparable sheet resistance values to a mid-IR and hot air oven processes but in a timeframe of only 2 seconds, compared to 84 seconds for IR and 600 seconds for the hot air oven. This occurs since the NIR absorbance of the ink vehicle is strong and the silver particles are rapidly heated through heat transfer from the evaporating organic components. The PET substrate does not absorb the NIR peak energy as effectively and is undamaged. It is likely that this process time can be further reduced for a thinner film. The ability to dry and sinter a wet ink film, without a pre-drying step, in ~2 seconds is technologically a very important result. The fastest sintering technology which could be implemented in R2R manufacturing is IPL sintering, which can achieve a sintered ink film in a microsecond timescale, but only from a pre-dried ink film. Using IPL to dry a wet ink film has been shown to take at least 10 seconds [9]. To illustrate the specification for a roll to roll product at 100 meters per minute would require an oven of just over 3m in length for NIR, 140m for IR and an infeasible 1000m for the conventional oven with associated capital costs to be considered.

6.5 References

1. http://www.novacentrix.com/ 8th March 2011
2. Perelaer, J., R. Jani, M. Grouchko, A. Kamyshny, S. Magdassi, and U.S. Schubert, *Plasma and microwave flash sintering of a tailored silver nanoparticle ink, yielding 60% bulk conductivity on cost-effective polymer foils.* Advanced Materials, 2012. **24**(29): p. 3993-8.
3. Vongsavat, V. and T.R. Lee, *COLL 191-Metal-metal nanoparticles that absorb strongly in the near infrared.* Abstracts of Papers of the American Chemical Society, 2008. **235**: p. 1.
4. Bauer, S., S. Bauer-Gogonea, W. Becker, R. Fettig, B. Ploss, W. Ruppel, and W. von MÃ¼nch, *Thin metal films as absorbers for infrared sensors.* Sensors and Actuators A: Physical, 1993. **37â€“38**(0): p. 497-501.
5. Mabbett, I., *Applications of near infrared heating to the coil coating industry*, in *College of Engineering. Materials Research Centre.* 2011, Swansea University.
6. Knischka, R., U. Lehmann, U. Stadler, M. Mamak, and J. Benkhoff, *Novel approaches in NIR curing technology.* Progress in Organic Coatings, 2009. **64**(2-3): p. 171-174.
7. Bär, K.K.O., *How to save energy costs with the NIR-technology in coil coating processes.* Steel Grips 4, 2006. **3**: p. 225-228.
8. Watson, T., I. Mabbett, H. Wang, L. Peter, and D. Worsley, *Ultrafast near infrared sintering of TiO_2 layers on metal substrates for dye sensitized solar cells.* 2010.
9. Perelaer, J., M. Klokkenburg, C.E. Hendriks, and U.S. Schubert, *Microwave Flash Sintering of Inkjet-Printed Silver Tracks on Polymer Substrates.* Advanced Materials, 2009. **21**(47): p. 4830-+.

7 Near infrared radiation sintering characteristics of a nanoparticle silver ink applied by the flexographic printing process

7.1 Introduction

In Chapter 6, Near infrared (NIR) radiation was shown, to be an applicable method for facilitating the rapid drying and sintering of a nanoparticle silver conducting ink to a resistivity of ~5x bulk silver in 2 seconds for a large area thick ink film (~3μm) coating.

This chapter will take the process a step further and apply the NIR drying and sintering to the flexographic printing process. Tracks of varying widths will be printed using a flexographic printability tester and dried and sintered using NIR radiation. Emitter power will be varied to assess how the ink performs under different sintering conditions. The electrical performance of the nanoparticle silver ink can be measured and the uniformity of the sintering can be determined by observing the volume resistivity as this should be a constant figure for each set of samples for different emitter powers. Changing the anilox roll will subsequently allow the effect of changing the deposit thickness during the NIR sintering process and see if changing the volume of ink printed affects the electrical performance.

7.2 Experimental

7.2.1 Materials

Nanoparticle silver ink was used (InkTec, TEC-PR-030) as for work in Chapter 6. The substrate used was a PET polymer film (Melinex ST505 175μm from

DuPont Teijin Films). The transmission spectrum for the substrate is reported in chapter 6.

7.2.2 Flexographic printing

Samples were printed using an IGT F1 flexographic printability tester. Two different volume anilox rolls were used; $8cm^3m^{-2}$ and $24cm^3m^{-2}$ and referred to as AR8 and AR24 respectively. Anilox specifications are given in chapter 4. Printing speed of $0.4ms^{-1}$ ($25m\ min^{-1}$) was used with an anilox-to-plate force of 50N and a printing force of 50N. These conditions were chosen as they produced the best visual print. Five prints per sample set were produced. Figure 7-1 shows the plate image which was designed so tracks of different widths could be evaluated for resistance and volume resistivity. Widths; 0.1mm, 0.2mm, 0.3mm, 0.5mm, 1.0mm were investigated.

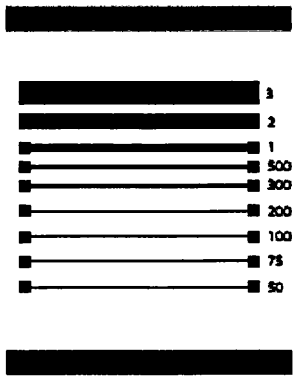

Figure 7-1 Flexographic plate design

7.2.3 NIR operation

The NIR unit and its operation are described in section 3.3.3. Before printing the NIR emitters of the Adphos NIR/IR Coil lab LV2 unit were warmed up by running the unit which was set to the desired power. Immediately after printing samples were transferred onto the PTFE sample holder and secured at the top and

bottom edges with 3M scotch tape. The sample was then transferred to the sample holder of the NIR unit and exposed to the NIR emitters for a 1 second exposure time at 25 m/min. This speed and time was chosen to compliment the printing. After exiting the emitter housing the sample was removed from the NIR unit and wrapped in aluminium foil which was sealed at each end. This helped prevent the evaporation of any organic material which may have been left in the ink to prevent the possibility of further sintering as room temperature sintering of nanoparticle films was reported in chapter 2.

7.2.4 Sample analysis

The methodology for analysis of printed tracks is presented in chapter 4. Electrical resistance was measured using the four-point probe method (Keithley 2400 sourcemeter). Resistivity of the tracks was calculated from the resistance and the cross sectional area as described in section 3.5. Scanning electron microscopy (Hitachi S-4800) was used to take images of the ink microstructure at a magnification of 100 000x.

7.3 Results and discussion

The results are presented in three separate sections: The first looks at the effect of emitter power on electrical performance and microstructure for 1mm wide lines printed using the AR8 anilox. The second contains an investigation of how different track widths printed using the AR8 anilox perform. The third looks at the effects of increasing the anilox roll volume to change the thickness of the ink deposit on electrical performance after NIR processing.

7.3.1 Effect of emitter power on resistance

Figure 7-2 shows the effect of NIR emitter power on the resistance for a 1mm printed track, using the AR8 anilox, exposed to NIR radiation for 1 second. Data for resistance at different emitter powers along with the modeled peak spectral

emittance (chapter 3) of the emitters at peak wavelength is given in Table 7-1. All samples were dry on exit from the NIR unit, with samples at higher emitter powers (≥50%) appearing more shiny in appearance, whereas samples at lower emitter powers (40-45%) had a yellow/green tint. Resistance and resistivity are shown to decrease with increasing emitter power, with the lowest resistance at 55% power where a resistivity of 5 times bulk is achieved.

The standard deviation in the resistance decreases with increasing emitter power. With higher power, a more complete and sintered ink film is achieved with less defect areas. At lower emitter powers, particle sintering is incomplete, causing localized voids between particles resulting in higher resistance (Figure 7-3).

Scanning electron microscope images of the ink after NIR processing at different emitter powers are shown in Figure 7-3. The air dried sample (a) shows that no particle sintering had occurred, with individual particles of ~30nm diameter visible. Electrical resistance was higher due to the large contact resistance between particles. When the ink film is processed using NIR at 40% emitter power (b) the ink film shows evidence of particle sintering with larger clusters of silver particles, where particles have started to coalesce. The electrical resistance is still high (see Table 7-1) with the flow of current impeded by the contact resistance between the particles. A fully sintered ink film (c) is achieved when the NIR emitter power is increased to 55%. The silver particles have sintered together to form a continuous metallic film with no contact resistance between particles and few void spaces, as described in in Chapter 2. As a result the ink film behaves as a metal film and resistance of the ink film is minimal.

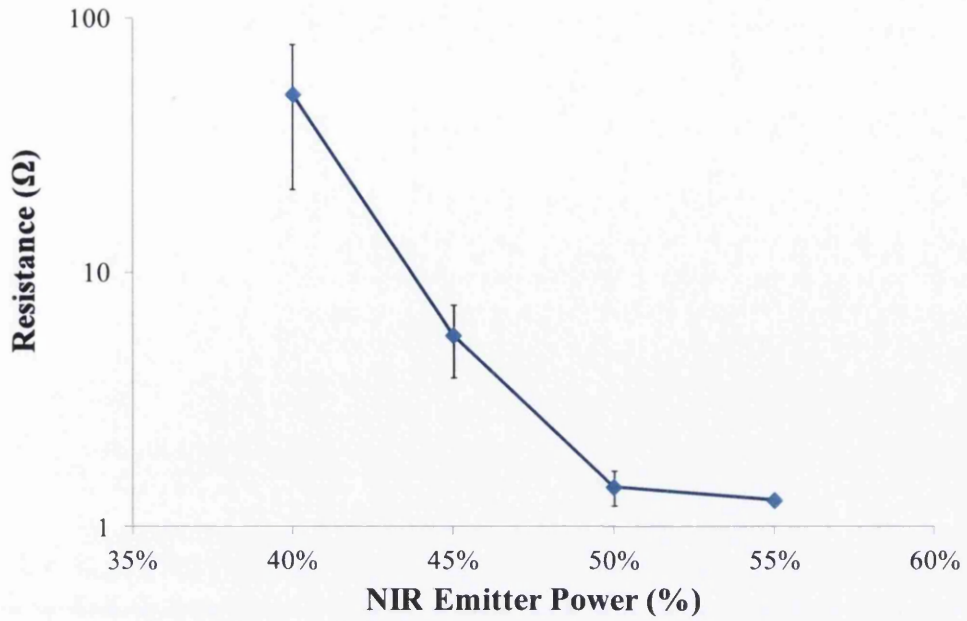

Figure 7-2 Effect of NIR emitter power on resistance for a 1mm wide track printed with the AR8 anilox roll for a dwell time of 1 second (Resistance is reported using a logarithmic scale)

Table 7-1 Resistance data and emitter output for NIR processed 1mm wide tracks

NIR Emitter Power (%)	Modeled spectral emittance at λ_{max} ($\mu Wcm^{-2}nm^{-1}$)	Resistance (Ω)	Resistivity (Ω.m)	Resistivity as a ratio to bulk Ag
40	2467.16	50.1 ±28.9	3.12e-6	196
45	3069.28	5.66 ±1.81	3.52e-7	22.2
50	3706.70	1.44 ±0.22	8.94e-8	5.63
55	4445.90	1.27 ±0.06	7.92e-8	4.99

a)

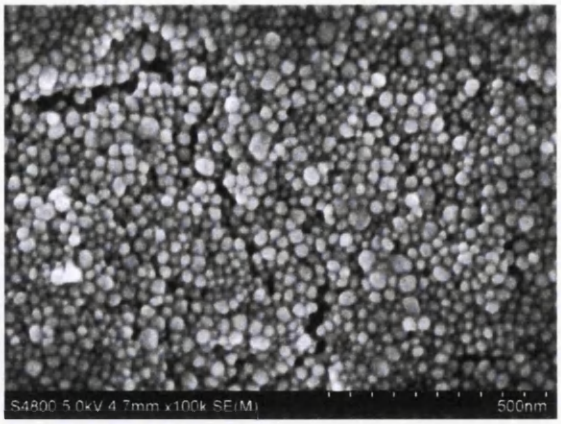

b)

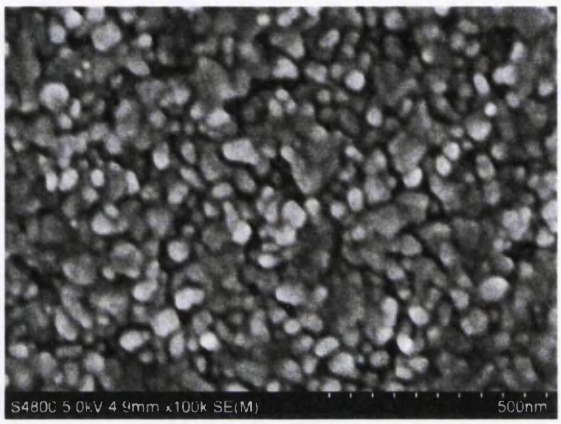

c)

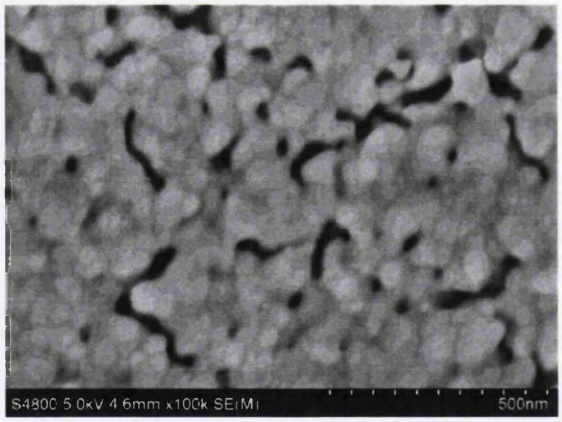

Figure 7-3 SEM images at 100k x magnification of flexographic printed nanoparticle silver ink which have been processed using different methods: a) allowed to dry in air, b) NIR processed at 40% emitter power, c) NIR processed at 55% emitter power

Figure 7-4 shows the effect of emitter power on resistance for flexographic printed tracks of different track widths. Tracks are shown to reach the lowest resistance at the largest emitter power (55%). When the emitter power is reduced to less than 55% the resistance increases, as previously observed, but narrower track widths (<0.5mm) show a large variance in their resistance, particularly between 40% and 45% power. The effect of track width on the NIR sintering performance will be discussed in the next section. In summary, the emitter power is an important factor to consider when setting up an NIR drier and there is a critical emitter power required to ensure that sintering has occurred. Increasing the emitter power increases the amount of energy available to be transferred into the ink system.

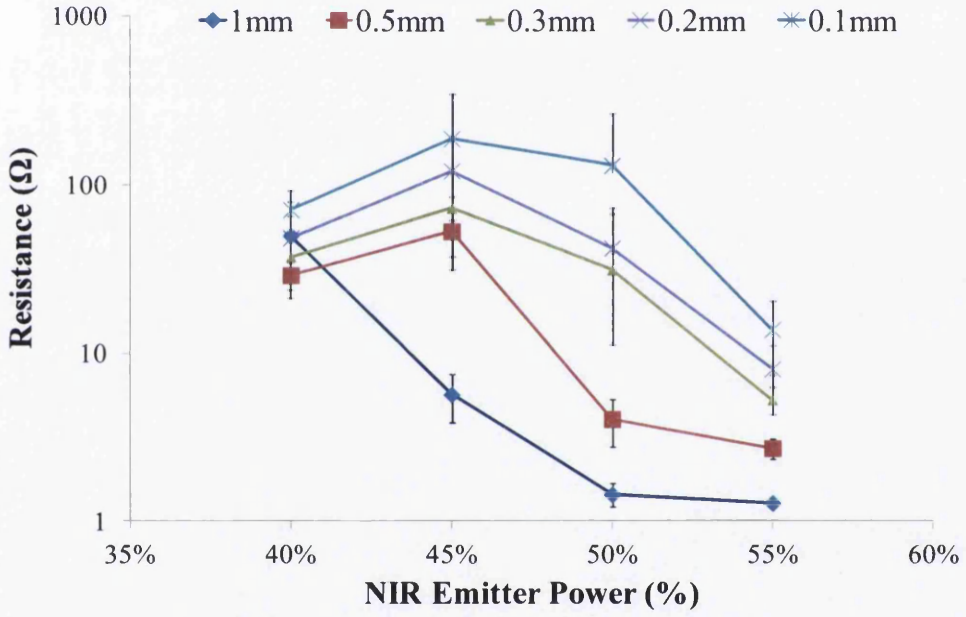

Figure 7-4 Effect of NIR emitter power on resistance for different line widths (Line widths are nominal values, anilox volume is AR8)

7.3.2 Effect of track width on electrical performance

It was observed during the experiment that during the time taken to transfer the printed samples, from the substrate holder of the printer to the sample holder of the NIR unit that some drying of the thinner track widths was occurring. In

chapter 6 a dried ink film was shown to have a higher reflectance than a wet ink film. Therefore this drying observed in the thinner tracks will increase the reflectance reducing the absorbance, which would result in less of the NIR radiation being absorbed.

Figure 7-5 shows the effect of track width on the resistivity, for NIR processed flexographic printed tracks using the AR8 anilox. The decrease in track width results in an increase in the resistivity for samples processed at 55%, 50% and 45%. The exception is for tracks which were processed using an emitter power of 40%, where the resistivity increases with width. The variation in the resistance at emitter powers below 55% for the thinner tracks could be explained because of the variability in the time taken to remove the printed samples from the IGT F1, attach them to the sample holder and process them through the NIR unit; the longer the transfer time, the greater the evaporation of the solvent in the ink vehicle which, as already determined in Chapter 6, is crucial to the mechanism of NIR sintering. At 40% emitter power it is possible that the 1.0mm wide tracks have an unusually large resistance because the top of the ink layer has dried quickly, forming a skin which traps the organics in the ink system underneath, preventing the sintering process from occurring.

If the best performing samples which were processed at 55% emitter power are evaluated (see Figure 7-6) the increase in resistivity with respects to track width is clear. Resistivity is a material property and it would be expected that all track widths dried and sintered at a specific emitter power should exhibit the same value. Volume resistivity is directly related to resistance and area (equation 3-2). The change in resistance with track width, for samples processed at 55%, is proportional and the cross-sectional area of flexographic printed tracks has been shown, in chapter 4, to increase linearly with respect to width.

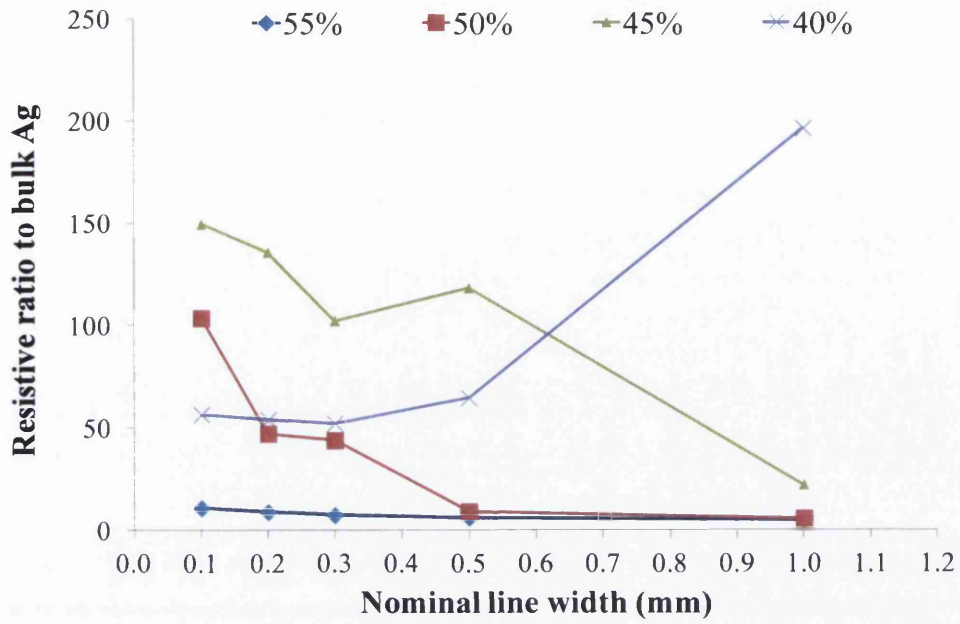

Figure 7-5 Nominal line width verses resistivity as a ratio to bulk silver for anilox AR8

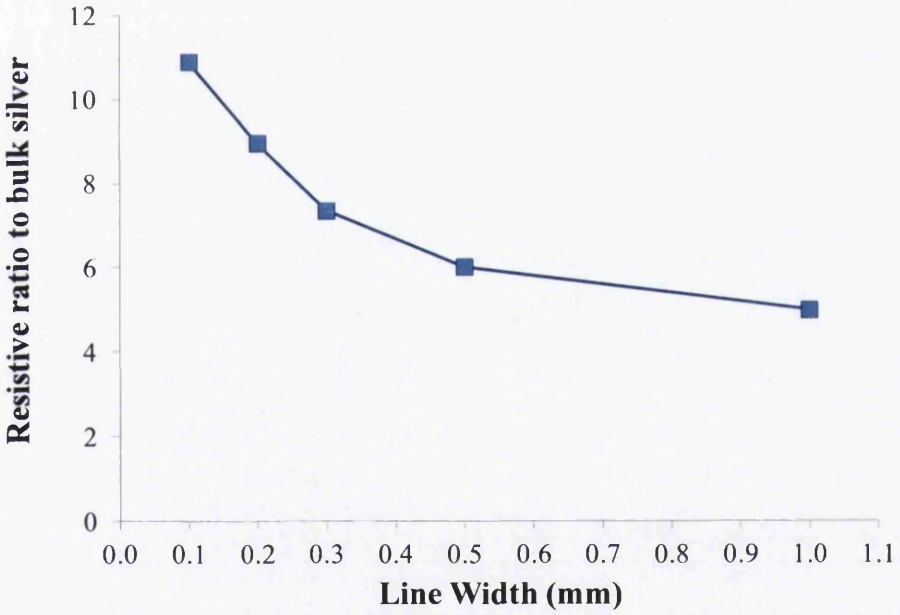

Figure 7-6 Nominal line width verses volume resistivity for tracks printed using AR8 and sintered at 55% emitter power for 1s

Figure 7-7 shows the change in the ratio of the exposed perimeter of the track to the cross-sectional area. The ratio is similar for 1.0mm and 0.5mm track width but for the smaller tracks the ratio increases. The solvent evaporation will be greater for thinner tracks as the proportion of exposed surface is greater. The thinner tracks should absorb proportionally more NIR radiation than wider tracks. The increase in resistivity with decreasing line width therefore can be associated to the increased drying before exposure to NIR. If the experiment was carried out in a R2R process, with samples transferred straight under the NIR emitters after printing, then solvent evaporation for the thinner tracks may not be observed.

For the samples processed at 40% emitter power, where resistivity increases with line width, the SEM image (Figure 7-3 (b)) showed that particles had begun to coalesce but there were many void spaces between particles impeding the flow of current. It is possible that the emitter power was too low to provide enough energy to remove all the organic components but instead allowed a skin of dried ink to form at the surface, making the ink appear dry. It is known that nanoparticles will sinter at room temperature and before measuring the track resistance room temperature particle sintering could have occurred. With less organic components to be evaporated in the smaller tracks the sintering process would be more rapid than for the wider tracks. At higher emitter powers the organic components will have been removed and greater particle sintering will have occurred resulting in larger particles so subsequent sintering is less energetically favorable.

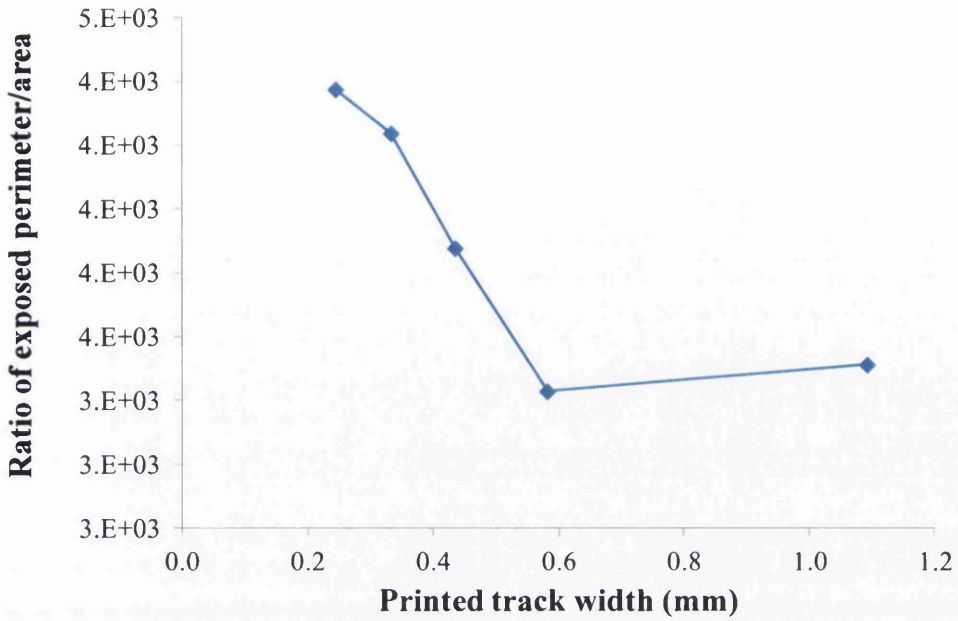

Figure 7-7 Ratio of the exposed perimeter/cross-sectional area at different printed track widths

7.3.3 Effect of anilox volume on electrical performance

Changing the volume of the anilox roll will change the volume of ink transferred during the printing process (c.f. chapter 4). Here, a comparison of the electrical performance, of NIR sintered tracks, for two different anilox rolls, the AR8 and the larger volume AR24 (anilox rolls are defined in Table 4-2) is presented. Geometric data for tracks printed using both anilox are in chapter 4.

Figure 7-8 compares the effect of NIR emitter power on resistance for 1.0mm wide tracks. Tracks printed using the AR24 anilox result in lower resistances, than tracks printed using the AR8, because the deposit thickness is greater. The effect of increased emitter power to reduce the resistance shows the same trend for both anilox rolls. If the resistivity of the ink is evaluated (see Figure 7-9) the electrical performance of the ink is consistent for both anilox rolls at an emitter power of 55% and 50%. A further reduction in the emitter power leads to an increase in resistivity.

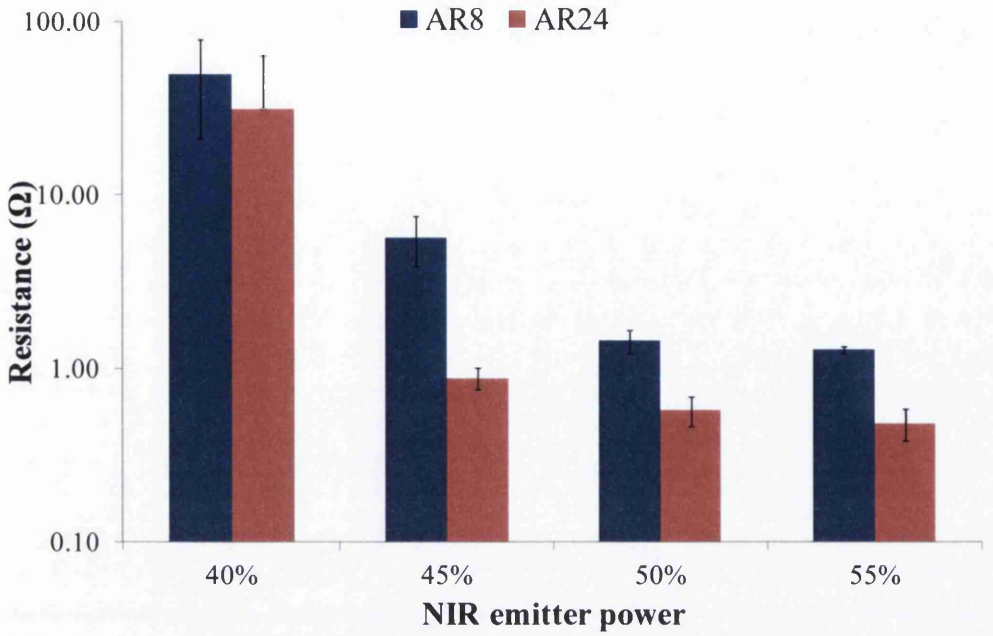

Figure 7-8 Effect of NIR emitter power on resistance for 1mm wide tracks deposited using two different anilox rolls

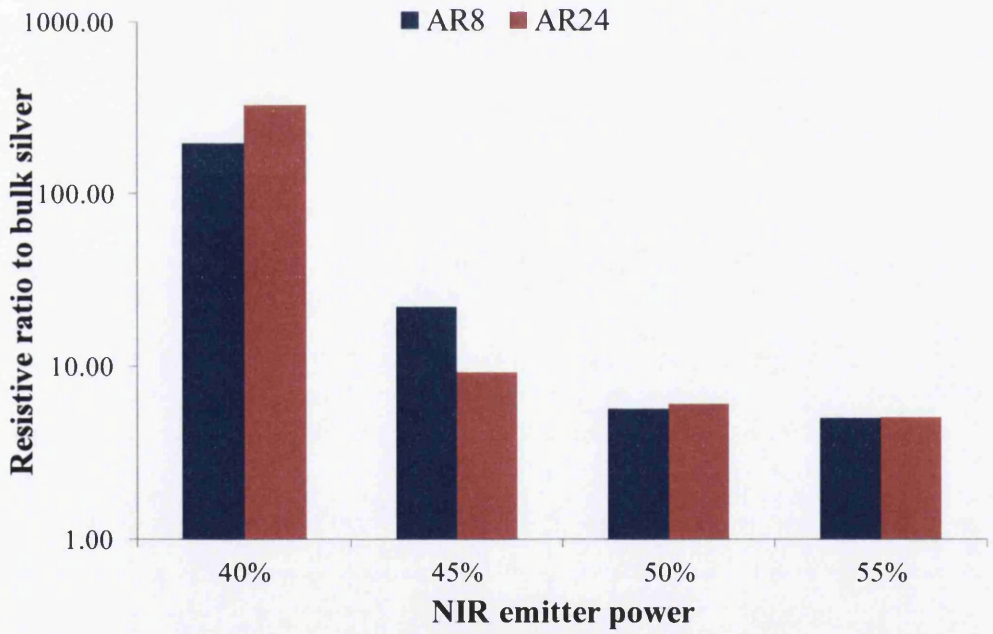

Figure 7-9 Effect of NIR emitter power on resistivity for 1mm wide tracks deposited using two different anilox rolls

For track widths printed using different anilox volumes and sintered at the highest emitter power (55%) the larger AR24 anilox shows the same trend as the AR8, with resistance increasing with decreasing track width (Figure 7-10). However, the tracks printed using the AR24 anilox show much lower resistances, especially for thinner tracks. The ratio of exposed perimeter to area is lower for tracks printed using the AR24 anilox (Figure 7-11) and the thicker deposit printed by the AR24 anilox means that there is a greater amount of organic components to evaporate so the drying rate should be slower meaning the drying observed with thinner track widths with the AR8 samples is less.

A reduced drying rate for smaller features is backed up in Figure 7-12. The resistivity values of the thinner tracks printed using the AR24 anilox are much lower, than those of the AR8 anilox, with a range of 5 – 7 times bulk silver (as opposed to 5-11 times bulk silver for AR8). This indicates that the thinner tracks printed using the AR24 anilox absorb more NIR radiation.

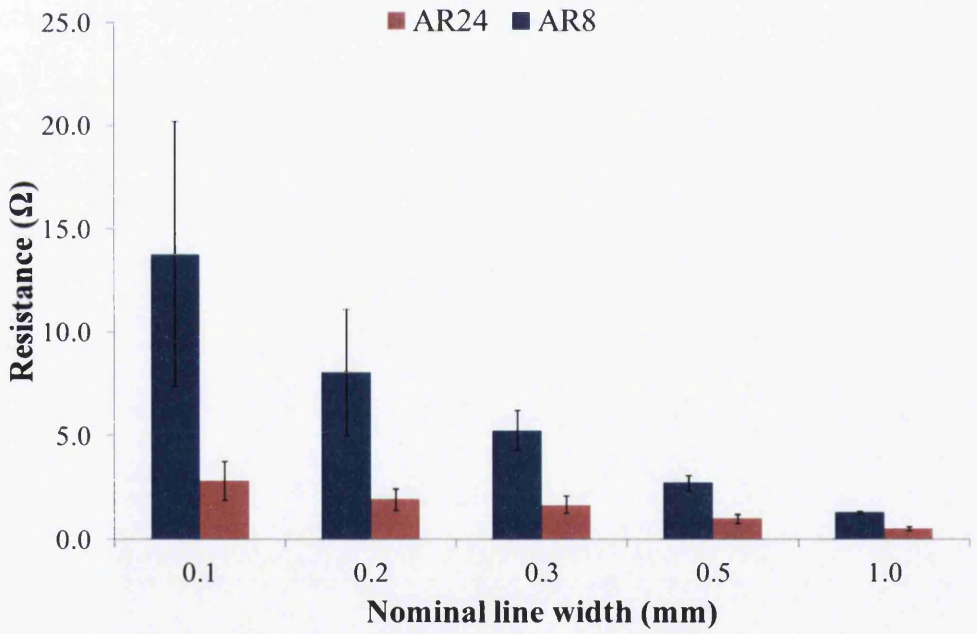

Figure 7-10 Effect of line width on resistance for tracks NIR sintered at 55% emitter power for 1s, compared for samples printed using different volume anilox rolls

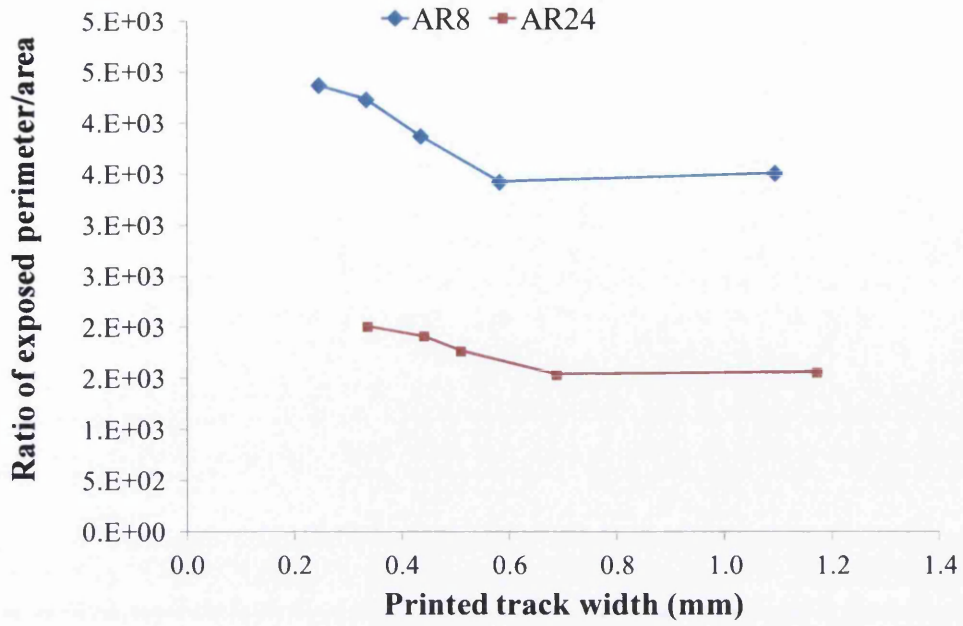

Figure 7-11 Comparison of the ratio of exposed perimeter to cross-sectional area for different track widths for two different anilox roll

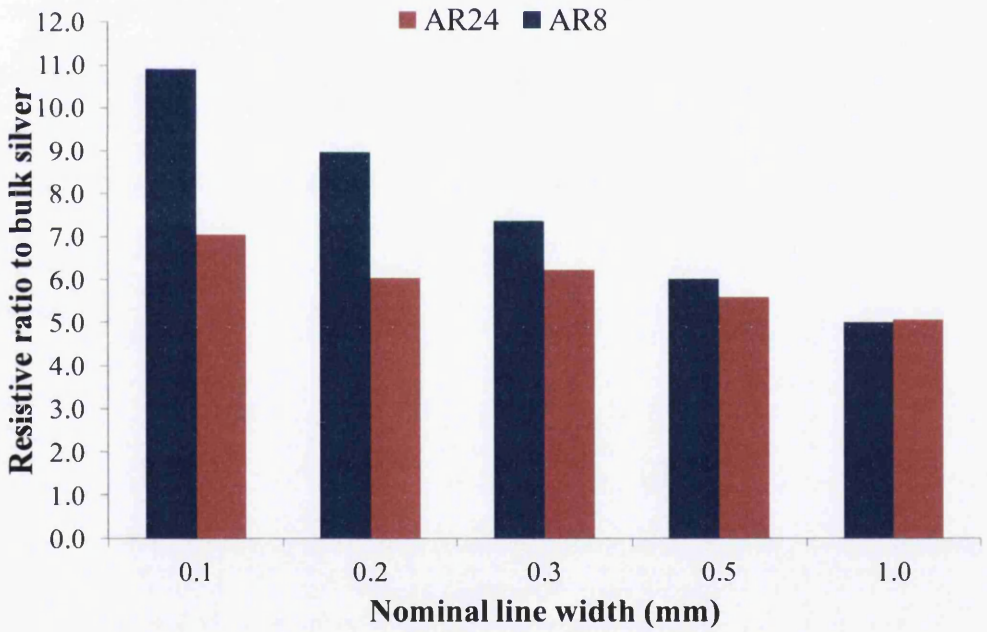

Figure 7-12 Effect of line width on resistivity for tracks NIR sintered at 55% emitter power for 1s, compared for samples printed using different volume anilox rolls

7.4 Conclusions

This study has investigated how NIR drying and sintering affects conductive nanoparticle silver tracks applied by flexographic printing for a process time of 1 second.

NIR emitter power must be great enough to allow the ink vehicle to absorb enough energy to remove the organic components of the ink and facilitate full particle sintering. Too low a power leads to incomplete sintering. For a 1 second process time a minimum emitter power of 50%, which equates to a total intensity of $0.8MWcm^{-2}$, is required for a 1.0mm wide track to ensure it is sintered regardless of anilox volume.

In these experiments wider tracks sintered better than thin tracks when exposed to NIR. This is believed to be because the thinner lines have a greater comparative exposed surface than wider lines which resulted in solvent evaporation in between printing and exposure to NIR. This reduced the absorption of NIR by the ink. Increasing the anilox volume saw a reduction in this ratio and they performed much better under NIR exposure.

This study has increased the understanding of rapid drying and sintering of nanoparticle silver conductive tracks using the NIR drying and sintering process. A resistivity of 5 times bulk silver in 1 second has been achieved for a 1.0mm flexographic printed track. This further highlights the potential of NIR as method for rapidly drying and sintering nanoparticle inks.

8 Evaluation of electrical performance through colour: A potential non-contact, inline measurement system

8.1 Introduction

During the manufacturing of a printed electronic device, it is necessary to ensure the desired electrical performance is obtained by monitoring the drying and sintering process for a conductive ink, preferably as it exits. Silver particles in solution, with a diameter of ~30nm, are shown to absorb in the violet, due to surface plasmon resonance (chapter 2). The observed colour of the solution is yellow/green. An increase in particle size causes a red-shift in the absorption, which changes the observed colour. During the sintering process the size of the silver particles increases so the observed colour should change. In this chapter a non-contact method, which could be implemented inline, to monitor the sintering process of a nanoparticle silver ink through colorimetry is presented.

8.1.1 Quality control methods in printing

Existing R2R quality control methods in the printing industry were developed for the graphics applications and are often based around using image software to visually inspect print registration and feedback to the printer to adjust the web accordingly [1, 2]. Few methods have been developed for R2R testing for quality control in printed electronics. The Hübler group in Chemnitz University have designed an inline measurement system (IMS) for measuring the resistance of printed PEDOT:PSS source/drain structures on PET foils [3]. The substrate passes between two cylinders and at the nip the electrical resistance is detected. The disadvantage of this method is that it is a contact technique and there is the potential to damage the printed material. A non-contact method is preferable.

8.1.2 Colorimetry

The nanoparticle silver ink used throughout this thesis has a characteristic visible colour change between the dried and sintered ink states. Colour can be quantified using colorimetry, which is defined in chapter 3. Colorimetry was developed for use in the graphics industry as a means of quality testing printed media with a requirement to detect small changes in printed colour [4] with CIELAB colour space the industry standard (see section 3.7). The many other diverse uses for colorimetry include predicting emulsion colour in products [5], measuring weathering effects on coated strip steel [6], monitoring the discoloration of waste water [7] and assessing teeth discoloration [8].

Systems have been developed for non-contact spectral imaging using CIELAB to detect in-line colour drift in gravure printing of graphics at high speed [9]. The colour change between the nanoparticle silver ink can be measured using colorimetry and the CIELAB industry standard. In this chapter the sheet resistance of a nanoparticle silver coating will be measured and evaluated against the $L^*a^*b^*$ coordinates to see if there is a correlation between the electrical performance and the colour of the ink. A correlation would be a first step in evaluating the potential of colorimetry for use as a non-contact quality control method for printed electronics manufacturing.

8.2 Experimental procedure

The nanoparticle silver ink (InkTec TEC-PR-030) used in this work consists of ~30nm diameter silver particles. Samples were printed using a mechanical bar coater (RK K-Coater, k-bar 1), giving an average dry film thickness of 0.240μm (±0.030μm), onto PET foil substrate (Dupont-Teijin Films, Melinex ST504 175μm). The samples were rapidly dried and sintered using NIR radiation across a range of dwell times (≤2s) and power conditions to create a complete collection of samples with a varied degree of sintering and consequently a range of electrical performance. Comparative samples were dried in a convection oven (SC Driers combination furnace).

Sheet resistance of the processed silver films was measured using the 4-point probe method described in chapter 2 using a Keithley 2400 sourcemeter.

The CIELAB colour space values were measured using a sphere spectrophotometer (X-Rite SP64, D65/10 standard) recording the specular excluded, diffuse data to reduce the effect of the reflective metallic film. A sphere spectrophotometer was chosen so that the diffuse data could be measured.

8.3 Results and discussion

Figure 8-1 shows that the lightness value, L^*, does not show a significant correlation to the sheet resistance. The data is scattered although some samples with low sheet resistance do appear to have a marginally higher L^* value, which is what was expected because the ink film is more metallic and therefore more reflective.

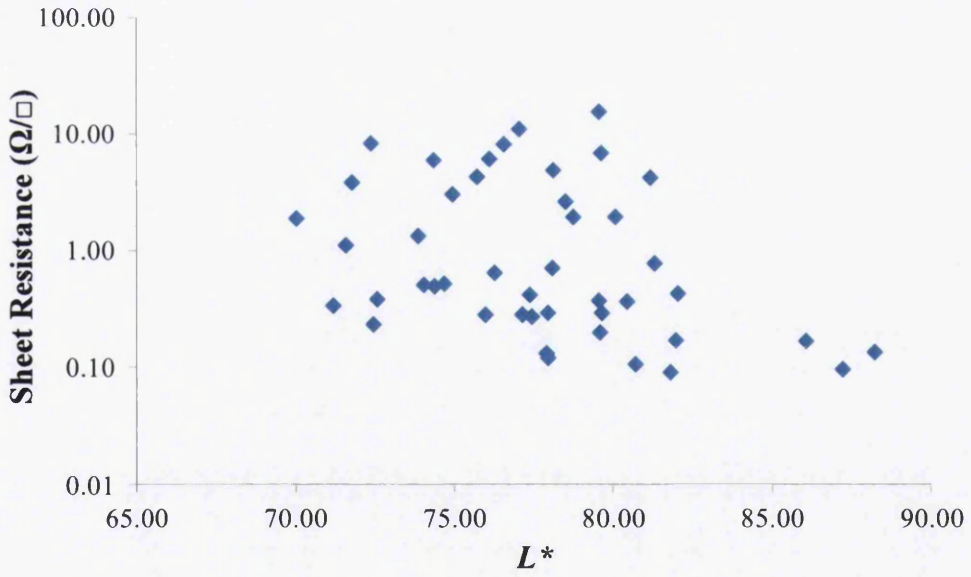

*Figure 8-1 Relationship between the L*colour space value and sheet resistance for NIR sintered nanoparticle silver ink*

The shift in a^*, shown in Figure 8-2, represents a colour change from green (negative a^*) to red (positive a^*). The results show that there is a reduction in the green colour as the sheet resistance reduces with the best sintered silver films occuring where the a^* coordinate is zero (range: -0.5 to +0.5). Therefore, on a printing press using a NIR drier if a^* values were negative then this is indicative of the ink film not being sintered and the NIR emitter power would need to be altered. In samples where a^* values were positive (>+0.5) the PET substrate was observed to be damaged thermally. PET has been shown to exhibit an increase in a^* from approximately zero to a positive value at high temperatures to due recrystallisation [10], with noticeable distortions leading to a cracked ink film and an increased sheet resistance.

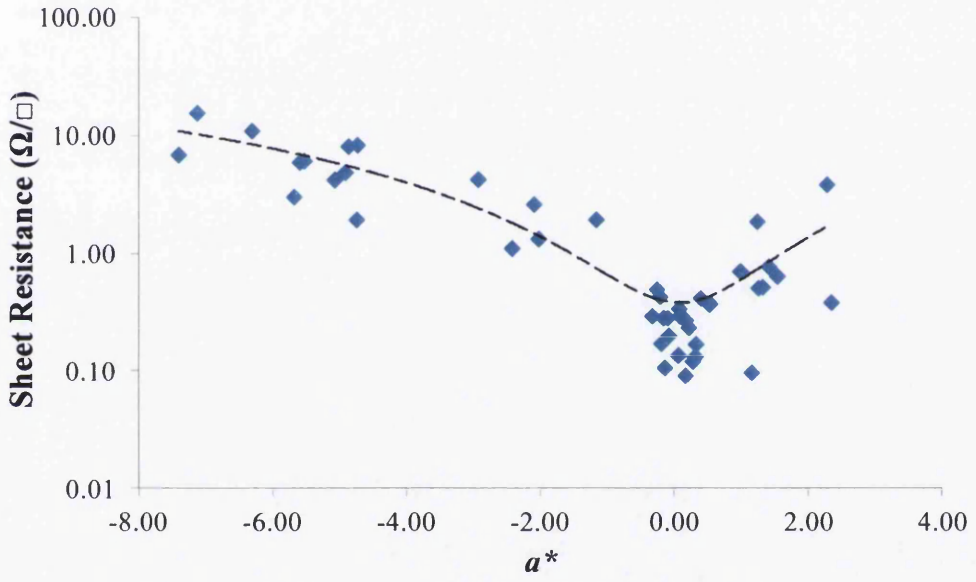

Figure 8-2 Correlation between a color space values and sheet resistance for NIR sintered nanoparticle silver ink*

The b^* coordinate represents the colours blue (negative b^*) and yellow (positive b^*). Figure 8-3 illustrates the shift in the b^* value with regards to sheet resistance. The trend shows that as sheet resistance decreases the b^* values are reduced; from a positive value to a less positive value. This is indicative of a reduction in the yellow component. Samples exhibiting the best sheet resistance occurred in a narrow range between +7 and +12.

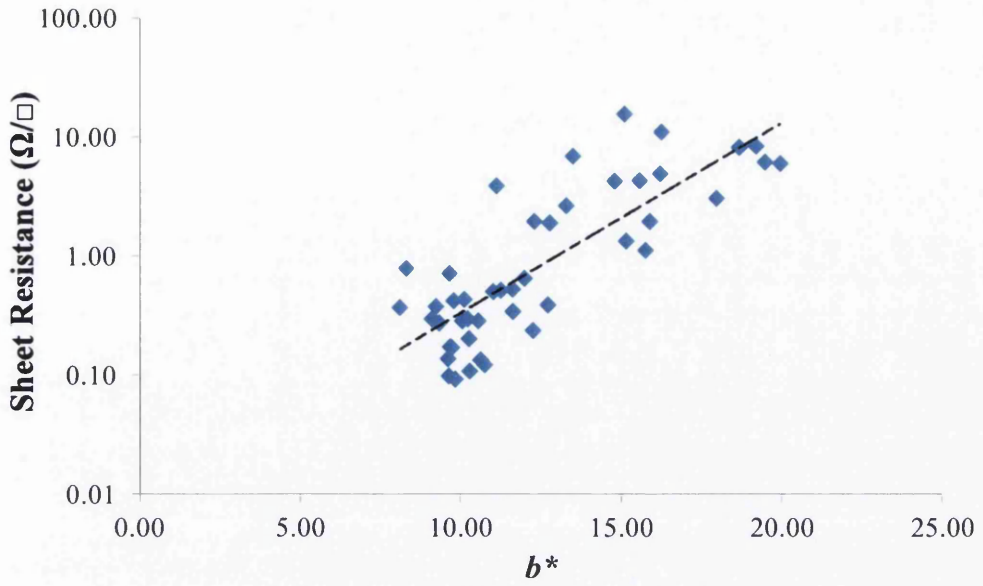

Figure 8-3 Correlation between the b color space value and sheet resistance for NIR sintered nanoparticle silver ink*

If both a^* and b^* coordinates are considered simultaneously then the overall colour shift can be visualised for the sintering process of a NIR sintered ink film. Figure 8-4 shows the colour shift, with the sheet resistance is represented by the size of the circle. As the electrical performance of the ink improves a^* values increases to zero and b^* values reduce to approximately +10.

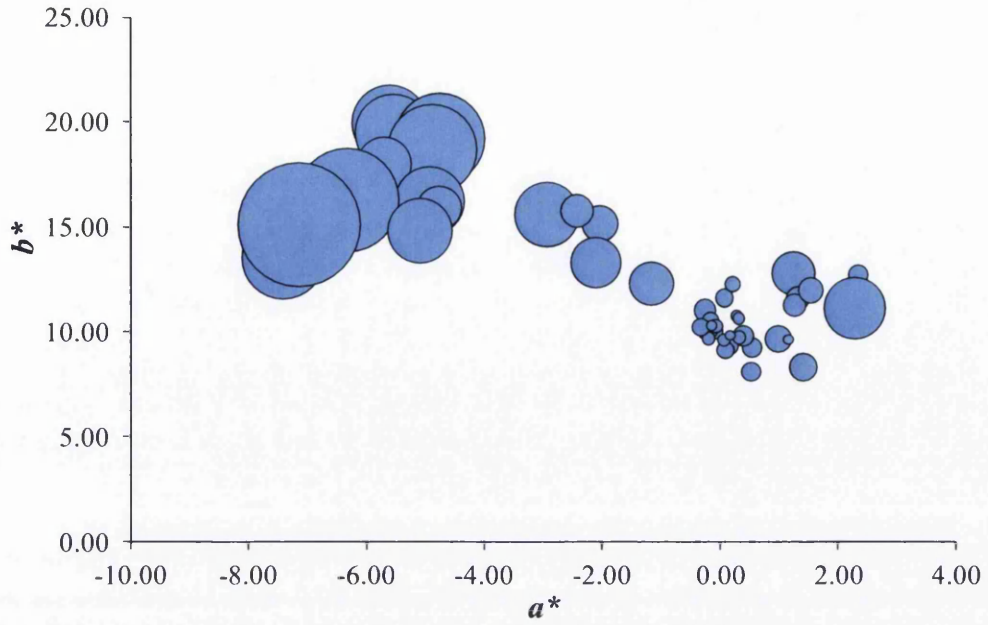

Figure 8-4 The 2D colour shift for NIR sintered nanoparticle silver ink with sheet resistance graphically represented by the size of the circle (N.B. Small circle = low sheet resistance)

To see whether there was any dependence between cure method and colour a conventional convection oven at 140°C was used to replicate the work. A 2D colour shift in a^* and b^* is shown in Figure 8-5. The range in processing time increased from < 2.5s for the NIR samples to 7s and 680s for the oven samples. The a^* coordinates showed the same trend as the NIR processed samples. The b^* values showed no change, with respect to sheet resistance, remaining at a value of approximately +20. A possible explanation for this is that during NIR processing the ink resin could be chemically changed by absorbing in the NIR band which could result in a change in the yellow colour. During oven sintering the heat transfer process is through convection heating so the resin would not absorb meaning that the yellowness and therefore b^* value would not change.

Figure 8-6 shows the effect of drying time on the a^* coordinate for oven dried samples with sheet resistance is illustrated graphically. As dwell time increases the ink becomes more sintered and a^* moves from a negative value towards zero.

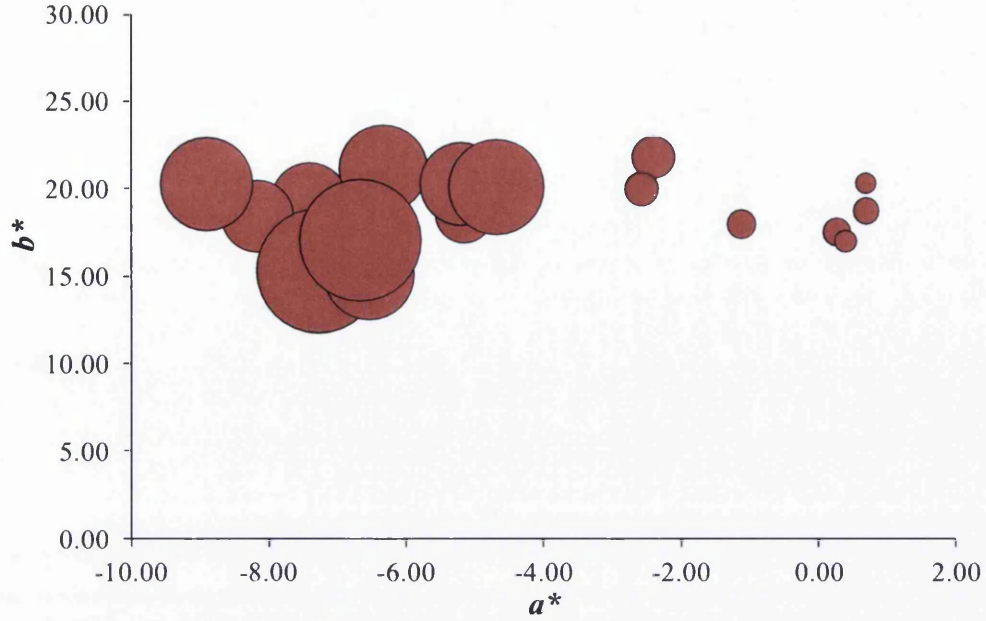

Figure 8-5 2D colour shift for oven processed samples with sheet resistance graphically represented by the size of the circle (NB. Small circle = low sheet resistance)

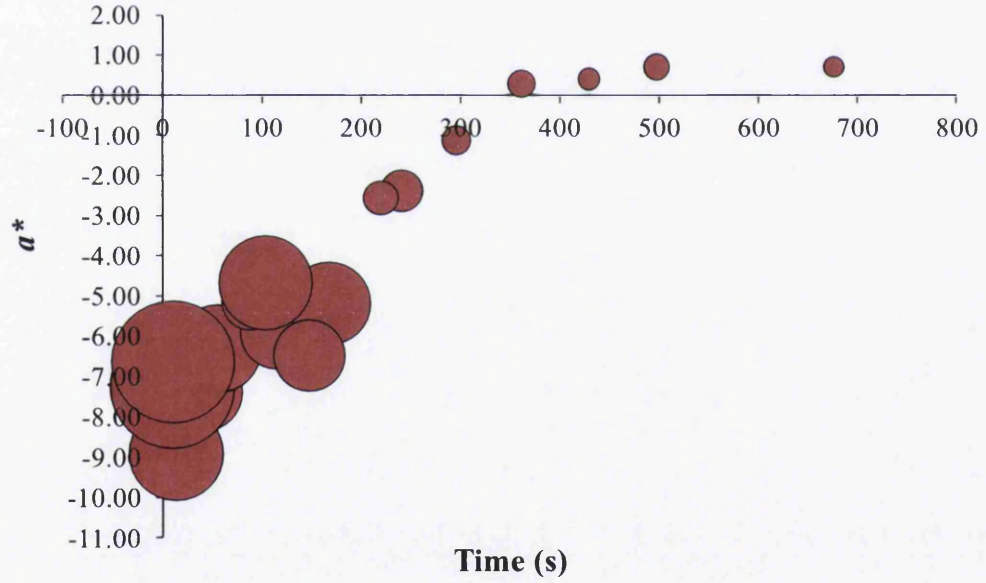

Figure 8-6 Effect of time on a for oven processed nanoparticle silver ink with sheet resistance graphically represented by the size of the circle (NB. Small circle = low sheet resistance)*

To understand the change in colour between non-sintered and sintered states the microstructure of the ink film is considered. Figure 8-7 shows SEM images of both non-sintered (a) and sintered (b) ink films. CIELAB and sheet resistance data for the SEM images is presented in Table 8-1. The non-sintered ink film has an a^* value of -7.14, b^* value of +15.11 and a sheet resistance of 15.69Ω/□. The sintered ink film has an a^* value of 0.06, b^* value of +9.61 and a sheet resistance of 0.137Ω/□. The non-sintered, but dried, ink film shows separate silver nanoparticles with a diameter of ~30nm. In contrast, the sintered ink film shows that the particles have merged, or sintered, together forming a continuous and conductive film.

The size distribution of the silver nanoparticles in the ink (Figure 8-8) shows that the mean particle size is 29nm. It can be calculated from the literature that the non-sintered nanoparticles will therefore exhibit absorption due to SPR at ~430nm. This value correlates to the yellow/green colour observed both visually and in the colorimetric measurements of a^* and b^*.

A sample diffuse reflectance spectrum for the nanoparticle silver ink in sintered and non-sintered states is shown in Figure 8-9. The non-sintered ink film exhibits a maximum reflectance at ~550nm, which corresponds to the green waveband of the visible spectrum. The sintered ink has a much broader spectrum, reflecting more across the visible spectrum.

(a)

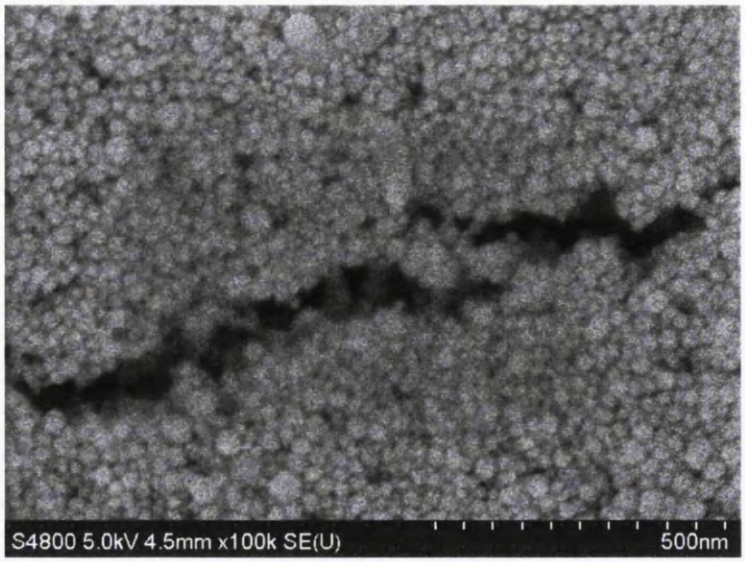

(b)

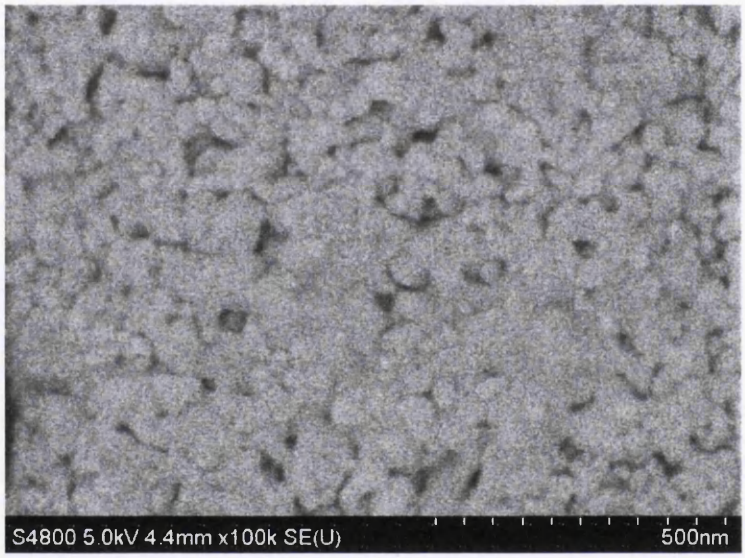

Figure 8-7 Scanning electron microscope images of the (a) dried and non-sintered nanoparticle silver film (a -7.14, b* 15.11, sheet resistance 15.69Ω/□) and (b) the sintered ink film (a* 0.06, b* 9.61, sheet resistance 0.137Ω/□)*

Table 8-1 CIELAB and sheet resistance data for the SEM images

SEM Image	*L**	*a**	*b**	Sheet resistance (Ω/□)
(a)	79.55	-7.14	15.11	15.69
(b)	88.22	0.06	9.61	0.137

N.B. CIELAB data is for a diffuse measurement

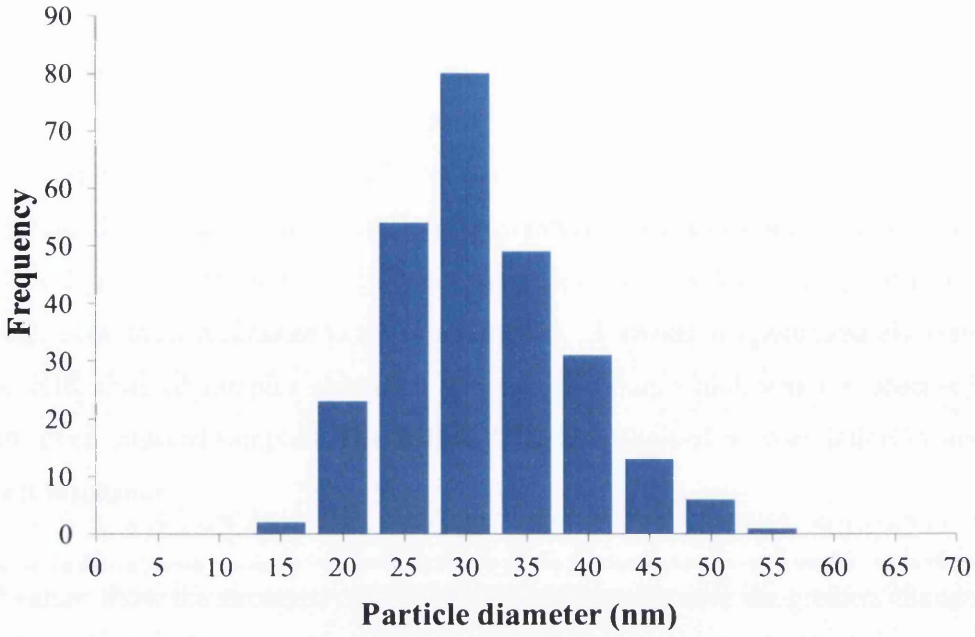

Figure 8-8 Size distribution of silver nanoparticles in the dried and non-sintered ink film

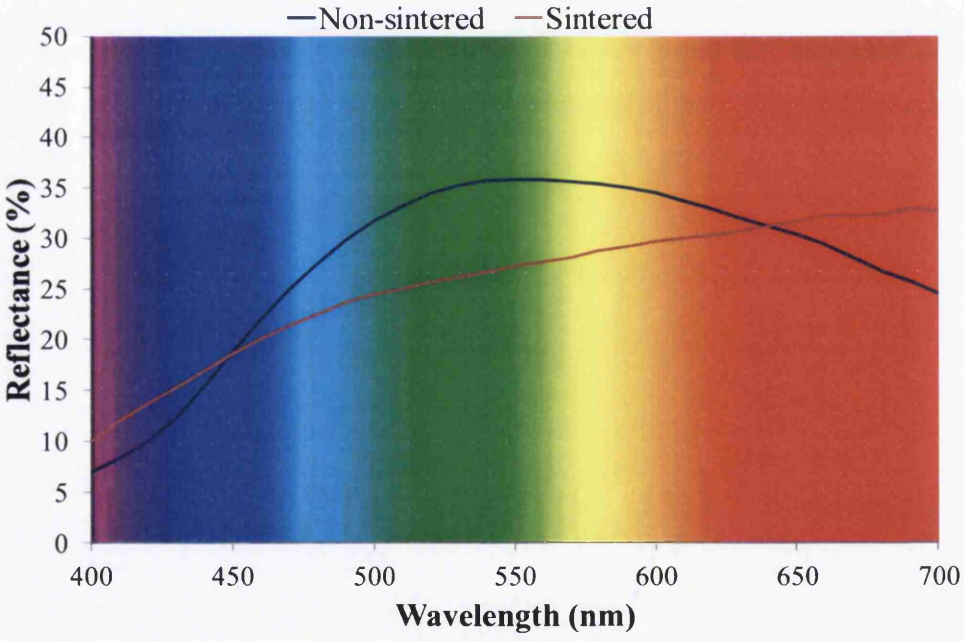

Figure 8-9 Typical diffuse (specular excluded) reflectance spectra of nanoparticle silver ink films both sintered and non-sintered

8.4 Conclusions

In conclusion the electrical performance of a nanoparticle silver ink film can be indirectly measured using colorimetry. The relationship between the CIELAB colour space coordinates; L^*, a^*, b^* and the sheet resistance of the ink was individually evaluated against their corresponding sheet resistance. Samples that gave a high sheet resistance recorded a very negative a^* value and a positive b^* value. Low sheet resistance samples resulted in a^* values of approximately zero and NIR sintered samples showed a reduced b^* value, which was not observed with oven sintered samples. The diffuse L^* values showed no correlation to the sheet resistance.

a^* values show the strongest correlation to resistance because the greatest change in the reflectance is observed in the green region of the spectrum (~550nm). The b^* values exhibit a good correlation when the ink is NIR processed and less so when processed more slowly in an oven, with the reasons for this requiring further investigation.

This is potentially a breakthrough technology which could be integrated to a printing/coating press to be used for inline monitoring of the drying and sintering process of nanoparticle silver inks in a non-contact, non-destructive fashion.

8.5 References

1. Kipphan, H., *Handbook of Print Media*. 2001: Springer.
2. Yang, C.-D. and Y.-C. Chen. *Integrated Longitudinal/Lateral Dynamics and Control of a Moving Web*. in *Large-Area, Organic and Polymer Electronics Convention 2011 (LOPE-C 11)*. 2011. Frankfurt: OE-A.
3. Müller, M.M., K. Weigelt, U. Fügmann, and A.C. Hübler. *Design of an inline measurement system for printed electronic patterns*. in *LOPE-C*. 2011. Frankfurt Messe.
4. Hunt, R.W.G., *Measuring Colour*. 3rd ed. 1998: Fountain Press.
5. McClements, D.J., *Theoretical prediction of emulsion color.* Advances in Colloid and Interface Science, 2002. **97**(1-3): p. 63-89.
6. Wijdekop, M., J.C. Arnold, M. Evans, V. John, and A. Lloyd, *Monitoring with reflectance spectroscopy the colour change of PVC plastisol coated strip steel due to weathering.* Materials Science and Technology, 2005. **21**(7): p. 791-797.
7. Coque, Y., E. Touraud, and O. Thomas, *On line spectrophotometric method for the monitoring of colour removal processes.* Dyes and Pigments, 2002. **54**(1): p. 17-23.
8. Adeyemi, A.A., F.D. Jarad, E.D. de Jong, N. Pender, and S.M. Higham, *The evaluation of a novel method comparing quantitative light-induced fluorescence (QLF) with spectrophotometry to assess staining and bleaching of teeth.* Clinical Oral Investigations. **14**(1): p. 19-25.
9. Brown, N., J. Peng, M.R. Jackson, and R.M. Parkin. *A System for Non Contact Spectral Imaging*. in *2nd International Symposium on Printing and Coating Technology*. 2000. Swansea University: Welsh Centre for Printing and Coating.
10. Phillips, C.O., E.H. Jewell, T.C. Claypole, and D.T. Gethin, *Development of measurement techniques to characterize the optical properties of transparent films with application in in-mould decoration.* Measurement Science & Technology, 2008. **19**(2).

9 Conclusions and further work

9.1 Introduction

This EngD project contributes to the TATA Steel Colors 'PV Accelerator project' to develop a photovoltaic coating based on the dye-sensitized solar cell (DSC) for potential use as a building-integrated photovoltaic system. This project has focused on the printed electronics development for depositing current collectors, which are used to maintain the performance of the DSCs as they are scaled-up.

The objectives of this research were to:

- Investigate printing technologies suitable for high volume R2R production of current collectors for flexible DSCs,
- Develop and optimize a method to increase the speed of the drying and/or sintering process for conductive inks,
- Conceptualize a quality control method which could be used in-line to monitor the sintering process of a metallic nanoparticle conducting ink.

9.2 Conclusions

'Investigate printing technologies suitable for high volume R2R production of current collectors for flexible DSCs':

Rotogravure and flexography were investigated, in Chapter 4, as alternative printing technologies to screen printing for depositing conductive tracks for potential application as current collectors in DSCs. The rotogravure printing trials were unfortunately limited due to the costs associated with the engraving process and access to a rotogravure printing unit was limited. Experiments with flexography proved more successful and consistent conducting tracks with a range of widths were printed. The thicknesses of the flexographic printed tracks

were several orders of magnitudes thinner than tracks produced by screen printing but resistivity values were lower than screen printed tracks. The good electrical performance of the flexographic printed tracks was due to the use of a nanoparticle silver ink which enabled a continuous metallic layer to form after a thermal sintering process.

In Chapter 5, flexible DSCs, consisting of titanium foil and ITO/PET plastic electrodes, with 'thin-film' flexographic printed current collectors were produced alongside cells produced with 'thick-film' screen printed current collectors. Drying time for the PTF microparticle screen printing ink was found to directly affect the performance of a cell; the longer the drying time, the lower the resistivity, the better the performance. For flexographic printed current collectors the anilox volume was shown to affect cell performance; a larger volume anilox resulted in a thicker ink film and a lower resistance, which increased the FF and efficiency. Although the cells with screen printed current collectors resulted in a better Isc and light-to-electric conversion efficiency, the fill factor of the cells with flexographic printed current collectors were higher, and in fact better, than any reported in the literature. Another important observation was that the flexographic printed current collectors deposited a silver thickness which was between 95-99% (depending on the anilox roll volume) thinner than tracks deposited using screen printing for only a 33-35% drop in performance. This is a significant result as the cost of silver for metallization during the scale-up of DSCs represents a large proportion of the overall materials costs and there is a balance between performance and materials costs to consider.

'Develop and optimize a method to increase the speed of the drying and/or sintering process for conductive inks':

Printing is fast, drying is slow. This fact is one of the main problems hindering the manufacturing development of printing electronic devices. In reported literature the sintering process for nanoparticle conductive inks could be achieved in microseconds using photonic devices, but the printed ink film had to be dry prior to sintering. This preliminary drying step still required several minutes in an oven. A process which requires a complete 'as printed' wet to fully

dried and sintered ink film is desirable. Near infrared (NIR) radiation was found to sinter nanoparticle silver coated thick-films in 2 seconds (Chapter 6) and thin flexographic printed tracks in 1 second (Chapter 7). The energy density delivered by the NIR emitter across a narrow bandwidth (800-1200nm), which is near invisible to PET substrates but in a region where the wet nanoparticle ink system absorbs, means that the drying and sintering is extremely fast and gave comparable results to samples dried in an oven and using a mid-IR emitter. It was found that thinner tracks achieved a higher resistivity than wider tracks. Possibly this is associated to different evaporation rates of solvent; Thin tracks were found to dry quickly, even before being passed under the NIR emitters, increasing their reflectance before NIR exposure.

'Conceptualize a quality control method which could be used in-line to monitor the sintering process of a metallic nanoparticle conducting ink':

After the printing and drying process there are no existing methods to assess whether a conductive ink is performing to its desired potential. It was observed during experiments that there was a visual difference in colour between a dried and a sintered nanoparticle silver ink film. By using a spectrophotometer to measure the CIELAB colorimetry coordinates it was found that the colour of a given nanoparticle ink film could be correlated to its electrical resistance (Chapter 8). The most significant parameter was the a^* coordinate, which corresponds to green or red. A negative value meant that the ink film was not sintered whereas a value close to zero indicated a sintered ink film. This color variation during sintering has been associated to the surface plasmon resonance effect.

9.3 Further work

- Optimize the flexographic printed current collector to maximize performance by investigating; the design, different track widths, larger volume anilox rolls, other nanoparticle inks (e.g. copper). Then look to scale-up the size by building a test module using the printability tester and possibly scale-up to a full size printing press.
- Use NIR to rapidly sinter nanoparticle current collectors and integrate into a DSC.
- Investigate rapid NIR sintering of different nanoparticle inks, for instance copper.
- Integrate a NIR drying unit with a large press and investigate whether the electrical performance of smaller features could be improved in a R2R setup and see what the limits of process speed are.
- Develop the colorimetric monitoring with the aim of integrating it with a printing press.

9.4 List of journal publications

M. Cherrington, T. C. Claypole, D. Deganello, I. Mabbett, T. Watson, and D. Worsley, *Ultrafast near-infrared sintering of a slot-die coated nano-silver conducting ink.* Journal of Materials Chemistry. **21** (21) p.7562-7564

M. Cherrington, T.C. Claypole, D.T. Gethin, D. Worsley, and D. Deganello, *Non-contact assessment of electrical performance for rapidly sintered nanoparticle silver coatings through colorimetry.* Thin Solid Films. In Press, Accepted Manuscript.

A. Appendix

A.1 Rotogravure printing trial

A.1.1 Introduction

Rotogravure has been investigated by several groups for printing electronic features for devices such as RFID [1], transistors [2, 3] and OLEDs [4] but not for application in DSCs. The purpose of this work was therefore to conduct an exploratory trial to assess rotogravure as a printing technology for depositing conductive tracks.

The gravure printing process was discussed in Chapter 1. Rotogravure is mechanically simpler than other printing processes and also has the ability to print a wide range of ink film thicknesses in one printing cylinder by using different line rulings in the engraving to change the roll capacity. Other printing processes such as screen and flexography do not have this ability.

A.1.2 Rotogravure printing trial

This was a scoping trial designed to gain a basic understanding of gravure printing and test the feasibility of the rotogravure process for printing conductive tracks for potential use as current collectors for DSCs. Different width lines were printed to test how the electrical performance of the ink changed. The brief given to the engravers was that lines with smooth edges were required and a line ruling be selected to ensure that the fine lines would print homogeneously.

A.1.2.1 Experimental procedure

The trial was carried out at Keating's Specialist Cylinders in Flintshire using a Heaford 3m drum proofing press to print the samples. The cylinder was electromechanically engraved to the engravers recommendations with a line ruling of 400lines/cm at a 45° engraving angle and a stylus angle of 105°. The engravers decided that the wide range of line widths, coupled with the requirement to make the line edges smooth, would require a fine engraving specification. Lines were specified as 40mm long and widths of; 0.1mm, 0.2mm, 0.3mm, 0.5mm and 1.0mm. The substrate was PET (Melinex ST504 175μm). Ink used was a microparticle ink, from Parelec Inc. (Parmod DYA-100) diluted to manufacturers specifications to 14wt% solvent with *tert*-butyl acetate. Drying conditions were as recommended by the manufacturer and were 5 minutes at 150°C in a hot air oven.

A.1.2.2 Print analysis

This section will present the results of the rotogravure scoping trial carried out to assess the feasibility of using the rotogravure process in this thesis. All results are from lines printed parallel to the print direction.

Figure A-1 shows the averaged 2D profiles of the gravure printed tracks, measured using white light interferometry. The lines appear uniform and symmetric but the surface becomes rougher as the width increases. This surface roughness is caused by the cell structure of the engraving and is linked to the cell frequency.

The topography images of the printed lines, in Figure A-2, show that the edges are fairly smooth but the lines are discontinuous and broken, with the exception of the 0.1mm wide line which has a continuous centre. This will impact upon the electrical performance by increasing resistance and also indicates that the engraving was not optimal for the coarser features. To prevent the discontinuity in the ink film and make the lines more consistent a greater volume of ink should

be printed. This could be achieved by increasing the cell size, by decreasing the line ruling, thereby making the engraving coarser.

Cross-sectional area of the tracks (Figure A-3) increases linearly with width. The printed track width was different from the nominal width and the percentage of spreading is shown in Figure A-4. The wider lines spread less than the thinner lines.

Figure A-5 shows that the average and maximum height of the printed lines are consistent at 1μm for widths of 1.0mm to 0.3mm. The 0.2mm wide lines have the lowest average and maximum heights. 0.1mm wide lines have an average height greater than the 0.2mm lines but lower than the 0.3mm lines but they do have the greatest maximum height of 1.65μm.

Resistance decreases with increasing track width (see Figure A-6). The 0.1mm lines exhibit the highest resistance. The 2D profile and the topography image shows that the 0.1mm lines are the most consistent, especially in the centre of the line, and have the greatest maximum height, even though they have the second lowest average height. It is the line with the fewest visible breaks and the most consistent, which likely explains its superior electrical performance. The 0.2mm wide tracks are the second worst performing overall but the topography image shows that it has many defects in the print, which would increase resistance. The 1.0mm wide lines have the highest resistivity value but they have also been shown to have a lot of defects in the print.

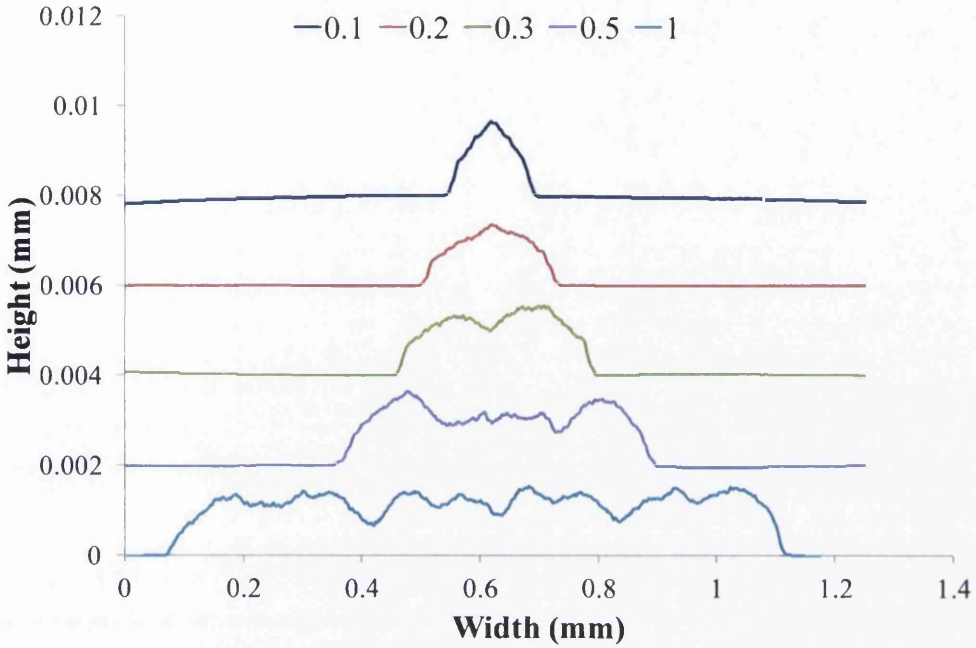

Figure A-1 Gravure printed cross-section profiles

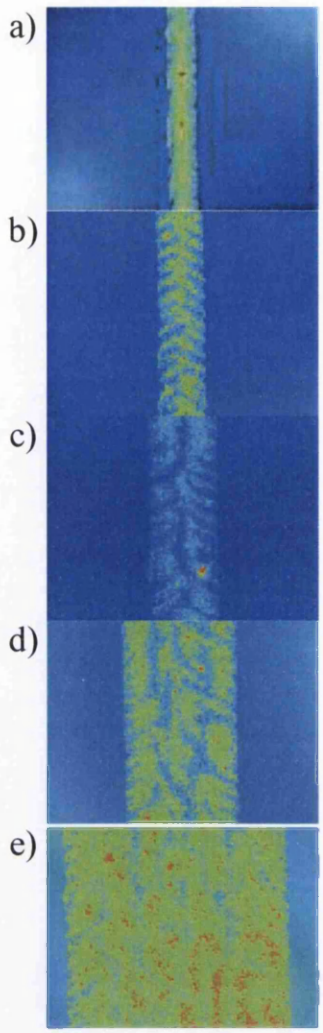

Figure A-2 Whitelight interferometer topography images for gravure printed lines for nominal widths of: a) 0.1mm, b) 0.2mm, c) 0.3mm, d) 0.5mm, e) 1.0mm

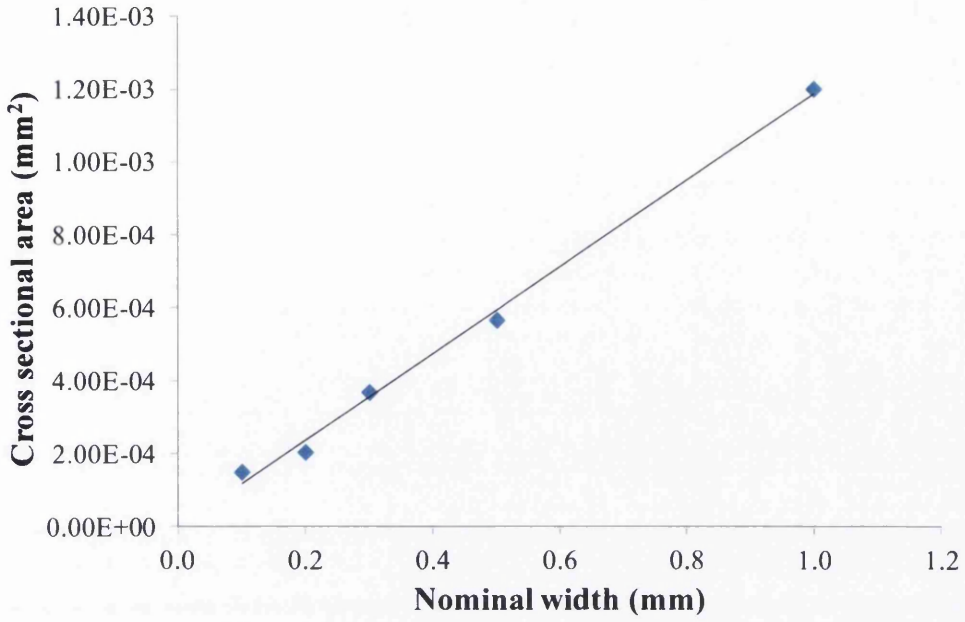

Figure A-3 Cross sectional area verses width for gravure printed lines

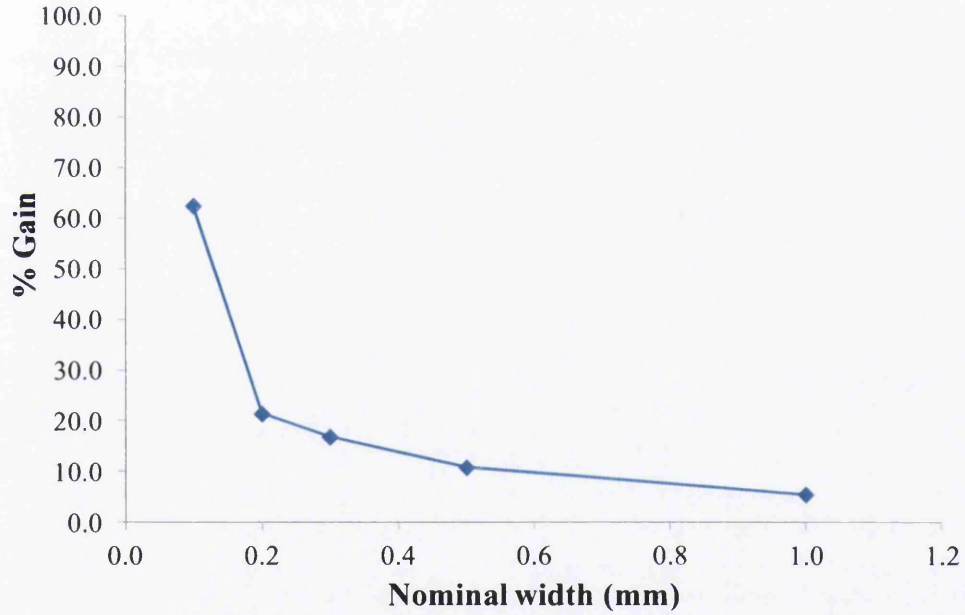

Figure A-4 Line gain from the nominal width for gravure printed lines

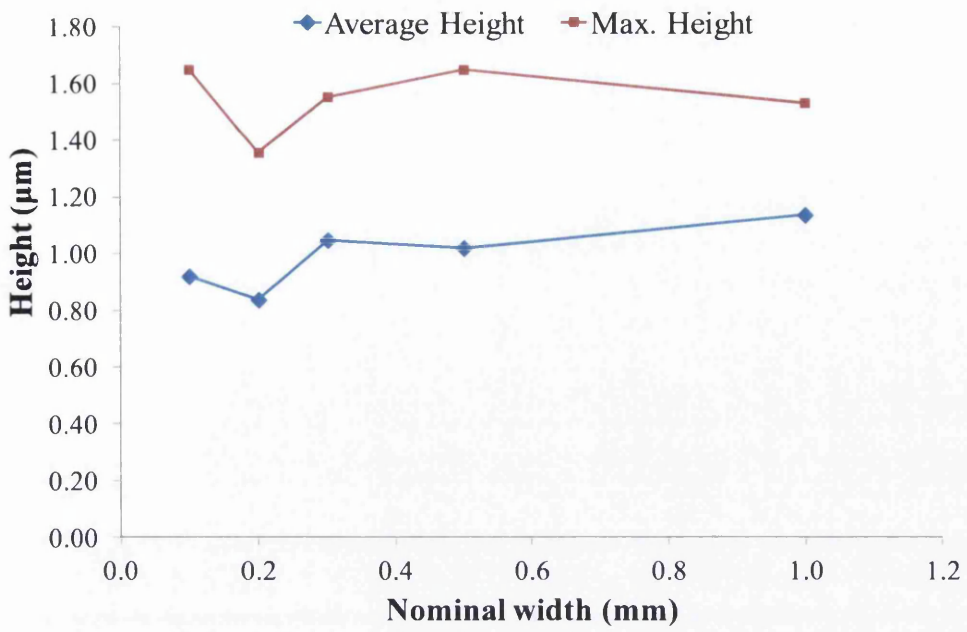

Figure A-5 How average height and maximum heights vary with line width for gravure printed lines

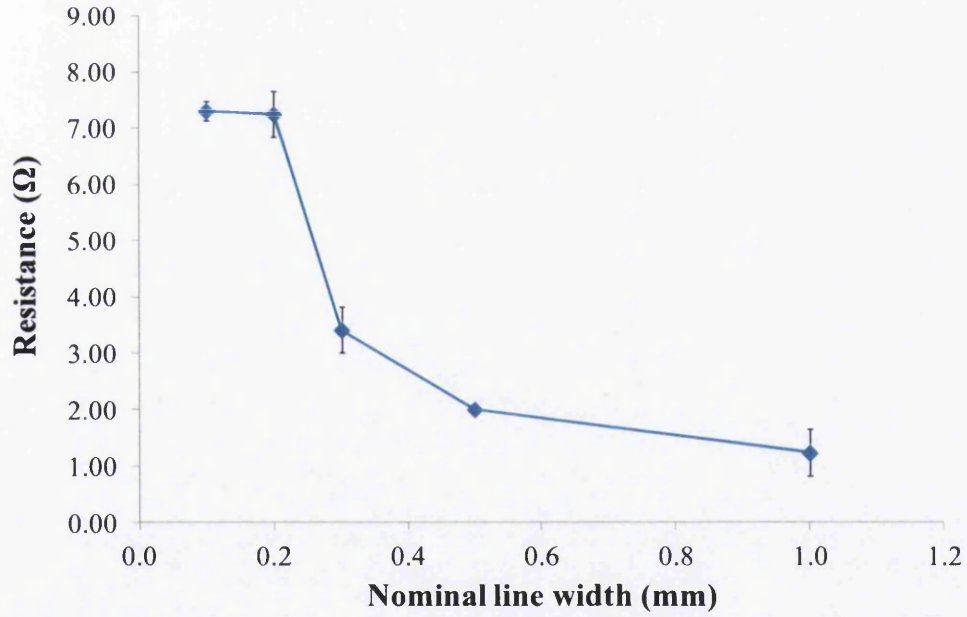

Figure A-6 How resistance changes with width for a microparticle silver ink dried at 150°C for 5 mins

A.1.3 Summary

This exploratory trial has demonstrates rotogravure as a potential method to print conductive features. However, there were several issues with the trial: Firstly, the line topography was very rough, caused by the engraved cell structure. Secondly, there were many defects in the printed tracks (with the exception of the 0.1mm tracks) which impacted on the electrical resistance. The resistivity results showed what the topography images confirmed; the line ruling used for the engraving was better suited to thinner track widths.

A further trial to carry out a factorial experiment using a variety of line rulings was proposed but rejected due to cost reasons. Other printing technologies offered cheaper and more available alternatives. Rotogravure printing has potential for use in printed electronics manufacturing but high setup (engraving) costs and poor line morphology, a result of the engraved cell structures, which ultimately limit its potential for producing low resistivity features.

A.1.4 References

1. Allen, M., C. Lee, B. Ahn, T. Kololuoma, K. Shin, and S. Ko, *R2R gravure and inkjet printed RF resonant tag.* Microelectronic Engineering. **88**(11): p. 3293-3299.
2. Huebler, A.C., G.C. Schmidt, H. Kempa, K. Reuter, M. Hambsch, and M. Bellmann, *Three-dimensional integrated circuit using printed electronics.* Organic Electronics. **12**(3): p. 419-423.
3. Kang, H., R. Kitsomboonloha, J. Jang, and V. Subramanian, *High-Performance Printed Transistors Realized Using Femtoliter Gravure-Printed Sub-10 mu m Metallic Nanoparticle Patterns and Highly Uniform Polymer Dielectric and Semiconductor Layers.* Advanced Materials. **24**(22): p. 3065-3069.
4. Kopola, P., M. Tuomikoski, R. Suhonen, and A. Maaninen, *Gravure printed organic light emitting diodes for lighting applications.* Thin Solid Films, 2009. **517**(19): p. 5757-5762.
5. Pudas, M., N. Halonen, P. Granat, and J. Vahakangas, *Gravure printing of conductive particulate polymer inks on flexible substrates.* Progress in Organic Coatings, 2005. **54**(4): p. 310-316.
6. Hrehorova, E., M. Rebros, A. Pekarovicova, B. Bazuin, A. Ranganathan, S. Garner, G. Merz, J. Tosch, and R. Boudreau, *Gravure Printing of Conductive Inks on Glass Substrates for Applications in Printed Electronics.* Journal of Display Technology. **7**(6): p. 318-324.

7. Noh, J., D. Yeom, C. Lim, H. Cha, J. Han, J. Kim, Y. Park, V. Subramanian, and G. Cho, *Scalability of Roll-to-Roll Gravure-Printed Electrodes on Plastic Foils.* Ieee Transactions on Electronics Packaging Manufacturing. **33**(4): p. 275-283.
8. Clist, A.M., *Ink transfer in image and non-image areas in the rotogravure process*. 2004. PhD Thesis Swansea University